ANALYSIS OF WATER TRANSPORT PHENOMENA IN THIN POROUS MEDIA OF A POLYMER ELECTROLYTE MEMBRANE FUEL CELL

by

Logan Robb Battrell

A dissertation submitted in partial fulfillment
of the requirements for the degree

of

Doctor of Philosophy

in

Chemical Engineering

MONTANA STATE UNIVERSITY
Bozeman, Montana

November 2018

DEDICATION

To Fred and Martha, for their constant support, love, and encouragement; and to all of my teachers and educators, who recognized potential and never gave up, thank you for all of the inspiration.

ACKNOWLEDGEMENTS

I'd like first thank my advisor Dr. Ryan Anderson for taking a chance on me when it seemed like nobody else would. Your advice and confidence in me has been irreplaceable and I will always look back on our first meeting as a pivotal moment in my life. I'd also like to thank the other members of my committee, Drs Jen Brown, Erick Johnson, and Lifeng Zhang, for their continual advice and feedback. Additionally, I'd like to acknowledge and thank all of the excellent undergraduates who passed through the lab during my time here: Aubrey Trunkle, Erica Eggleton, Megan English, Joe Watkins, Prasaad Milner, and Duncan Jacobsen, you all consistently exceeded my expectations. I'd also like to thank David and Isabel for their help in editing and revising everything I've written and helping to keep me calm and sane throughout this whole process.

Finally, I'd like to thank my Mom and Dad. You've both always been there to talk me through my lowest times, kept me focused on the big picture, and helped me remember that home was always only a phone call away; I wouldn't have gotten through this without you both. To the rest of my friends and family, thank you for all of the love and support you've given me throughout this entire adventure.

This material is based on work supported, in part, by the NSF under award number 1444198. Any opinions, findings, and conclusions or recommendations expressed in this material are those of the authors and do not necessarily reflect the views of the National Science Foundation. The author also acknowledges Montana State University for funds related to these efforts and the Center for Biofilm Engineering at Montana State University for access to imaging software.

TABLE OF CONTENTS

TABLE OF CONTENTS — CONTINUED

TABLE OF CONTENTS — CONTINUED

LIST OF TABLES

LIST OF FIGURES

LIST OF FIGURES CONTINUED

Figure Page

ABSTRACT

This thesis explores and quantifies water transport related to the desaturation of the thin porous layer known as the Gas Diffusion Layer (GDL) associated with Polymer Electrolyte Membrane (PEM) fuel cells. The proper management of water within this layer is critical to optimal fuel cell performance. If there is not enough water, the membrane can become dehydrated, which leads to poor cell performance, but if too much water accumulates or becomes flooded, gas transport is restricted, which also lowers performance and can potentially lead to total cell failure. Understanding the desaturation of this layer is thus key to obtaining and maintaining optimal fuel cell performance. This behavior is explored both at the macroscale, through the quantification of the removal of excess water from an active fuel cell, as well as at the micro-scale, through the use of synchrotron X-ray computed tomography (X-ray CT) to visualize and quantify the desaturation of an initially flooded GDL. The macro-scale investigation extends the previously developed qualitative Anode Water Removal (AWR) test, which functions to identify when poor PEM fuel cell performance is due to excess water, to a diagnostic protocol that quantifies the amount of water being removed by the test through an analysis of the anode pressure drop. Results show that the protocol can be applied to a variety of fuel cell setups and can be used to quickly quantify water management capabilities of novel GDL materials. The microscale investigations show that while both convection and evaporation play a role in the desaturation, evaporation is required to fully desaturate the GDL. Additionally, the microscale investigation allows for the spatial segmentation of the GDL to identify local desaturation rates and temporal saturation profiles, which show that the overall desaturation of the GDL is a heterogeneous process that depends on initial conditions, flow field geometry and the natural anisotropy of the material. Results show that future control strategies and modeling studies will need to expand their investigated domains in order to accurately capture the fully heterogeneous nature of this process.

CHAPTER ONE

PEM FUEL CELLS: INTRODUCTION AND BACKGROUND

1.1 Introduction

Polymer Electrolyte Membrane (PEM) fuel cells are an energy conversion technology that have been imagined as a focal point of a future hydrogen-based power supply. Their main attractive qualities include zero local greenhouse gas emissions, high power density, and scalability. However, further research is still required before the widespread integration of these power conversion devices can occur. To help bring about the widespread adoption of PEM fuel cells, the Department of Energy identified specific goals for their progress by 2020, specifically the improvement to their long-term durability, overall power efficiency, and cost [1]. One of the key issues related to long-term PEMFC durability is water management within the thin porous gas diffusion layer (GDL) [2]. This thesis explores both the macroscale and microscale characterization of water transport in the GDL of a PEM fuel cell. This is accomplished first by experimental characterization through an active fuel cell test, which determines water fluxes through pressure drop analysis. Then, synchrotron radiography is used to investigate and quantify the desaturation of the GDL at the microscale. The developed protocol is a novel diagnostic test that quantifies liquid movement across an active fuel cell, while synchrotron results show that the desaturation of the GDL is a largely heterogeneous process.

The following sections of this chapter provide the theoretical background of how PEM fuel cells work, review what challenges and problems are associated with water management, and describe how synchrotron radiography works, which is the visualization tool used in this study. The final section of this chapter details the overall goals of this work and describes the contents of the rest of the thesis.

1.2 Hydrogen Fuel Cell Background

Similar to batteries, fuel cells turn stored chemical energy into electricity. But while both rely on electrochemistry, a fuel cell will continue to produce electricity as long as fuel is supplied. Polymer Electrolyte Membrane (PEM) fuel cells are a variety of fuel cell that utilize the electrochemical reaction between hydrogen and oxygen, producing water. More commonly referred to as hydrogen fuel cells, this technology has drawn consistent interest due to their potential to be a cornerstone of a future sustainable and renewable energy grid. These devices have been envisioned as both a replacement for combustion engines in vehicles and for integration into the power grid to help off-set peak loads. One of the main benefits to hydrogen fuel cells is that they have no local greenhouse gas emissions, while also featuring high power density, scalability, and rapid start-up [2]. Currently, most major car companies have a working prototype PEM fuel cell car, such as the Honda FCX Clarity™ and Toyota Mirai™, and fuel cell stacks are used around the world for residential (3-7 kW) and commercial (+50kW) electricity and hot water applications [3]. These fuel cells are also being integrated into transit buses, industry vehicles, such as forklifts, and as back-up or auxiliary power systems [1].

As mentioned above, the electrochemical reaction within PEM fuel cells is the hydrogen combustion reaction or

$$H_2 + {}^{1}/_{2}\, O_2 \rightarrow H_2O + Heat \qquad (1.1)$$

This overall reaction is separated into its two half reactions by a polymer membrane, which is impermeable to both the reactant gases and electrons. This membrane is coated on both sides with catalyst particles supported on carbon and is generally referred to as the Catalyst Coated Membrane (CCM). The CCM is sandwiched between a pair of thin porous Gas Diffusion Layers (GDL), graphite plates with embedded flow channels, and current collector plates. A schematic diagram of all of these parts, as well as the general operation of a PEM fuel cell, is shown in Figure 1. Protons are created at the anode and pass through the membrane as electrons pass through an external circuit. At the cathode, the protons and electrons react with oxygen and produce water. Ideally, this product water then moves through the GDL to the gas flow channels where it can be removed. The combination of the two GDLs and the CCM is commonly referred to as the Membrane Electrode Assembly (MEA). When in operation, the gas streams flow through the graphite plates and then diffuse through the GDLs to the catalyst layer, where the appropriate half reactions then take place.

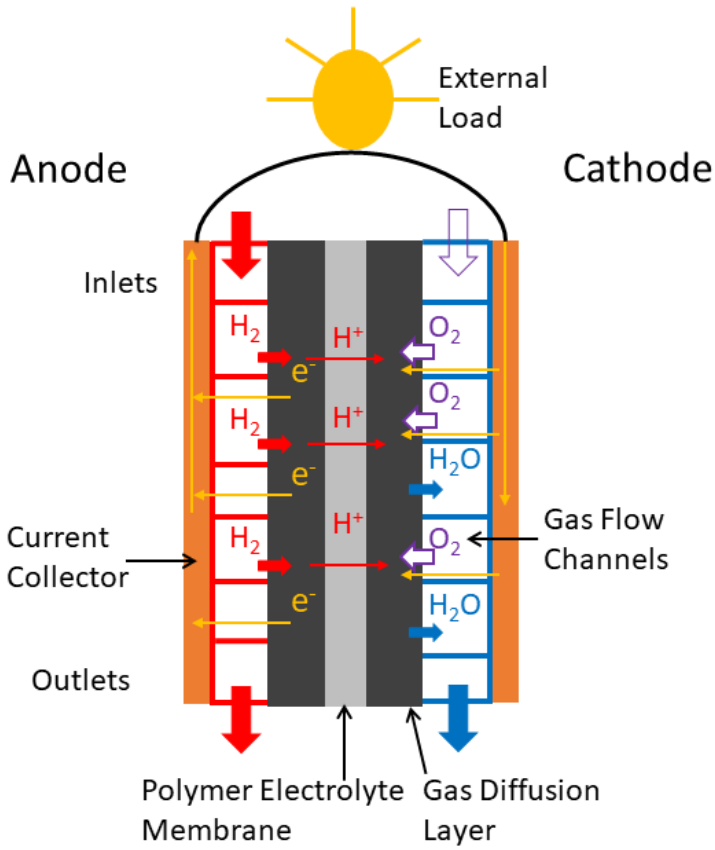

Figure 1. Schematic of PEM fuel cell components and the basic principles of operation

Breaking down the overall reaction into its two half reactions, the reaction on the anode side of the fuel cell is

$$\mathrm{H_2} \rightarrow 2\mathrm{H^+} + 2\mathrm{e^-} \qquad E_0 = 0V \qquad (1.2)$$

while the reaction that takes place on the cathode side is

$$^1/_2\, O_2 + 2\mathrm{H^+} + 2\mathrm{e^-} \rightarrow H_2O \qquad E_0 = 1.23V \qquad (1.3)$$

leading to an overall reaction of

$$H_2 + {}^1/_2\, O_2 \rightarrow H_2O + Heat \qquad E_0 = 1.23V \qquad (1.4)$$

The E_0 term refers to the standard-state reversible voltage (T = 0°C, P = 1 bar). However, as fuel cells generally do not run at standard conditions, this value changes during operation. The next sections provides a brief overview of the thermodynamics, different kinds of voltage losses that occur during operation, properties of key fuel cell components, typical operating conditions, and a summary of the challenges related to both the overall fuel cell water management and the specific challenges within the GDL.

1.2.1 Fuel Cell Thermodynamics

As the reaction presented in Eqn. 1.4 is exothermic, the heat of reaction can be calculated by:

$$\Delta H = (h_f)_{H2O} - (h_f)_{H2} - 1/2(h_f)_{O2} \quad (1.5)$$

where h_f is the heat of formation for each chemical species [4]. Using heating values at standard conditions, the heat of reaction is calculated to be -286 kJ mol^{-1}. Due to entropy, not all of this produced energy can be turned into electricity. Therefore, the total potential energy available is the Gibbs free energy:

$$\Delta G = \Delta H - T\Delta S \quad (1.6)$$

After this correction, the potential energy of the system is reduced to -238 kJ mol^{-1}. This value can then be related to electrical work through:

$$W_{elec} = nFE = -\Delta G \quad (1.7)$$

where n is the number of electrons transferred (for H_2 n = 2), F is Faraday's constant (96,485 C mol^{-1}) and E is potential (V). This can then be rearranged to solve for the maximum theoretical voltage, or the equilibrium cell potential, which at standard conditions is [4]:

$$E_0 = -\Delta G/_{nF} = {237{,}340\ J\ mol^{-1}}/{2 \times 96{,}485\ C\ mol^{-1}} = 1.23\ V \quad (1.8)$$

1.2.2 Effect of Temperature and Pressure

Substituting the theoretical cell potential *E* (Eqn. 1.8) into the Gibbs free energy equation (Eqn. 1.6) leads to [4]:

$$E = -\left(\Delta H/_{nF} - T\Delta S/_{nF}\right) \quad (1.9)$$

From this equation, it can be seen that an increase in cell temperature will result in a decrease in the theoretical cell potential, since both *ΔH* and *ΔS* are both negative and are both known to increase with temperature based on heat capacity. For example, an increase of cell temperature to 65°C from 25°C results in a loss of 0.03 V. Although this may indicate that it is advantageous to run a fuel cell at as low of a temperature as possible, as will be detailed later an increase in temperature decreases kinetic losses such that any loss in theoretical voltage is more than overcome.

A similar analysis can be done as to the effect of pressure on the theoretical cell potential. To start, for an isothermal process the change in Gibbs free energy in molar quantities is expressed by:

$$\left(d(\Delta\hat{g})/_{dp}\right)_T = \Delta\hat{v} \quad (1.10)$$

where $\hat{v}$ is the molar volume. If the theoretical cell potential *E* (Eqn 1.8) is again substituted in for *G*, an expression for how the voltage varies with pressure is obtained:

$$\left(dE/_{dp}\right)_T = -\Delta\hat{v}/_{nF} \quad (1.11)$$

Assuming the ideal gas law, this equation then becomes:

$$\left({dE}/{dp}\right)_T = -{\Delta n_g RT}/{nFp} \quad (1.12)$$

where n_g is the change in the total number of moles of gas. From this result, it can be seen that similar to temperature, pressure has a minimal effect on the theoretical voltage potential. However, it is key to note that increasing the pressure results in an increase in the theoretical potential. For example, pressurizing the H_2 to 3 atm and O_2 to 5 atm results a 15 mV increase in the theoretical voltage.

Returning to Eqn 1.10 and integrating based on the ideal gas law derives an equation that relates changes in both temperature and pressure to the Gibbs free energy, given by:

$$G = G_0 + RTln\left({P}/{P_0}\right) \quad (1.13)$$

For a general reaction with two reactants and two products, denoted by aA + bB ↔ cC + dD, Eqn. 1.13 can be rewritten based on partial pressures as:

$$G = G_0 + RTln\left(\frac{\left({P_C}/{P_0}\right)^c\left({P_D}/{P_0}\right)^d}{\left({P_A}/{P_0}\right)^a\left({P_B}/{P_0}\right)^b}\right) \quad (1.14)$$

which is known as the Nernst equation, where P_0 = 1 atm. If this is applied to a fuel cell, it becomes:

$$G = G_0 + RTln\left({P_{H2O}}/{P_{H2}P_{O2}^{0.5}}\right) \quad (1.15)$$

If this is then re-written using the relation between Gibbs free energy and the theoretical fuel cell voltage, this becomes:

$$E = E_0 + {RT}/{nF}\, ln\left({P_{H2}P_{O2}^{0.5}}/{P_{H2O}}\right) \quad (1.16)$$

which fully describes the relation of temperature and pressure with the theoretical fuel cell voltage [4].

1.2.3 Theoretical Efficiency

As mentioned previously, one of the perceived benefits of fuel cells is their potential for high efficiency. The maximum theoretical efficiency at standard conditions can be found by:

$$\varepsilon_{thermo} = {\Delta G_0}/{\Delta H_0} = {-237.3\ kJ\ mol^{-1}}/{-286\ kJ\ mol^{-1}} \quad (1.17)$$

or 83%. In comparison, the maximum efficiency for a Carnot cycle is defined by:

$$\varepsilon_{Carnot} = {(T_H - T_L)}/{T_H} \quad (1.18)$$

In this expression, T_H is the maximum temperature and T_L is the rejection temperature, so a heat engine operating at 250°C with a rejection temperature at 50°C would have an efficiency of only 38%. For a heat engine, it can be seen that increasing T_H improves the theoretical efficiency. In contrast, the theoretical efficiency of a fuel cell decreases with increasing temperature, since the Gibbs free energy will decrease faster than the enthalpy. After 100°C (at standard pressure), this decrease is less pronounced, due to the difference in entropy between liquid water and water vapor [4].

1.2.4 Practical Fuel Cell Performance

In reality, the actual potential of a fuel cell is lower than the theoretical potential described above. Even before any current is drawn, the open circuit voltage (OCV) of a

fuel cell is generally between 0.95 and 1.0 V (vs. E_0 =1.23 V) [5]. This initial loss is due to fuel crossover, or hydrogen passing through the membrane without reacting. Additional losses that occur as more current is drawn can be divided into three groups: kinetic losses, ohmic losses, and concentration losses, and are also known as overpotentials, η_{act}, η_{ohmic}, and η_{conc} respectively. These three groups of losses can be visualized within the most common fuel cell diagnostic test, a polarization curve, where voltage and power are presented as a function of current density. Of note, it is standard with electrochemical reactions to report a current density (mA cm^{-2}) rather than the current. This is because electrochemical reactions occur at an interface, therefore doubling the surface area for the reaction should double the amount of electrons being transfered. This also allows for fuel cells of different sizes to be more readily comparable. An example of a hypothetical polarization curve is presented in Figure 2.

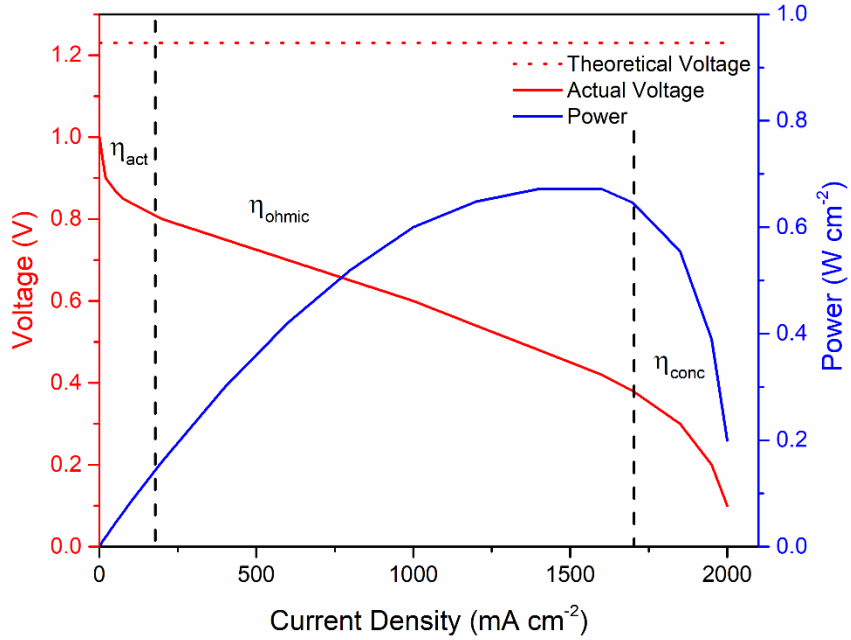

Figure 2. Example of a hypothetical polarization curve with theoretical voltage, actual voltage, and power displayed. The regions where the different overpotentials dominate are highlighted.

A review of these three groups of losses is provided in the following sections, but briefly the activation or kinetic losses are due to the electrode kinetics in the low current region, the ohmic losses are predominant in the medium currents and are due to the resistance of transport of ions and electrons, and the concentration losses occur at high currents and are due to reactant depletion at the catalyst surface. The following sections derive the overall expression describing the voltage behavior observed in a typical polarization curve, presented here [5]:

$$E_{cell} = E_{therm} - {}^{RT}/_{\alpha F}\, lo\, g\left({}^{i}/_{i_{0,C}}\right)_{kinetic} - iR_{T\,ohmic} - {}^{RT}/_{nF} \ln\left({}^{i_L}/_{i_L - i}\right)_{conc}$$

(1.19)

where E_{therm} is the predicted potential based on the thermodynamics (Eqn. 1.16) at the operating conditions being used.

1.2.5 Kinetic Losses

Kinetic losses refer to losses to the theoretical voltage due to the kinetics of the electrochemical reaction. This first type of voltage loss occurs at low currents (0 – 100 mA cm^{-2}) and is the voltage loss is due to the kinetics of the electrochemical reaction, specifically the mechanisms by which the electron transfer processes occur. In effect, the kinetic loss is the voltage sacrificed to get the overall electrochemical reaction started, which is also known as the activation polarization. These losses are immediately observed when any current is drawn from the fuel cell. This drop in voltage directly corresponds to the exchange current density, which is an electrochemical analog to the rate constant used to describe various chemical reactions, with a key difference in that it depends on the concentrations of the reactants. This value is found within the Butler-Volmer equation, which describes electrochemical kinetics on both the cathode and anode side:

$$i = i_0 \left[\exp\left(\frac{-\alpha nF\eta}{RT}\right) - \exp\left(\frac{-(1-\alpha)nF\eta}{RT}\right)\right] \quad (1.20)$$

where i is the current density, i_0 is the exchange current density, α is the transfer coefficient, n is the number of electrons transferred, F is Faraday's constant, η is the voltage loss, R is the gas constant, and T is temperature [4]. The Butler-Volmer equation shows that there is an exponential relationship between the voltage loss η and the amount of current being drawn from the electrochemical reaction. Practically, this states that as more current is drawn, there is an unavoidable loss in voltage. The Butler-Volmer

equation above is expressed for both the anode and the cathode. But, as the oxygen reduction reaction kinetics are slower than the hydrogen oxidation kinetics, meaning the exchange current density of the anode is several orders of magnitude larger, the overpotential of the cathode is much larger than that of the anode. This is because during practical fuel cell operation dictates that a net current is produced. Thus the forward-reaction direction dominates and the anode contributions can then be neglected and Eqn. 1.19 reduces to:

$$i = i_{0,C} \exp\left(\frac{-\alpha nF\eta}{RT}\right) \quad (1.21)$$

This equation can then be rearranged to solve for the activation overpotential, leading to:

$$\eta_{act} = {}^{RT}/_{\alpha nF} \ln({}^{i}/_{i_{0,C}}) \quad (1.22)$$

which can be further generalized to:

$$\eta_{act} = a + b\, log(i) \quad (1.23)$$

which is known as the Tafel equation, where a = -2.3 ($RT/\alpha F$) log($i_{0,C}$) and b = 2.3 ($RT/\alpha F$). The 'b' term is known as the Tafel slope. Importantly, at any fixed temperature the Tafel slope only depends on the transfer coefficient α, which for hydrogen fuel cells is generally reported to be between 0.2 and 0.5. The utility of the Tafel equation is that it allows for the experimental measurement of both α and $i_{0,C}$, which correspond to the slope and the x-intercept, respectively. Of note, the Tafel equation can only be applied while the relation between η_{act} and ln(i) is linear. At these low current densities, fuel crossover, where hydrogen directly diffuses through the membrane without reacting electrochemically, causes an additional loss in cell voltage. As such, the total electrical current is the sum of the external (useful) current and the current losses due to this

crossover, or $i = i_{ext} + i_{loss}$. Taking this into consideration, an expression for the actual cell potential at low current densities (i < 100 mA cm^{-2}) is:

$$E_{cell} = E_{therm} - {}^{RT}/_{\alpha F}\ log({}^{i_{ext} + i_{loss}}/_{i_{0,C}}) \quad (1.24)$$

1.2.6 Ohmic Losses

Ohmic losses refer to the reduction in cell potential due to the resistance of flow of ions through the membrane and electrons through the fuel cell components towards the external circuit. These losses can be directly expressed by Ohm's Law:

$$\eta_{ohmic} = iR_T \quad (1.25)$$

where R_T is the total internal cell resistance. This total resistance is the sum of the ionic, electronic, and contact resistances found within the cell, or the sum of all resistance found between the two current collectors. In general, electronic resistances within the fuel cell are negligible when compared to the ionic and contact resistances, which are on the same order of magnitude. Total internal resistance values typically range between 0.1 and 0.2 Ω cm^2 [5].

1.2.7 Concentration Losses

Concentration losses refer to the loss in cell potential due to concentration gradients between the bulk gas and catalyst surface, which arise due to the rapid consumption of reactants. As reviewed previously, electrochemical potential changes with the partial pressures of the reactants, this relationship is described by the Nernst equation:

$$\eta_{conc} = {}^{RT}/_{nF}\ ln\left({}^{C_B}/_{C_S}\right) \quad (1.26)$$

where C_B and C_S are the bulk and surface concentrations, respectively. From Fick's Law, the flux of reactant is proportional to the concentration gradient:

$$N = \left({D(C_B - C_S)}/{\delta} \right) A \quad (1.27)$$

where N is the flux of reactants, D is the diffusion coefficient of the reacting species, A is the electrode active area, and δ is the diffusion distance. At steady state, the consumption rate of the reactant by the electrochemical reaction is equal to the diffusion flux. Faraday's law relates the current density to the amount of charge transferred and the consumption of reactant (or production of product) per unit area:

$$i = {nFN}/{A} \quad (1.28)$$

Fick's law can then be combined with Faraday's law, leading to:

$$i = {nFD(C_B - C_S)}/{\delta} \quad (1.29)$$

Thus, as more current is produced the reactant concentration at the catalyst surface decreases. When the surface concentration reaches zero, the rate of the reaction has exceeded the rate of diffusion, effectively defining a limiting current density:

$$i_L = {nFDC_B}/{\delta} \quad (1.30)$$

Using this result, the concentration polarization can be defined as:

$$\eta_{conc} = {RT}/{nF} \ln \left({i_L}/{i_L - i} \right) \quad (1.30)$$

which describes the exponential drop seen at the end of the polarization curve in Figure 2. Combining this with the equations derived for the other two losses (Eqns 1.23 and 1.24) leads to Eqn 1.19, which describes all of the voltage losses observed in a polarization curve [5].

1.2.8 PEM Fuel Cell Components

Shown previously in Figure 1, the main components of a PEM fuel cell include the current collector plates, gas flow channels, and the MEA, comprised of the two GDLs and the CCM. This section briefly reviews the function and properties of each of these layers, starting with the membrane and working out.

The requirements of the membrane are high proton conductivity, minimizing the crossover of the fuel and reactant gases, and also being stable both mechanically and chemically in the PEM environment. The best known and most commonly used membrane (and membrane used in this work) is currently Nafion™, made by Dupont, which is comprised of perfluoro-sulfonylfluoride ethyl-propyl-vinyl ether. The proton conductivity of the membrane is strongly dependent on its water content, so proper membrane hydration is key to optimal fuel cell performance [5].

Water transport across the membrane occurs through various mechanisms. Electroosmotic drag occurs due to the protons dragging water as they move across the membrane (anode to cathode) and can be expressed by:

$$N_{H2O,drag} = \xi(\varphi)\, {}^{i}/_{F} \quad (1.31)$$

where ξ is the electroosmotic drag coefficient and is a function of membrane hydration φ. In addition to electroosmotic drag, both diffusion and hydraulic permeation take place, generally in the cathode to anode direction, and can be expressed by:

$$N_{H2O,diff} = D(\varphi)\, {}^{\Delta c}/_{\Delta z} \quad (1.32)$$

and

$$N_{H2O,hyd} = k_{hyd}(\varphi)\, {}^{\Delta P}/_{\Delta z} \quad (1.33)$$

respectively [5]. Based on operating conditions, the net water flux can favor either the anode or cathode side, largely dependent on the difference between diffusion and electroosmotic drag. However, the experimental measurement and separation of these different fluxes is very difficult, due to the architecture of the fuel cell and relatively small magnitudes of each of the terms. Experimental work has shown that the direction of the net cell water flux can change based on a variety of parameters, including humidification of the anode and cathode, temperature and pressure of the cell, and the operating current density [6].

There is a thin catalyst layer on either side of the membrane where the respective reactions take place. The most common catalyst used in PEM fuel cells is platinum, and current loadings generally range between 0.3-0.4 mg cm^{-2}. Most of the improvements as far as cost reduction are concerned are based around reducing the platinum loading required for fuel cell operation [2].

The GDLs located on either side of the CCM are responsible for several important functions for the fuel cell including: facilitating the transport of reactants to the CCM, facilitating the transport of product water to the gas flow channels, transporting electrons between the current collectors and CCM, conducting heat between the flow field and the CCM, and providing mechanical support to the MEA to prevent any sagging or intrusion into the gas flow channels. To this end, the GDL must be porous to allow the transport of the various species, while remaining both electrically and thermally conductive and mechanically rigid. As this layer is the focus of this thesis, a more detailed review on specifications, substrate materials, and material properties can be found in section 1.4.

The gas flow channels are responsible for distributing the reactants evenly across the active area and efficiently removing product water, while also being electrically conductive and chemically stable in the fuel cell environment. As such, this layer is commonly made from graphite. The specific geometry used in flow fields is an evolving field, but some common variations include serpentine channels, parallel channels, and interdigitated channels, displayed in Figure 3.

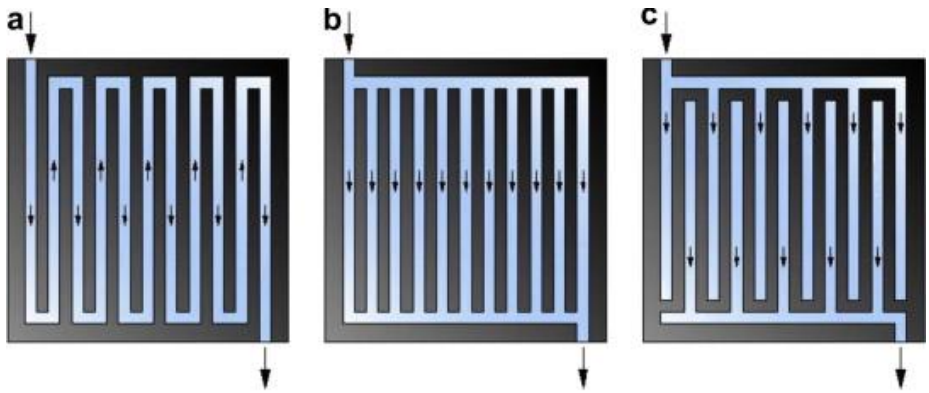

Figure 3. Common fuel cell gas flow field geometries a) single serpentine b) parallel c) interdigitated. (reprinted with permission from [7]).

Each geometry has its own advantages and challenges. For example, interdigitated channels promote secondary flow through the GDL at the expense of higher pressure drops, while parallel channels feature low pressure drops, but can suffer from flow maldistribution when one or more of the channels is blocked by a water droplet. The flow field geometry used in this work is a single-serpentine channel, which also promotes secondary flow patterns due to its U-shaped bends and pressure gradients between channels but avoids water blockage problems, since there is only one channel and any blockages would be removed by the resulting increase in pressure [8]. Figure 4 shows the

graphite flow field plates and an example of a fabricated MEA used in the active fuel cell testing for this thesis.

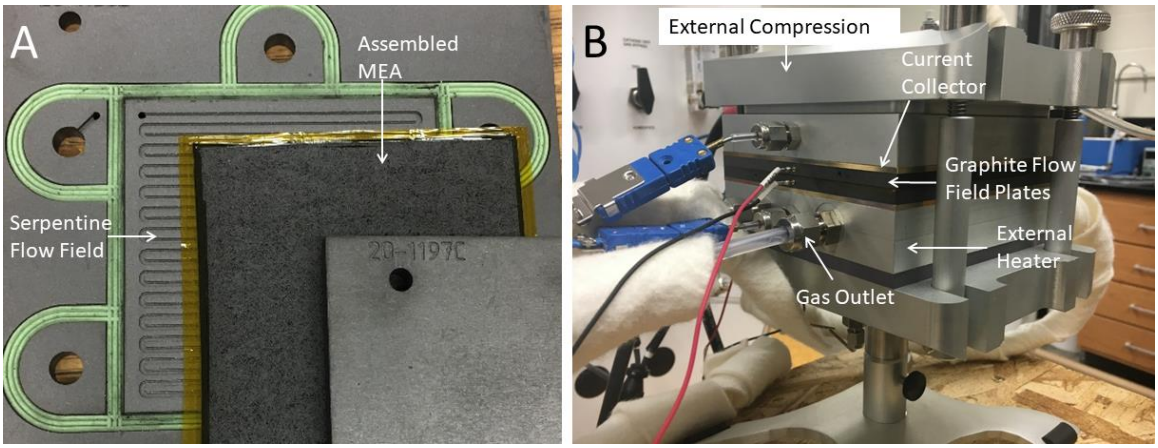

Figure 4. A) Graphite flow field plates and an MEA used for this study and B) fully assembled fuel cell. The flow field features 26 bends with dimensions of 1.57 mm (w) x 0.99 mm (d) for the cathode and 1.27 mm (w) x 0.51 mm (d) on the anode.

Typical channel dimensions range from 0.5-2.0 mm (w) and 0.5-1.5 mm (d) [8]. The spacing between the channels can also be modified, with wider channels promoting more reactant flow into the GDL and more available area for water removal, and wider ribs facilitating both heat and electron conduction. However, if the channel is too wide the MEA will begin to intrude into the flow field, and a wide rib provides more area for water accumulation.

1.2.9 Operating Conditions

The main operating conditions that can be manipulated during fuel cell operation are gas flow rates and relative humidities, the pressures and temperatures of both gases, and the overall cell temperature and compression pressure. The influence of pressure and temperature on the thermodynamics of the cell have already been detailed, but are

summarized here considering any additional positive or negative effects that they may have on the operating voltage.

An increase in pressure increases cell potential via the Nernst equation by increasing the surface reactant concentration, which leads to an increase in the exchange current density. However, while increasing the operating pressure may increase the potential of the cell, it increases the parasitic losses from the required compressor. Importantly, a change in pressure also plays an important role in the water management of the cell as it has an effect on the densities, velocities, and water carrying capacity of the gases as well as influencing the breakthrough pressure for any water droplets exiting the GDL. Similarly, although a fuel cell can function at ambient temperature, they are generally operated near 75°C, which serve to help with water management by exponentially increasing the water vapor pressure as well as helping to reduce kinetic losses by reducing the activation overpotential. Although the reaction is exothermic, maintaining the cell at a specific temperature requires external heating or cooling. Relatedly, this exothermic characteristic creates temperature gradients throughout the cell, with gradients shown to be as large as 5°C from the CCL to the flow field plates [9], making the accurate measurement of the cell's temperature difficult.

Although the gas flow rate is a variable that can be manipulated, it is largely dictated by the desired current to be drawn and therefore dictated by Faraday's Law, which for the two reactants are:

$$N_{H2} = {iA}/{2F} \quad N_{O2} = {iA}/{4F} \quad (1.34)$$

In reality, the cell is supplied with an excess of gas to ensure that gas concentrations remain high, and in the case of the cathode to assist with the removal of product water. The ratio of supplied gas to required gas is known as the stoichiometric ratio and is expressed as:

$$\lambda = {N_{supplied}}/{N_{needed}} \quad (1.35)$$

Typical stoichiometries for the anode and cathode are λ = 1.5 and 2, respectively. The cathode is run at a larger stoichiometry largely because the oxygen is generally supplied via compressed air [5].

As optimal fuel cell performance requires a fully hydrated membrane, the gas streams are typically humidified before entering the fuel cell. However, the balance between proper membrane hydration and cell flooding, which can lead to cell degradation or total failure, is a complex problem that depends on system design and operating conditions. The following section explains the general background of water management, and more detailed literature reviews on the topic can be found in the introductions of Chapters 2-4.

1.3 Water Management Review

To maintain optimal PEM fuel cell performance, there must be a certain amount of water within the MEA to maintain the membrane hydration and promote the ionic conductivity, while not reaching a point wherein the fuel cell becomes flooded, where reactant transport becomes impeded, effectively starving the reaction and potentially leading to total cell failure. Water management refers to the manipulation of operating

conditions and material properties, or the implementation of control schemes, to actively prevent the fuel cell from flooding or dehydrating. In order to manage water within the fuel cell, it is important to understand the common areas of water accumulation and the different ways it can be transported throughout the cell. Figure 5 displays a summary of the different water fluxes occurring within the fuel cell.

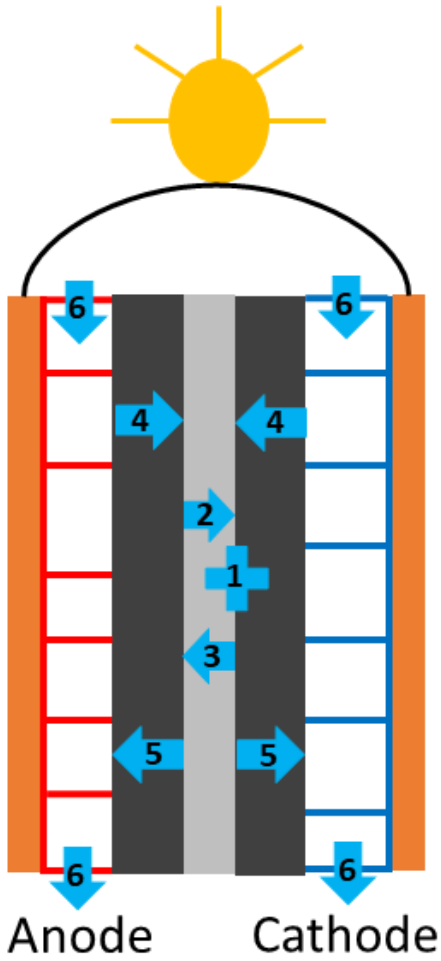

Figure 5. Summary of potential water fluxes within a fuel cell: 1) Reaction product water 2) Electroosmotic drag 3) Hydraulic permeation 4) Diffusion/condensation (accumulation) 5) Diffusion/evaporation 6) Convection

The water production rate can also be determined by Faraday's Law to be:

$$N_{H2O} = {}^{iA}/_{2F} \quad (1.36)$$

As liquid water is both produced on the cathode side and continually dragged across the CCM to the cathode via electroosmotic drag (Eqn 1.29), flooding is generally most severe on the cathode side. As water accumulates within the GDL, capillary pressure can force water into the gas channels. This accumulated liquid water can be removed convectively if it remains as a liquid or by evaporation into the cathode flow stream. As discussed, water can be transported from the cathode to anode via both diffusion and hydraulic permeation (Eqns 1.32 and 1.33). Water is also introduced into the fuel cell by the gas flow streams, since both are generally humidified [5]. A more thorough review of state-of-the-art techniques and recent literature can be found in the introductions of Chapters 2-4, the focus of the following sections is to introduce general topics and approaches.

1.3.1 Active Mitigation

Numerous studies have been conducted trying to either prevent the fuel cell from heading towards the flooded state, or more reactive strategies that attempt to mitigate and remove excess water after identifying that the cell is heading towards the flooded state. These strategies utilize techniques ranging from intelligent engineering of various PEM components, including the development of novel GDLs and flow field designs, to model-based process flow controllers, which react to signal analysis of pressure drops or voltage signals [10]. For example, recently proposed nanocrack-regulated self-humidifying membranes have been shown to inhibit water desorption, preserving ionic conductivity [11]. Additionally, a control-oriented model of a membrane humidifier was developed,

and experimentally validated, to maintain appropriate humidification on the cathode side of an operating fuel cell [12]. Finally, a group has recently proposed and experimentally tested a dual recirculation system to allow the fuel cell to self-humidify in a cold start-up setting [13].

1.3.2 Modelling Efforts

Various modeling strategies have been implemented to try to better understand the fundamental behavior that governs water accumulation and transport throughout the fuel cell. Volume-of-fluid methods, which track the surface of droplets, are regularly implemented to study the multiphase flow that takes place in the gas channels. Pore network models, which are able to model the GDL as a network of pores and throats and can accurately capture phase changes and multiphase flow, have been used to study where water accumulation is likely to occur within the fuel cell's porous media. The lattice Boltzman method has also been used to create pore-scale dynamic simulations of water transport through the GDL, though recent work has questioned whether the method is applicable to this specific media (detailed in Chapter 4) [14, 15].

1.3.3 GDL Visualization Strategies

Multiple visualization tools have been used to better understand the water transport as well as to generate data sets that could be used to validate findings from modeling based approaches. Neutron radiography utilizes a neutron beam, similar to how x-ray radiography works, but with the advantage that the neutrons can pass through materials that generally reflect x-rays, such as metals. This is especially beneficial for

fuel cells as the current collectors are generally made out of metal. This makes neutron radiography especially useful for conducting through-plane experiments of active fuel cells. One of the drawbacks to neutron radiography is its general low resolution when compared to X-ray based techniques [16].

The expanding availability of lab-top micro-CT scanners has made visualization experiments much more accessible. These scanners have been used to investigate and quantify water accumulation and desaturation within the GDL in non-active fuel cells by generating 3-D images. The main constraint to these devices is that the region of interest is relatively small, which means samples studied must be small enough to interface with the device ($D_{sample} < 5$ mm) [16].

Synchrotron radiography is a subset of X-ray radiography that utilizes a particle accelerator to generate a source of extremely high energy electrons. This powerful source allows for the generation of high X-ray fluxes, which provides higher spatial and temporal resolution, phase contrast, as well as lower scanning times than usually obtained by traditional X-ray radiography. A synchrotron is a combination of an electron gun, linear accelerator, booster rings, and storage rings that generate electrons producing light that is one million times brighter than the sun. Synchrotron radiography has been used in PEM fuel cell water management research to observe both active fuel cell behavior as well as non-active setups. Similar to micro-CT scanners, synchrotron radiography can also be used to generate 3-D images via X-ray computed tomography (X-ray CT) [16]. The main constraint to synchrotron radiography is the relatively high demand and limited

access available to these facilities; to date there are only 50 active synchrotron facilities in the world [17].

1.4 Gas Diffusion Layer Review

As mentioned, the GDL is a thin porous media responsible for transporting reactants to the CCM and water to the gas flow channels, conducting electrons, and providing mechanical support to the MEA. The thin characteristic refers to the fact that the average pore size is of a similar order of magnitude as the thickness of the layer itself (L_{GDL} = 100-400 μm, $D_{GDL\text{-}Pore}$ = 1-100 μm). The most commonly used GDL substrate is carbon fiber paper, which is a highly anisotropic material with characteristics generally ranging between 70-80% porosity and 170-400 μm thickness. Figure 6 shows microscopic images of the material.

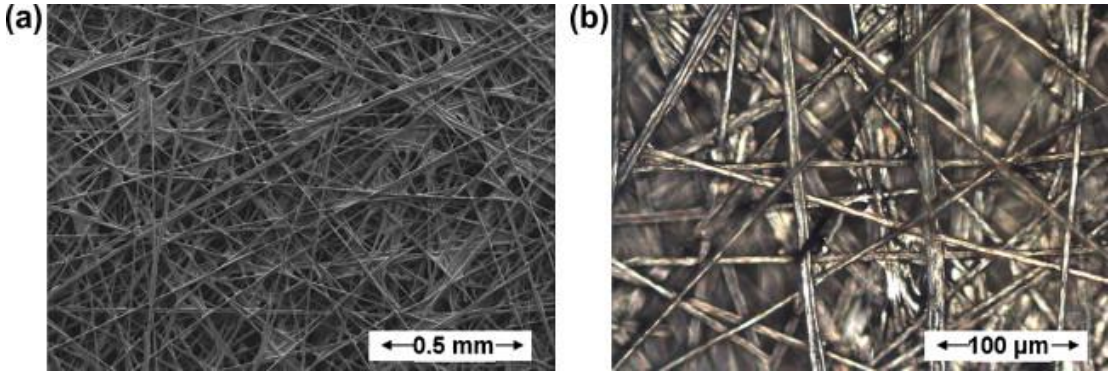

Figure 6. Microscopic images of carbon paper GDL, showing individual carbon fibers and the connecting binder (reprinted with permission [18]).

As the carbon fiber paper is naturally hydrophilic, PTFE treatment is commonly added to increase the hydrophobicity of the material (5-20% by weight) that helps to reduce potential flooding. Additionally, it was found that adding a highly hydrophobic

microporous layer (MPL), generally made of PTFE bound with carbon black, helps to further improve performance by both wicking water away from the CCM and improving electrical contact with the catalyst layer [19]. Recent investigations have looked into using alternative substrates for GDLs such as electrospun nanofibers and metal based GDLs. Electrospun GDLs allow for the intelligent engineering and control of pore size and fiber diameter, allowing for the creation of a more isotropic substrate as compared to typical carbon fiber paper GDLs; however these GDLs are both time consuming and costly to manufacture [20]. Similarly, metal based GDLs, such as metal foams, metal meshes and micro-machined metal, can also provide a more homogenous and controlled pore size distribution, but are subject to corrosion from the gas streams [21]. Liquid water transport in this media is governed by capillary pressure and viscous forces [22], while the vapor transport can be described by both convection and diffusion [23].

1.4.1 Effect of Material Properties on Cell Performance

The porosity of the GDL allows for the transport of the reactant gases and the removal of product water. However, as the GDL is also responsible for providing mechanical support and transporting electrons, there is a limit to how porous the layer can be. Similarly, the permeability dictates how easily liquid water can pass through the GDL, but gas bypass from one channel to the other has been shown to have dependence on this parameter [19]. It should be noted that as this layer has different structures in the in-plane (x, y directions) and through plane (z direction), permeability values have been measured to typically be higher in the in-plane direction, ~1×10^{-11} m^2 versus ~1×10^{-12} m^2 respectively [24, 25]. The amount of external compression on the GDLs affects its

porosity, permeability, percent saturation, and contact resistance. The over-compression of a GDL leads to quicker degradation due to a breakup of fibers and a deterioration of the hydrophobic coating. However, an under-compressed GDL leads to higher contact resistance, lowering its bulk conductivity and therefore increasing the full resistance R_T [19].

1.5 Preface

This thesis explores both the macroscale and microscale characterization of water transport in the GDL of a PEM fuel cell. Chapter 2 details a novel diagnostic protocol that characterizes water transport at the macroscale from the cathode to anode side in an active fuel cell. Results show that the net cell water flux can be quantified by calculating the relative humidity of the anode based on its pressure drop, effectively closing the overall cell water balance. As cathode flooding during active fuel cell testing predominantly occurs in the GDL, the microscale studies then investigate the desaturation process of a flooded GDL, described in Chapters 3 and 4. Key results from these efforts are that both evaporation and convection play a role in GDL desaturation, but that evaporation is the dominant component and is required for the GDL to reach full desaturation. Quantified results (Chapter 4) show that both percent saturation values and desaturation rates are largely heterogeneous across the domain, likely due to initial conditions, flow field geometry, and the natural anisotropic nature of the GDL. Chapters 2 and 3 are republications of work that has already been accepted and published in peer reviewed journals. Chapter 4 is a republication of work that is currently under review in a

peer reviewed journal. Finally, Chapter 5 provides overarching conclusions as well as recommendations for future work. Of note, each chapter has its own reference section, while a cumulative reference section in alphabetical order is provided after Chapter 5. Appendices A and B detail the protocols and scripts used for data collection and analysis in Chapter 2. Appendix C details the protocols and software used for the image reconstruction and analysis in Chapters 3 and 4. Appendix D is a summary of work currently in progress.

References

1. Fuel Cell Technologies Office Multi-Year Research, Development, and Demonstration Plan, D.o. Energy, Editor. 2012. p. 3.4-1 - 3.4-58.

2. Wang, Y., et al., A review of polymer electrolyte membrane fuel cells: Technology, applications, and needs on fundamental research. Applied Energy, 2011. 88(4): p. 981-1007.

3. Kirubakaran, A., S. Jain, and R.K. Nema, A review on fuel cell technologies and power electronic interface. Renewable and Sustainable Energy Reviews, 2009. 13(9): p. 2430-2440.

4. O'hayre, R., et al., Fuel Cell Fundamentals. 2006, Hoboken, New Jersey: John Wiley & Sons.

5. Barbir, F., PEM fuel cells: theory and practice. 2012: Academic Press.

6. Yau, T.C., et al., Water transport and Schröder's Paradox in fuel cell membrane electrode assemblies. Journal of Power Sources, 2013. 224: p. 285-289.

7. Manso, A.P., et al., Influence of geometric parameters of the flow fields on the performance of a PEM fuel cell. A review. International Journal of Hydrogen Energy, 2012. 37(20): p. 15256-15287.

8. Aiyejina, A. and M.K.S. Sastry, PEMFC Flow Channel Geometry Optimization: A Review. Journal of Fuel Cell Science and Technology, 2011. 9(1): p. 011011-011011-24.

9. Djilali, N. and D. Lu, Influence of heat transfer on gas and water transport in fuel cells. International Journal of Thermal Sciences, 2002. 41(1): p. 29-40.

10. Li, H., et al., A review of water flooding issues in the proton exchange membrane fuel cell. Journal of Power Sources, 2008. 178(1): p. 103-117.

11. Park, C.H., et al., Nanocrack-regulated self-humidifying membranes. Nature, 2016. 532: p. 480.

12. Solsona, M., C. Kunusch, and C. Ocampo-Martinez, Control-oriented model of a membrane humidifier for fuel cell applications. Energy Conversion and Management, 2017. 137: p. 121-129.

13. Jiang, H., et al., Experimental study on dual recirculation of polymer electrolyte membrane fuel cell. International Journal of Hydrogen Energy, 2017. 42(29): p. 18551-18559.

14. Andersson, M., et al., A review of cell-scale multiphase flow modeling, including water management, in polymer electrolyte fuel cells. Applied Energy, 2016. 180: p. 757-778.

15. Wu, H.-W., A review of recent development: Transport and performance modeling of PEM fuel cells. Applied Energy, 2016. 165: p. 81-106.

16. Bazylak, A., Liquid water visualization in PEM fuel cells: A review. International Journal of Hydrogen Energy, 2009. 34(9): p. 3845-3857.

17. Light Sources of the World. 2018, Lightsource.org: https://lightsources.org/lightsources-of-the-world/.

18. Wang, Y., et al., Stochastic modeling and direct simulation of the diffusion media for polymer electrolyte fuel cells. International Journal of Heat and Mass Transfer, 2010. 53(5): p. 1128-1138.

19. Cindrella, L., et al., Gas diffusion layer for proton exchange membrane fuel cells—A review. Journal of Power Sources, 2009. 194(1): p. 146-160.

20. Chevalier, S., et al., Novel electrospun gas diffusion layers for polymer electrolyte membrane fuel cells: Part I. Fabrication, morphological characterization, and in situ performance. Journal of Power Sources, 2017. 352: p. 272-280.

21. Park, S., J.-W. Lee, and B.N. Popov, A review of gas diffusion layer in PEM fuel cells: Materials and designs. International Journal of Hydrogen Energy, 2012. 37(7): p. 5850-5865.

22. Sinha, P.K. and C.-Y. Wang, Pore-network modeling of liquid water transport in gas diffusion layer of a polymer electrolyte fuel cell. Electrochimica Acta, 2007. 52(28): p. 7936-7945.

23. Owejan, J.P., et al., Water Transport Mechanisms in PEMFC Gas Diffusion Layers. Journal of The Electrochemical Society, 2010. 157(10): p. B1456-B1464.

24. Gurau, V., et al., Characterization of transport properties in gas diffusion layers for proton exchange membrane fuel cells: 2. Absolute permeability. Journal of Power Sources, 2007. 165(2): p. 793-802.

25. Gostick, J.T., et al., In-plane and through-plane gas permeability of carbon fiber electrode backing layers. Journal of Power Sources, 2006. 162(1): p. 228-238.

CHAPTER TWO

QUANTIFYING CATHODE WATER TRANSPORT VIA ANODE HUMIDITY MEASUREMENTS IN A POLYMER ELECTROLYTE MEMBRANE FUEL CELL

Contribution of Authors and Co-Authors

Manuscript in Chapter 2

Author: Logan Battrell

Contributions: Conceived and designed experiments, performed experiments, analyzed data, wrote the manuscript

Co-Author: Aubree Trunkle

Contributions: Performed experiments

Co-Author: Erica Eggleton

Contributions: Performed experiments

Co-Author: Lifeng Zhang

Contributions: Conceived and designed experiments, edited earlier manuscripts

Co-Author: Ryan Anderson

Contributions: Conceived and designed experiments; analyzed data; provided materials and analysis tools; edited manuscripts

Manuscript Information

Logan Battrell, Aubree Trunkle, Erica Eggleton, Lifeng Zhang and Ryan Anderson

Energies

Status of Manuscript:
____ Prepared for submission to a peer-reviewed journal
____ Officially submitted to a peer-reviewed journal
____ Accepted by a peer-reviewed journal
_X_ Published in a peer-reviewed journal

MDPI
Vol 10, Issue 8, 1222, August 2017
https://doi.org/10.3390/en10081222

QUANTIFYING CATHODE WATER TRANSPORT VIA ANODE HUMIDITY MEASUREMENTS IN A POLYMER ELECTROLYTE MEMBRANE FUEL CELL

Abstract

A relative humidity (RH) measurement based on pressure drop analysis is presented as a diagnostic tool to experimentally quantify the amount of excess water on the cathode side of a polymer electrolyte membrane fuel cell (PEMFC). Ex-situ pressure drop calibration curves collected at fixed RH values, used with a set of well-defined equations for the anode pressure drop, allows for an estimate of in-situ relative humidity values. During the in-situ test, a dry anode inlet stream at increasing flow rates is used to create an evaporative gradient to drive water from the cathode to the anode. This combination of techniques thus quantitatively determines the changing net cell water flux. Knowing the cathodic water production rate, the net water flux to the anode can explain the influence of liquid and vapor transport as a function of GDL selection. Experimentally obtained quantified values for the water removal rate for a variety of cathode gas diffusion layer (GDL) setups are presented, which were chosen to experimentally vary a range of water management abilities, from high to low performance. The results show that more water is transported to the anode when a GDL with poor water management capabilities is used, due to the higher levels of initial saturation occurring on the cathode. At sufficiently high concentration gradients, the anode removes more water than is produced by the reaction, allowing for the

quantification of excess water saturating the cathode. The protocol is broadly accessible and applicable as a quantitative diagnostic tool of water management in PEMFCs.

2.1 Introduction

Polymer electrolyte membrane fuel cells (PEMFCs) are energy conversion devices featuring zero local greenhouse emissions, high power density, low operating temperature, and a rapid start up, making them attractive candidates for integration into vehicular and mobile applications [1]. Although there remain technical challenges related to hydrogen storage and distribution, as well as the robustness and durability of PEMFCs, the attractive benefits of widespread fuel cell adoption have driven continued research into this technology for the past few decades. One of the key issues affecting the short-term performance and the long-term durability of PEMFCs is water management [2]. Water is produced in an electrochemical reaction at the cathode, and to obtain maximal PEMFC efficiency, the membrane electrode assembly (MEA) must be kept within a window of optimal hydration. In order to obtain optimal cell performance, the water content within the cell must be maintained at a level such that the catalyst coated membrane (CCM) is well hydrated, so as to promote the ionic conductivity, yet to not reach a point where water accumulation begins to block or restrict the mass transport of the reactant gases to the catalyst sites. Either one of these extreme cases of overall cell hydration can cause degradation of key cell components, or even result in total cell failure [3,4]. Due to these reasons, proper water management is an extremely important aspect of fuel cell operation.

To this end, multiple strategies and material improvements have been made to help optimize water management within PEMFCs. Research groups have investigated reactive control strategies via signal analysis and the manipulation of operating conditions [5]. Hussaini et al. [6] demonstrated a dynamic external intermittent humidification scheme using a single serpentine flow field, as well as a multiple, parallel channel flow field. Song et al. [7] investigated the connection between the hydrogen pressure drop with the development of cathode flooding within a fuel cell and proposed a hydrogen purge scheme, along with humidification modification, as a water management scheme for an operating PEMFC. Damour et al. [8] developed a control scheme for an air flow controller to regulate membrane humidity and optimize PEMFC performance. Pahon et al. [9] proposed a signal-based fault diagnostic approach using relative wavelet energy to analyze signals from a 40-cell stack to identify abnormal or healthy operation. These signal-based approaches are based on reacting to a change in the voltage or pressure signal to identify the beginning of the flooding condition, and then modifying the flow conditions, namely the relative humidity (RH) of the flow streams, to move the fuel cell away from the flooded state. Research has also been done on the modification of material properties and structure of various PEMFC components. Alink et al. [10] investigated the effects on water management from machined and laser modifications to the porous layer and found that selective perforations to the cathode microporous layer (MPL) helped improve performance in both flooding and dry conditions. Chen et al. [11] studied the effect of different MPL compositions in relation to different air RH, and found that the MPL composition should be optimized in relation to the operating RH of

the cathode in order to maximize performance. Finally, Li et al. [12] investigated four different cathode types with varying structures and properties to study the relationship between their water management capabilities and electrochemical performance. They showed that a hydrophobic CCM and MPL assisted in membrane hydration while avoiding cell flooding. In addition, multiple models have been created with the aim to better understand the two-phase transport of water within the porous layer [13–15], at the catalyst layer and across the membrane [16,17], and within the gas flow channels [18,19]. Attempts have been made to model the relation between the cell water content to cell performance, showing that oversaturation or flooding on the cathode side leads to lower performance [20–22]. Understanding the water transport characteristics of the various PEMFC elements allows for the creation of more accurate numerical models, as well as the intelligent design of key components to help to intrinsically manage water accumulation within the cell. Numerous studies have investigated the water transport characteristics of these elements using a variety of methods. Yau et al. [23] determined that water crossover rates of MEAs placed in a non-operating fuel cell using a specially designed setup, which included infrared sensors and specific considerations for post fuel cell gas processing. Morgan and Datta [24] investigated how different gas diffusion layer (GDL) characteristics can effect diffusivity, as well as performance by using a specially designed water vapor diffusivity measurement tool. Chevalier et al. [25] were able to perform in-situ measurements of the effective diffusivity of a GDL using synchrotron X-ray radiography (Canadian Light Source facility, Saskatoon, SK, Canada).

One of the challenges facing both the experimental design space and modeling efforts is the accurate quantification of water within the cell, both in terms of where the water is accumulating and how it is transporting through various components of the cell. Methods to visualize liquid water within a PEMFC have been performed in-situ with X-ray radiography and neutron beam radiography, as well as a number of optical visualization experiments taken using a modified fuel cell structure [26]. Specifically, using synchrotron X-ray tomography Krüger et al. [27] qualitatively demonstrated the increasing GDL saturation that accompanies higher current density operation. Additionally, soft X-ray tomography was used by Deevanhxay et al. [28] to visualize the additional flooding between the GDL and the CCM when a MPL was not applied to the cathode GDL. Recently, Banerjee et al. [29] transiently visualized the increase in porous layer liquid water saturation accompanying the higher current densities. They found that the saturation level increased to a certain threshold, after which increasing the current density no longer increased the liquid water saturation. Owejan et al. [30] used neutron beam radiography to investigate water transport and accumulation in a 7% polytetrafluoroethylene (PTFE) hydrophobic treated GDL and found that the GDL could become 44% saturated before water began to be pushed into the gas channels. Using a modified fuel cell structure, Hussaini et al. [31] optically visualized cathode channel flooding to investigate two-phase flow properties and qualitatively showed voltage degradation under conditions that promoted flooding and oversaturation of the GDL. Owejan et al. [32] investigated the liquid and vapor transport mechanisms related to MPL characteristics ex-situ and studied how they affected performance in-situ.

In all cases, the studies either required highly specialized equipment, or the modification of the fuel cell architecture. Some efforts have been made to determine ‘flooding’ conditions in realistic fuel cells without the need for advanced techniques. One such protocol, Anode Water Removal (AWR), was previously shown to qualitatively identify poor cell performance due to cathode GDL flooding [33,34]. This method relies on the manipulation of an evaporative gradient created by running the fuel cell with a dry anode stream at systematically increasing flow rates. In situations prone to the accumulation of water on the cathode, a voltage increase was noted as the concentration gradient between the cathode and anode increased. However, that work did not quantify the amount of water transported out of the fuel cell and no quantitative link could be determined between the amount of excess water on the cathode and the cell’s performance. This was most likely not previously performed due to the difficulty in accurately measuring the anode RH within the highly specialized fuel cell environment. This paper addresses this challenge through the development of a novel pressure drop analysis to determine the anode RH.

In the present work, a combination of experimental techniques allows for the in-situ quantification of water removal from the cathode. The presented methodology provides a diagnostic tool to investigate and compare different GDL materials, allowing for the in-situ measurement and quantification of general water management capabilities, as well as providing insight into various water flux parameters. The AWR protocol is adapted to remove excess fuel cell water and then extended to quantify the amount of water that the protocol removes from the cell. A new method is presented where an anode

pressure drop calibration curve is used to determine pertinent flow parameters, allowing for the calculation of the RH of the anode stream. Although not as precise as previously discussed measurement techniques, the major advantage of the proposed method is the broad accessibility and quick-to-implement procedure, which allows for a rapid estimate of quantified water transfer and accumulation values. This is novel from other signal-based approaches, which generally investigate the in-situ pressure drop signal for patterns to identify flooding behavior. By monitoring the anode pressure drop during the AWR protocol, the resulting anode RH is calculated, leading to a determination of the rate of water removal from the cathode. The experimental setup, RH calculation, and data analysis procedures are detailed. Quantified water removal rates for three different MEA setups are presented along with the effect of temperature. The experimental data shows that this method is robust and reproducible.

2.2 Materials and Methods

This section details the experimental setup for PEMFC testing and the procedures for polarization curve testing, anode water removal tests, and the calibration of ex-situ pressure drops for use in the data analysis of in-situ pressure drops. Experimental tests for this study were all performed using a single TP50E Research PEM Fuel Cell (Tandem Technologies Ltd., Ludlow, MA, USA); specifications for this cell can be found in Table 1.

Table 1. TP50E Research Cell Specifications

Criteria	Description
Active Area	50 cm^2
Cathode Channel Dimensions	1.57 mm (w) × 0.99 mm (d)
Anode Channel Dimensions	1.27 mm (w) × 0.51 mm (d)
Compression Pressure	100 kPaG
Flow Field Design	Single serpentine channel
Flow Field Pattern	Semi Co-Flow

Fuel cell operating conditions were controlled via the FCATS G20 Single Cell Test Station (Model G20HF, Greenlight Innovation, Burnaby, BC, Canada). The G20 test station allowed for the continuous collection of voltage, pressure drop, and temperature data during all testing. The station controls set points and provides measurements for current or voltage (120 A, 50 V, 300 W), pressure (5–300 kPaG), temperature (up to 110 °C), inlet gas dew point (22–90 °C), hydrogen flow rate (0.05–5 NLPM), and air flow rate (0.1–10 NLPM). The variables measured for this study were voltage, pressure drop, and temperature. For these three variables the stations reported accuracy is ±0.005 V, ±2 kPa, and ±2 °C. All testing was performed using a Nafion NR-212 CCM (Ion Power, New Castle, DE, USA), which features a reported 0.3 mg cm^{-2} platinum loading on both anode and cathode sides. All GDLs investigated were from the Sigracet 25 line, specifications for which can be found in Table 2. Importantly, literature has shown the GDLs selected have a measurable effect on the saturation of the layer, making them useful benchmarks for this study [35].

Table 2. Sigracet 25 Gas Diffusion Layer (GDL) Line Specifications.

Sigracet Gas Diffusion Layer	% Polytetrafluoroethylene	Microporous Layer	Thickness (μm)	Porosity
25 BC	5%	Yes	235	0.80
25 BA	5%	No	190	0.88
25 AA	0%	No	190	0.88

Although the majority of fuel cell flooding intrinsically occurs on the cathode side, where the water is formed, and not on the anode, unless subjected to outside factors such as abnormally low temperature operating conditions [36,37], the anode GDL was universally tested with the 25 BC in order to ensure anode flooding did not confuse the cathode analysis.

2.2.1 Polarization Curve

The polarization curve was collected by increasing the current density from 0 to 1800 mA cm^{-2}, while maintaining the required flow rates for a constant cathode and anode stoichiometry of 2 and 1.5, respectively. The stoichiometry, λ, is defined as the ratio of reactant gas supplied to the cell to the needed amount for the electrochemical reaction to occur. The temperature was set at 75 °C and the inlet pressure was maintained at 206.9 kPaG. Specifically, the system monitors the inlet pressure and controls it using a backpressure regulator. The anode and cathode gases were both fully humidified (RH = 100%) before entering the fuel cell. The voltage at each current density point was determined by time averaging the voltage data collected over 10 min. Before collecting the polarization curve data, the membranes were conditioned at 75 °C and 206.9 kPaG for eight hours where the current density was increased from 600 mA cm^{-2} up to 1000 mA cm^{-2}, while maintaining cell voltage above 0.5 V.

2.2.2 Anode Water Removal

The basic testing protocol for AWR was adapted from previously published methods that focused on a qualitative analysis [38]. A brief summary is provided here. Initially, the cell was operated at a fixed current density (1000 mA cm^{-2}) with cathode and anode stoichiometry set at 2 and 1.5. The temperatures, inlet pressure, and inlet RH for both anode and cathode were $T_{cell} = T_{gas,inlet}$ = 75 °C or 85 °C, P_{inlet} = 206.9 kPaG, and RH_{inlet} = 100%. To initiate the AWR procedure, the anode flow stream was switched to 0% RH via a manual control valve. The flow rate was systematically increased every two minutes, the time period required for the voltage to reach a steady state, by increasing the anode stoichiometry set point. The duration of each set point was also consistent with the previously established protocol [33,34]. The test started with the standard anode stoichiometry set point of 1.5, and the first flow rate increase was to a stoichiometric value of two. The flow rate was then increased by one stoichiometric factor, up to a maximum value of 10. During PEMFC operation, water can accumulate within the GDL layer, or between the porous layer and the CCM, causing the voltage to drop. A schematic visualizing the different water fluxes present during this test can be seen in Figure 7. The applied concentration gradient causes a net water flux to the anode, highlighted via the arrow.

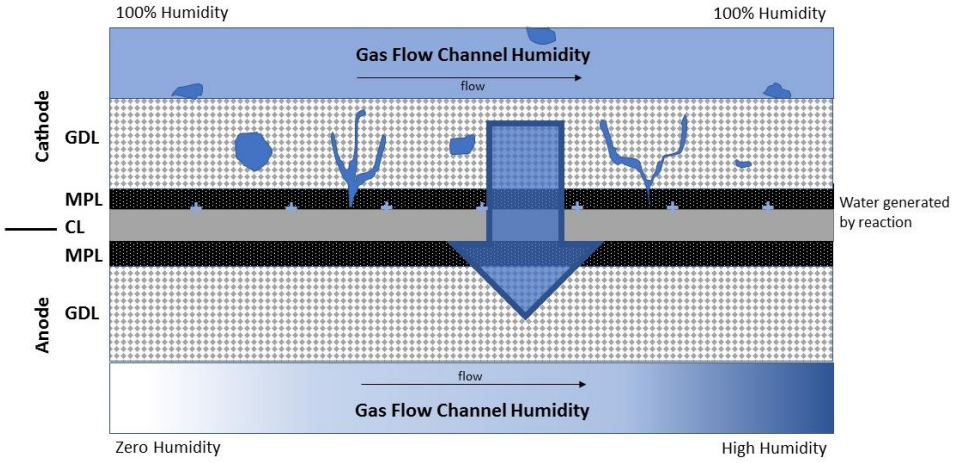

Figure 7. Experimental schematic showing liquid water accumulation and the main water vapor fluxes in the Anode Water Removal (AWR) procedure. As the anode flow rate increases, more water from the cathode is driven to the anode.

In between every AWR test, a reconditioning protocol was performed to re-establish a consistent initial voltage and rehydrate the CCM. This reconditioning protocol is similar to the polarization procedure described above; however, the current densities used were limited to 300 mA cm^{-2} through 1200 mA cm^{-2}.

2.2.3 Anode Pressure Drop Calibration Curve

Collecting data for the pressure drop calibration curves was performed using a similar protocol to the AWR protocol. The entire experimental setup remained the same, but the system was non-reacting. The CCM was replaced by a polyimide film of comparable thickness in order to prevent water vapor crossover from humidified gas flows. A GDL was placed on both sides of that film to represent accurate 'zero-saturation' behavior. The cathode flow rate was held steady while the other was raised systematically. The increases in flow rate for the anode stream were based on the stoichiometry factors as if the cell were operating at 1000 mA cm^{-2}. These tests were

repeated at varying set RH values, specifically 0%, 25%, 50%, 75%, and 100% RH. This set of data was then used to calculate set-up specific parameters related to the pressure drop, detailed below.

2.3 Quantification of *In-Situ* Data to Determine Average Anode Relative Humidity and Net Cell Water Flux

To determine the net water flux from cathode to anode, the experimentally measured pressure drop was used in conjunction with a set of equations for the pressure drop that are a function of the flow rate and RH.

2.3.1 *Ex-Situ* Determination of Set-up Specific Parameters Related to Pressure Drop

A detailed description of the assumptions and requirements for the implementation of the following equations has been thoroughly investigated by Barbir [39], and all of the equations presented in this section are from that reference. The pressure drop along the flow field channel from inlet to outlet (ΔP) for both the anode and cathode can be calculated using the equation for incompressible flow in a pipe:

$$\Delta P = f_{\mathrm{F}} \frac{L}{D_{\mathrm{H}}} \rho \frac{\bar{v}^2}{2} + \sum K_{\mathrm{L}} \rho \frac{\bar{v}^2}{2} \qquad (2.1)$$

where f_{F} is the friction factor, L is the channel length, D_{H} is the hydraulic diameter, ρ is the fluid density, $\bar{v}$ is the average velocity, and K_{L} is the loss coefficient. This coefficient accounts for the effects of the channel bends in the serpentine configuration. The friction factor was calculated from the following equation for laminar flow within a rectangular channel:

$$f_{\mathrm{F}} = \frac{55+41.5exp\left(\frac{-3.4}{w_c/d_c}\right)}{Re} \qquad (2.2)$$

where w_c and d_c are the channel width and depth, and Re is the Reynolds number, which was found to be laminar for all cases tested. The Reynolds number was calculated as

$$Re = {\rho\bar{v}D_H}/{\mu_{mix}} \qquad (2.3)$$

where μ_{mix} is the mixed fluid viscosity, calculated from

$$\mu_{mix} = \frac{\mu_1}{1+\psi_1({M_2}/{M_1})} + \frac{\mu_2}{1+\psi_2({M_1}/{M_2})} \qquad (2.4)$$

with

$$\psi_1 = \frac{\sqrt{2}}{4}\left(1 + \left({\mu_1}/{\mu_2}\right)^{0.5}\left({r_2}/{r_1}\right)^{0.25}\right)^2 (1 + {r_1}/{r_2})^{-0.5} \qquad (2.5)$$

and

$$\psi_2 = {\sqrt{2}}/{4}\left(1 + \left({\mu_2}/{\mu_1}\right)^{0.5}\left({r_1}/{\mathrm{r}_2}\right)^{0.25}\right)^2 (1 + {r_2}/{r_1})^{-0.5} \qquad (2.6)$$

where μ_1 and μ_2 are the viscosities of the pure gases, r_1 and r_2 are their respective volume fractions, and M_1 and M_2 are their molecular weights. The equation used to calculate μ_1 and μ_2 was

$$\mu = \mu_0\left(\frac{T_0+C}{T+C}\right)\left({T}/{T_0}\right)^{3/2} \qquad (2.7)$$

with μ_0 as a known viscosity at temperature T_0 and C being a fluid specific coefficient, with values of which can be found in the Appendix A Table A1. The fluid density was calculated as

$$\rho = \frac{(P-\emptyset\cdot P_{vs})Mw_{H2}+(\emptyset\cdot P_{vs})Mw_{H_2O}}{R\mathrm{T}} \qquad (2.8)$$

where P is the absolute pressure of the system (Pa), $Ø$ is the relative humidity (0–1), P_{vs} is the saturated vapor pressure (Pa) and Mw_{H2} and Mw_{H_2O} are the molecular weights of the hydrogen and water. The average velocity was calculated from the volumetric flow rate

$$Q = \frac{\mathrm{I}}{2F}\frac{\lambda_{H2}}{r_{H2}}\frac{RT}{(P-ø_{\mathrm{gas}}\cdot P_{vs})} \qquad (2.9)$$

where I is the current (A), F is Faraday's constant (C mol^{-1}), λ_{H2} is the stoichiometric flow rate value, and r_{H2} is the volume fraction of hydrogen. The volume fraction of water in a gas stream is calculated by

$$\mathrm{r}_{H_2O,Vol} = {ø_{\mathrm{gas}} \cdot P_{vs}}/{P} \qquad (2.10)$$

where the saturated vapor pressure is calculated by using the following equation, valid between 0 and 100 °C, with coefficients for which can be found in the Appendix A Table A2. It should be noted that a number of the above equations relate specifically to the geometry of the fuel cell used, and would require slight modification before their implementation to different systems. Generally, one would have to use whichever appropriate hydraulic diameter, as well as the specific experimental determination of K_L using the protocol outlined below.

$$P_{vs} = \exp(aT^{-1} + b + cT + dT^2 + eT^3 + f\ln(T)) \qquad (2.11)$$

Since several of these terms depend on the RH, this set of equations allowed for the pressure drop across the channel to serve as a quantitative estimate of the RH of the gas. The experimental ex-situ data collected at varying flow rates and relative humidities was then used to solve for the loss coefficient K_L, found in Equation (2.1). The determination of the local resistance term from the ex-situ data then allowed for the

calculation of the RH of each flow stream in the in-situ cases, thereby allowing for the quantification of the water leaving the fuel cell via the anode (as detailed in the following sections).

2.3.2 Quantification of *In-Situ* Data to Determine Anode Relative Humidity

Quantification of the in-situ pressure data was performed by solving for the anode RH; a summary of the steps taken by the solver can be seen in Figure 8. The routine functions by modifying the RH value until it has minimized the error between the calculated pressure drop and the experimentally measured value. This process is repeated for each stoichiometric set point on the anode, calculating the average RH value for each step. Specifically, the RH guess is used to update the viscosity terms (Equations (2.4)–(2.7)), fluid density (Equation (2.8)), and volumetric flow rate (Equation (2.9)). These are then used to calculate the Reynolds number (Equation (2.3)) and friction factor (Equation (2.2)), in order to determine the overall anode pressure drop (Equation (2.1)). The only modification to the equations presented above was the substitution of an averaged stoichiometric term into the volumetric flow rate in Equation (2.9). The average stoichiometric term is defined as the average of the inlet and outlet stoichiometric values, which accounts for the reduction in the mass flow rate due to the consumption of the reactant in the reaction.

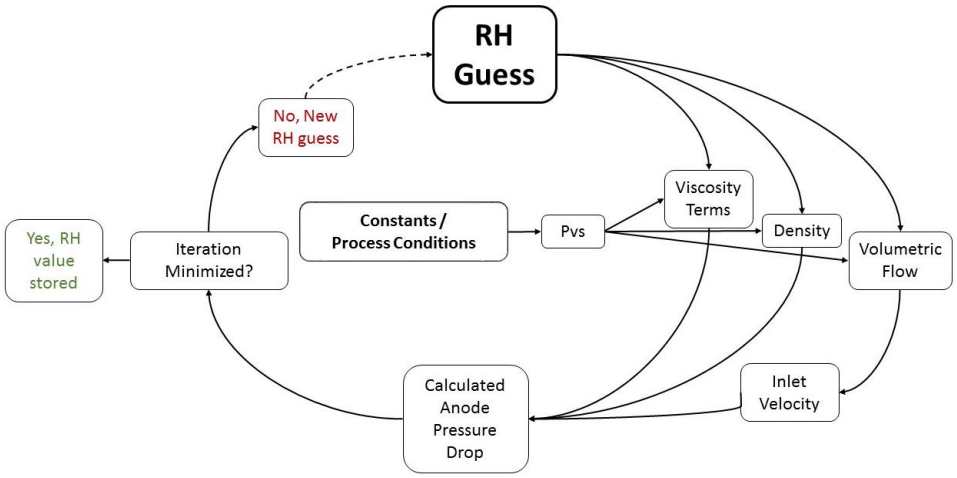

Figure 8. Iteration tree to determine the in-situ anode Relative Humidity (RH). An initial RH guess is used to determine all fluid physical properties and calculate the anode pressure drop. These are compared to the measured pressure drop and the iteration continues until the difference between the measured and calculated pressure drops is minimized.

2.3.3 Quantification of Net Cell Water Flux

Once the anode RH values had been determined, the water flux out of the cell from the anode stream could then be calculated, based on its set flow rate and pressure drop. The net cell water flux was determined by combining the anode, cathode, and reaction fluxes.

$$\dot{M}_{net,water} = \dot{M}_{reaction,water} - \dot{M}_{anode,water} - \dot{M}_{cathode,water} \qquad (2.12)$$

The reaction flux was calculated based on Faraday's law

$$\dot{M}_{reaction} = \frac{I}{2F} Mw_{H2O} \qquad (2.13)$$

resulting in a constant value for all anode flow rates. The anode water flux was calculated by first calculating the mixing ratio, *x* (g water vapor/g hydrogen) of water vapor to dry gas from

$$x = \frac{\mathrm{B}\,(\,\emptyset_{\mathrm{gas}} \cdot P_{vs})}{(P - \emptyset_{\mathrm{gas}} \cdot P_{vs})} \qquad (2.14)$$

where B is the constant 8.94 (g water vapor/g hydrogen). The mixing ratio can then be used with the outlet mass flowrate to determine the rate of water leaving the cell,

$$\dot{M}_{\kappa,water} = x\dot{M}_{\kappa,outlet} \qquad (2.15)$$

where κ indicates the anode or cathode. Since the excess water in the fuel cell is located on the cathode side, it was assumed that the cathode stream remained fully saturated at 100% RH. Due to the cathode pressure drop, this assumption leads to an additional water removal term. Although the magnitude of this contribution was less than 10% than that of the anode, it was included in the overall water balance calculation. The analysis was also performed without the cathode term and was found to have no effect on the overall analysis. The net cell flux was thus calculated from the balance between the calculated exit anode water flux, estimated exit cathode flux, and the produced water from the reaction. For the purpose of this study, a positive net cell water flux indicates that the cell is producing more water via the reaction than is being removed as vapor by the cathode and anode gas streams. A negative net cell water flux indicates that the water vapor being removed by the anode and cathode gas streams is greater than the amount of water being produced by the reaction, indicating an additional source of water on the cathode, namely excess water accumulation.

2.4 Experimental Results and Discussion

This section presents the experimental results based on the above methods. The polarization curve data and qualitative AWR results are shown first to benchmark the

system and corroborate the inherently different water management capabilities of the three GDLs. Specific values determined from the ex-situ pressure drop calibration tests are provided. Finally, results from the in-situ experiments are presented, including the different voltage responses, the calculated net cell water fluxes, the cathode pressure drop signals, and finally the total water removed as compared to the voltage gain.

2.4.1 Polarization Curves and Qualitative AWR Results

Three different MEA setups were investigated to compare operating characteristics. Polarization curve data was collected for MEAs, with a 25 BC, 25 BA, and 25 AA GDL on the cathode side, and the results found in Figure 9A. For all three MEAs investigated the anode featured a 25 BC GDL to ensure no water accumulation on the anode.

As expected, the MEA with a cathode 25 BC GDL performed the best, due to its hydrophobic treatment (5% PTFE) and MPL, which both assist with water management in terms of liquid and vapor [32] transport. The 25 AA GDL performed the worst, due to the lack of MPL and any sort of hydrophobic treatment (0% PTFE).

The basic AWR procedure was applied to these three same MEA setups at standard operating conditions of 75 °C and 206.9 kPaG of backpressure. In addition, the 25 AA MEA setup was tested at 85 °C to investigate the effect that temperature had on the test. Results of these four tests can be seen in Figure 9B. For all tests, the current density was fixed at 1000 mA cm^{-2}. The increase of the cell voltage in the 25 BA and 25 AA setups demonstrate that the reduction in voltage seen in the polarization curve was due to poor water management on the cathode. The drop in voltage above the anode

stoichiometry of five for the 85 °C, 25 AA case indicates that the membrane has started to dehydrate, thus resulting in an increase in ionic resistance. These results indicate that the GDLs perform as expected based on literature [35], making them ideal template

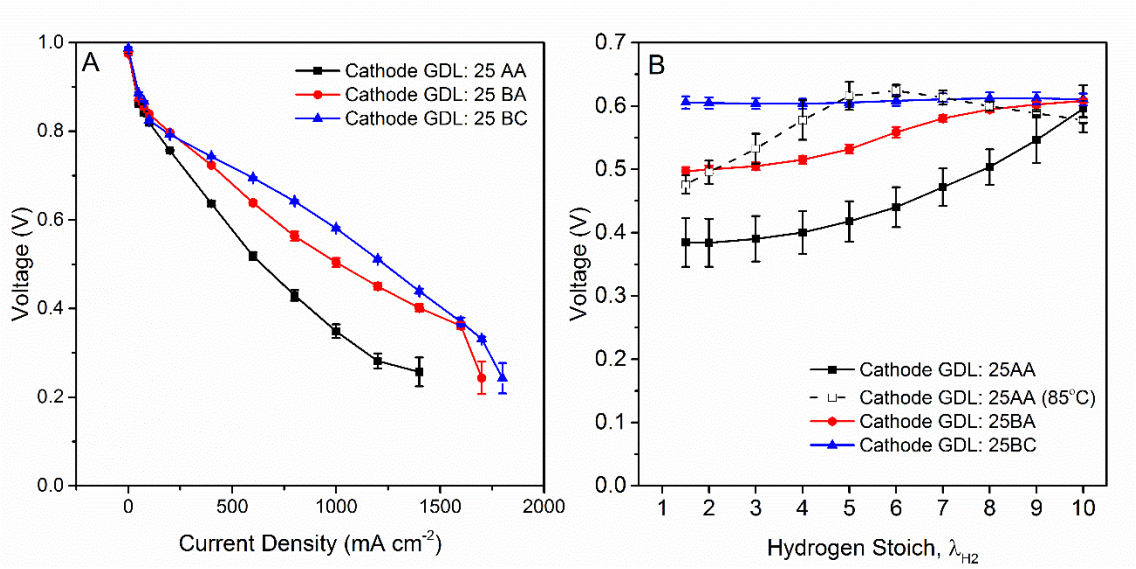

GDLs to use in this quantitative study.

Figure 9. (A) Polarization curve data for different membrane electrode assembly (MEA) configurations varying the cathode GDL at 75 °C for all setups, and (B) Comparison of AWR results for different MEA configurations varying the cathode GDL.

2.4.2 *Ex-Situ* System Parameters in Pressure Drop Analysis

The ex-situ anode pressure drop data was collected with the anode stream at set RH values of 0%, 25%, 50%, 75%, and 100%, at the operating condition used for the in-situ testing. For both of these operating cases, 75 °C and 85 °C, an overall K_L value was then calculated. The K_L value calculated for 75 °C was 7.7, with a 7% average error value, and for 85 °C was 8.3, with a 7.2% average error value. Percent error was calculated between experimental pressure drop values measured and the predicted values determined from Equation (2.1). Figure 10 demonstrates the strong fit found between the predicted and ex-situ experimental pressure drop values using the determined K_L value. It

should be noted that most of the divergence between experimental and predicted pressure drops were found to occur at lower flow rates, likely due to the fact that the RH term is located within the exponential in Equation (2.1), causing it to be more dominant in the higher flow regimes. However, at these low flow rates the maximum potential amount of water that can be removed by the anode is one order of magnitude lower than the amount being produced by the reaction, thus this potential error does not affect the analysis.

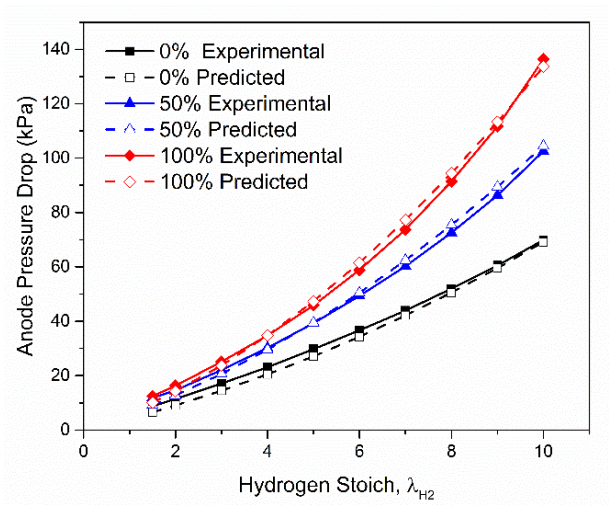

Figure 10. Comparison of experimentally measured anode pressure drop values and values predicted from Equation (1) at corresponding stoichiometric values for the fuel cell operating at 75 °C and P_{inlet} = 206.9 kPaG.

2.4.3 Quantification of Water Removed

Using the experimentally determined K_L values, average anode RH values were calculated for each stoichiometric set point step within the AWR tests. By first converting the RH data into a mixing ratio, Equation (2.14), and then combining it with the outlet mass flow rate, Equation (2.15), an average water removal rate was then calculated for each set point. An example of the results of these calculations for the three trials performed on the 25 AA GDL is presented in Table 3.

Table 3. Comparison of Voltage, Anode Relative Humidity, and Net Cell Water Flux for three individual trials with a 25 AA cathode GDL at 75 °C and P_{inlet} = 206.9 kPaG.

Stoich	Trial 1			Trial 2			Trial 3		
	Voltage	Anode RH	Net Cell Water Flux (g min^{-1})	Voltage	Anode RH	Net Cell Water Flux (g min^{-1})	Voltage	Anode RH	Net Cell Water Flux (g min^{-1})
1.5	0.37	100.00%	0.25	0.31	100.00%	0.25	0.36	100.00%	0.25
2	0.37	100.00%	0.23	0.30	100.00%	0.23	0.37	100.00%	0.23
3	0.38	100.00%	0.19	0.30	100.00%	0.19	0.38	100.00%	0.19
4	0.40	100.00%	0.15	0.33	100.00%	0.15	0.39	100.00%	0.15
5	0.44	100.00%	0.10	0.39	100.00%	0.10	0.44	100.00%	0.10
6	0.48	100.00%	0.05	0.44	100.00%	0.05	0.49	100.00%	0.05
7	0.52	100.00%	−0.01	0.50	100.00%	0.00	0.52	100.00%	0.00
8	0.59	100.00%	−0.07	0.57	98.90%	−0.07	0.58	95.86%	−0.06
9	0.63	95.70%	−0.13	0.62	89.19%	−0.10	0.62	83.01%	−0.07
10	0.62	91.82%	−0.20	0.62	85.59%	−0.16	0.62	75.72%	−0.10

A negative net cell water flux indicates that the anode is removing more water than the amount generated by the reaction, as the contribution to the cathode gas flow is minimal in order to maintain the fully humidified condition. Since the amount of water being produced by the reaction is known, the cases with a negative net cell flux indicate the removal of additional excess liquid water that has accumulated on the cathode side. As these calculations depend on the anode pressure drop measurement, a calculation of the range of the net cell water flux for a single trial was performed using the potential range of the anode pressure drop, based on the standard deviation found for each stoichiometric point. The result of this calculation shows that the average possible range for the net cell water flux was ± 0.006 g min^{-1}, with a maximum range of ± 0.02 g min^{-1} found at the highest stoichiometric flow rate. For the following figures, the error presented is the standard deviation between the three trials performed at each investigated operating condition, which was found to more accurately convey the potential error of this experimental system.

These calculations were repeated for the other nine trials, performed on the other three MEA and operating condition setups. A summary of the voltage changes as they relate to the changing net cell water flux for the four setups is displayed in Figure 11.

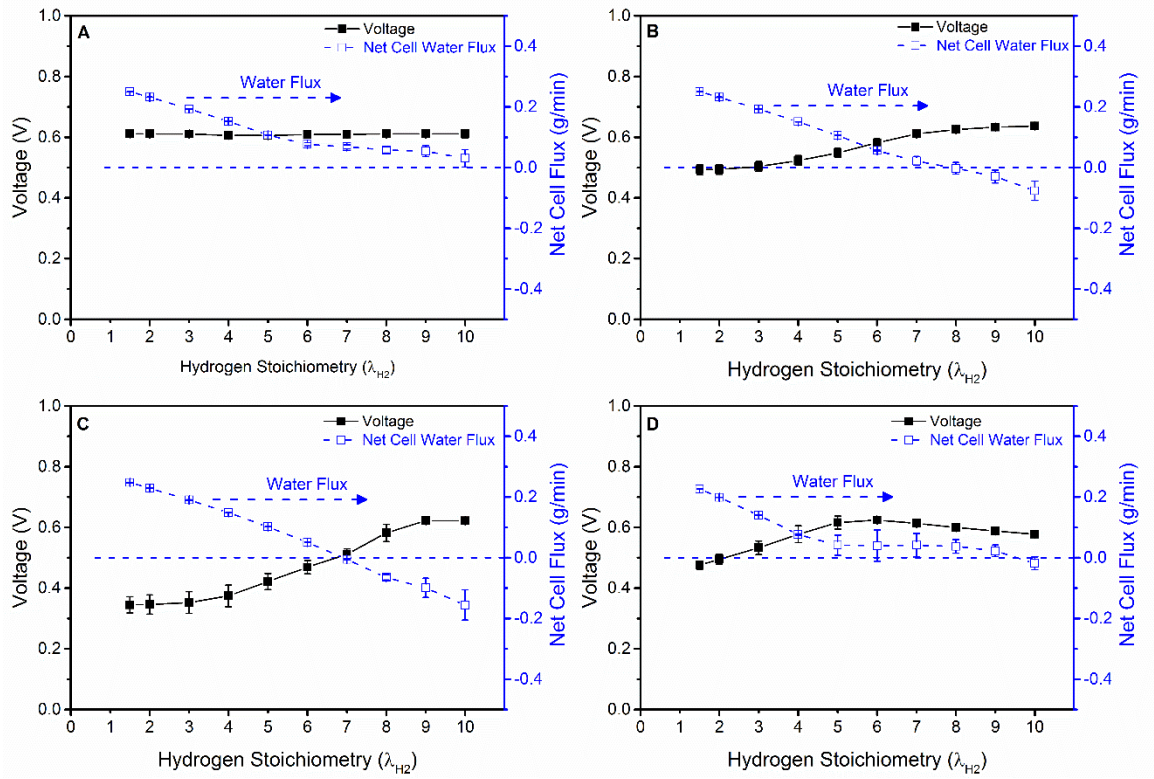

Figure 11. Comparison of voltage and net cell water flux for the operating conditions of (A) 75°C; cathode GDL 25 BC (B) 75°C; cathode GDL 25 BA (C) 75°C; cathode GDL 25 AA and (D) 85°C; cathode GDL 25 AA

The effect of the MPL is clearly noted as no voltage change occurs for the 25 BC GDL. It has been reported that one of the potential functionalities of the MPL is to help control for the accumulation of water between the GDL and the CCM [28,32]. It therefore makes sense that the reduction of water vapor on the cathode side did not have a noticeable effect on the voltage response, since the MPL was already helping to control the concentration of water vapor near the CCM. The net cell water flux is never negative, indicating that no excess water had accumulated in this case with an MPL. In the cases without an MPL, the major change in voltage occurs before the anode is able to remove more water vapor than what is being produced by the reaction. This result indicates the

mass transport limitation that causes the initial reduction in voltage is improved via more efficient transport of vapor away from the cathode catalyst layer, as well as the removal of the accumulated liquid water. Additionally, in the case of the 25 AA GDL, a large, negative net cell water flux is measured above an anode stoichiometry of seven. The negative net cell water flux indicates accumulated liquid water on the cathode in addition to vapor transport. The larger water removal displayed by the 25 AA GDL when compared to the 25 BA GDL agrees with the results from Figure 3, as well as previously published studies [35], since the 25 AA GDL does not have any PTFE treatment.

These results are also consistent with the cathode pressure drop results. In Figure 12 the average cathode pressure drops from each operating point are plotted versus the stoichiometric set points.

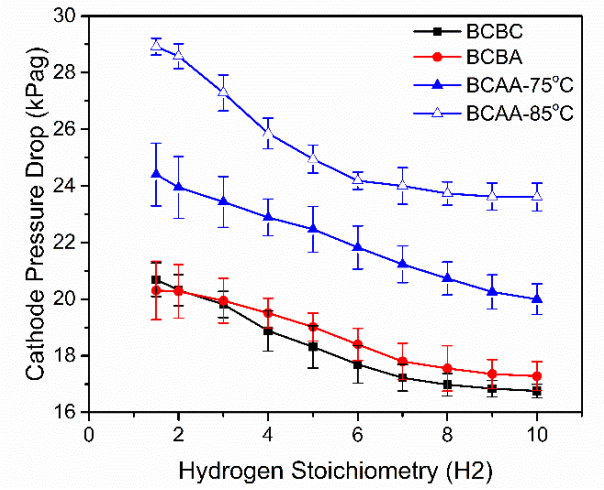

Figure 12. Average cathode pressure drop for each MEA configuration. Open symbols represent the tests performed at 85°C.

In all cases, there is a reduction in pressure drop consistent with water being removed from the cathode. In the case of the 25 BC GDL, where mass transport effects

are already minimized, the reduction in pressure drop is consistent with a lower total mass flow rate in the cathode flow field channels, due to water produced by the reaction moving to the anode instead. In the case of the 25 AA GDL, the pressure drop reduces throughout the test but remains higher than the 25 BC and 25 BA GDLs. The final voltages are similar in all cases, indicating that any mass transport limitations have been removed in the 25 AA case, but the higher pressure drop indicates residual channel water on the surface of this hydrophilic GDL.

This analysis is quantitatively supported by the average net voltage change, and total water removed by the anode stream, as reported in Figure 13. First, the case which demonstrates both a negligible voltage change and also has the lowest water removed on the anode is the setup with the 25 BC GDL, as expected. In this case, there was still a reduction in the cathode pressure drop, seen in Figure 12, however this reduction in cathode water vapor did not have any noticeable effect on the voltage signal.

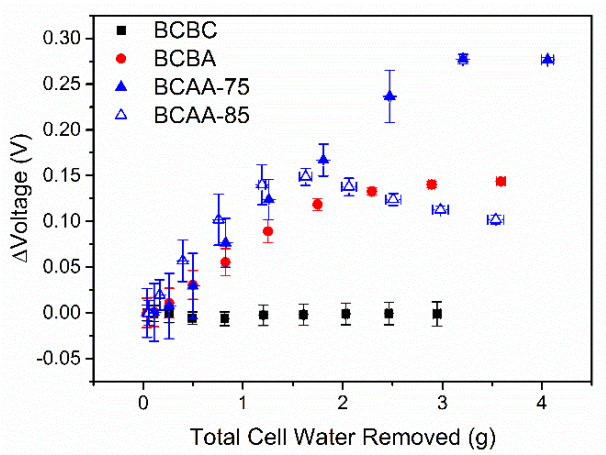

Figure 13. A plot of the increase in voltage versus the total water removed by the anode stream.

The most drastic change in voltage is observed with the 25 AA GDL at 75°C, from an initial voltage of 0.34 V, to a peak voltage of 0.62 V. This case is also observed to remove the most amount of water throughout the test. Although this setup has a lower evaporative potential than the 85°C case, the lower operating temperature promotes the largest amount of initial excess cathode water. This larger amount of available water allows for the largest net cell water flux out of the cell, seen in Figure 11C. The voltage response in Figure 11C shows a consistent increase in signal, showing that all the water being removed by the anode is negatively affecting the power of the fuel cell. Additionally, the cathode pressure drop in Figure 12 is seen to consistently decay, indicating a steady removal of the reaction product water vapor through the anode, from the increasing evaporative gradient.

The 85°C 25 AA and 75°C 25 BA cases display very similar results. From Figure 5B,D, it is seen that they start at a similar initial voltage, indicating a similar performance reduction related to mass transport, despite differing PTFE content and temperatures. The main difference between the two tests is demonstrated by their respective voltage responses, seen in Figure 11B,D. The 85°C 25 AA case demonstrate a sharp initial increase in voltage, from 0.47 V to 0.62 V over 5 stoichiometric set points, followed by a gradual decline in voltage, indicating the dehydration of the membrane. Interestingly, this sharp voltage increase aligns with the sharp decrease in the cathode pressure drop, as seen in Figure 12. This cathode pressure drop reduction is a function of the reduction of water on the cathode side, and the drastic increase in voltage indicates the removal of water that is negatively impacting the voltage. The 75°C, 25 BA case displays a more

gradual increase in voltage, not reaching peak voltage until the final stoichiometric set point. This gradual increase points to the important differences in evaporative potential between the 75°C and 85°C operating conditions. From the voltage signal in Figure 11D, it is seen that in the 85°C case the voltage change occurs earlier in the test, qualitatively agreeing with the higher evaporative potential that would be present at this higher temperature.

A similar analysis could be conducted by those studying operating conditions or engineered gas diffusion layers. By analyzing the amount of water removed via the anode, one has quantified the amount of water in the cathode and its impact on performance. Thus, a quantitative measure of the effect of mass transport limitations is determined. As detailed before, this analysis could also be extended to alternative flow field configurations, after the modification of the applicable equations. Future work is needed to verify that the assumptions used in this study are valid for interdigitated or multi-channel flow fields, but the analysis could be used to study the initial water saturation promoted by these different configurations or to determine their effect on the water flux through the cell.

2.5 Conclusions

A new diagnostic tool is presented to experimentally determine water flux rates into an initially dry anode stream, thus quantifying the amount of water being removed from the cathode. When the anode flow rate is sufficiently raised, this flux can overcome the water production rate of the reaction, identifying additional excess cathode water.

These results were obtained via an RH measurement, based on the pressure drop of the gas streams, where the anode pressure drop is calibrated to the anode RH. In this procedure, the flow rate of a dry anode stream is increased to cause an evaporative potential from the cathode to the anode. By measuring the anode pressure drops, the amount of water being removed by the anode can be calculated. The combination of this removal rate along with the water production rate from the reaction, allows for the calculation of an overall net cell water flux. The analysis of this value, along with its relation to the changing voltage of the fuel cell, allows for an investigation of water movement throughout the cell and a quantitative determination of excess water within the cell. This study investigated four different operating setups, featuring three different cathode GDLs, as well as two operating temperatures (75°C and 85°C), demonstrating the wide applicability of the approach. Net voltage gains, as well as the total water removed for each case were presented. In GDLs without an MPL, large voltage gains are noted as more cathode water is removed, which is indicative of a reduction of mass transport limitations in the cell. A main strength of the protocol is the ability to quantitatively calculate the RH of the anode stream without the need of expensive equipment. The technique hinges on the manipulation of operating conditions and knowledge of basic details of the specific fuel cell architecture, and can thus be applied to a wide assortment of fuel cell setups, providing an accessible and easy-to-implement protocol for a variety of PEMFC applications.

Acknowledgments

This material is based upon work supported by the National Science Foundation under Grant Number 1444198. Any opinions, findings, and conclusions or recommendations expressed in this material are those of the authors and do not necessarily reflect the views of the National Science Foundation. The authors further thank Montana State University for funds related to these efforts. The authors also thank Erick Johnson from Montana State University and the continued technical support from Greenlight Innovation and Tandem Technologies Ltd.

Appendix 2.A. Constants used in Equations

Table A1. Viscosity values and coefficients for Equation (2.7) (T_0 = 25 °C) [39].

Fluid	μ_0	C
Air	1.81×10^{-5}	120
Hydrogen	0.92×10^{-5}	72
Water Vapor	1.02×10^{-5}	660

Table A2. Coefficients used in saturated vapor pressure Equation (2.11) [39].

Coefficients for Vapor Pressure Equation	
a =	−5800.2206
b =	1.3914493
c =	−0.0486402
d =	$0.41764768 \times 10^{-4}$
e =	$-0.14452093 \times 10^{-7}$
f =	6.5459673

References

1. United States Department of Energy. Full Cell Technologies Office Multi-Year Research, Development, and Demonstration Plan; United States Department of Energy: Washington, DC, USA, 2012; pp. 1–58.

2. Wang, Y.; Chen, K.S.; Mishler, J.; Cho, S.C.; Adroher, X.C. A review of polymer electrolyte membrane fuel cells: Technology, applications, and needs on fundamental research. Appl. Energy 2011, 88, 981–1007.

3. Yousfi-Steiner, N.; Moçotéguy, P.; Candusso, D.; Hissel, D.; Hernandez, A.; Aslanides, A. A review on pem voltage degradation associated with water management: Impacts, influent factors and characterization. J. Power Sources 2008, 183, 260–274.

4. Ous, T.; Arcoumanis, C. Degradation aspects of water formation and transport in proton exchange membrane fuel cell: A review. J. Power Sources 2013, 240, 558–582.

5. Pei, P.; Li, Y.; Xu, H.; Wu, Z. A review on water fault diagnosis of pemfc associated with the pressure drop. Appl. Energy 2016, 173, 366–385.

6. Hussaini, I.S.; Wang, C.Y. Dynamic water management of polymer electrolyte membrane fuel cells using intermittent RH control. J. Power Sources 2010, 195, 3822–3829.

7. Song, M.; Pei, P.; Zha, H.; Xu, H. Water management of proton exchange membrane fuel cell based on control of hydrogen pressure drop. J. Power Sources 2014, 267, 655–663.

8. Damour, C.; Benne, M.; Grondin-Perez, B.; Chabriat, J.-P.; Pollet, B.G. A novel non-linear model-based control strategy to improve pemfc water management—The flatness-based approach. Int. J. Hydrogen Energy 2015, 40, 2371–2376.

9. Pahon, E.; Yousfi Steiner, N.; Jemei, S.; Hissel, D.; Moçoteguy, P. A signal-based method for fast pemfc diagnosis. Appl. Energy 2016, 165, 748–758.

10. Alink, R.; Haußmann, J.; Markötter, H.; Schwager, M.; Manke, I.; Gerteisen, D. The influence of porous transport layer modifications on the water management in polymer electrolyte membrane fuel cells. J. Power Sources 2013, 233, 358–368.

11. Chen, H.-H.; Chang, M.-H. Effect of cathode microporous layer composition on proton exchange membrane fuel cell performance under different air inlet relative humidity. J. Power Sources 2013, 232, 306–309.

12. Li, A.; Chan, S.H. Understanding the role of cathode structure and property on water management and electrochemical performance of a pem fuel cell. Int. J. Hydrogen Energy 2013, 38, 11988–11995.

13. Lemoine-Nava, R.; Hanke-Rauschenbach, R.; Mangold, M.; Sundmacher, K. The gas diffusion layer in polymer electrolyte membrane fuel cells: A process model of the two-phase flow. Int. J. Hydrogen Energy 2011, 36, 1637–1653.

14. Qin, C.; Rensink, D.; Fell, S.; Majid Hassanizadeh, S. Two-phase flow modeling for the cathode side of a polymer electrolyte fuel cell. J. Power Sources 2012, 197, 136–144.

15. Fazeli, M.; Hinebaugh, J.; Fishman, Z.; Tötzke, C.; Lehnert, W.; Manke, I.; Bazylak, A. Pore network modeling to explore the effects of compression on multiphase

transport in polymer electrolyte membrane fuel cell gas diffusion layers. J. Power Sources 2016, 335, 162–171.

16. Kalidindi, A.R.; Taspinar, R.; Litster, S.; Kumbur, E.C. A two-phase model for studying the role of microporous layer and catalyst layer interface on polymer electrolyte fuel cell performance. Int. J. Hydrogen Energy 2013, 38, 9297–9309.

17. Meng, H.; Han, B.; Ruan, B. Numerical modeling of liquid water transport inside and across membrane in pem fuel cells. Asia-Pac. J. Chem. Eng. 2013, 8, 104–114.

18. Qin, Y.; Du, Q.; Yin, Y.; Jiao, K.; Li, X. Numerical investigation of water dynamics in a novel proton exchange membrane fuel cell flow channel. J. Power Sources 2013, 222, 150–160.

19. Wang, Y.; Chen, K.S. Advanced control of liquid water region in diffusion media of polymer electrolyte fuel cells through a dimensionless number. J. Power Sources 2016, 315, 224–235.

20. Grötsch, M.; Mangold, M. A two-phase pemfc model for process control purposes. Chem. Eng. Sci. 2008, 63, 434–447.

21. Berning, T.; Odgaard, M.; Kær, S.K. A study of multi-phase flow through the cathode side of an interdigitated flow field using a multi-fluid model. J. Power Sources 2010, 195, 4842–4852.

22. Ding, Y.; Bi, X.; Wilkinson, D.P. 3D simulations of the impact of two-phase flow on pem fuel cell performance. Chem. Eng. Sci. 2013, 100, 445–455.

23. Yau, T.C.; Cimenti, M.; Bi, X.T.; Stumper, J. Water transport and schröder's paradox in fuel cell membrane electrode assemblies. J. Power Sources 2013, 224, 285–289.

24. Morgan, J.M.; Datta, R. Understanding the gas diffusion layer in proton exchange membrane fuel cells. I. How its structural characteristics affect diffusion and performance. J. Power Sources 2014, 251, 269–278.

25. Chevalier, S.; Lee, J.; Ge, N.; Yip, R.; Antonacci, P.; Tabuchi, Y.; Kotaka, T.; Bazylak, A. In operando measurements of liquid water saturation distributions and effective diffusivities of polymer electrolyte membrane fuel cell gas diffusion layers. Electrochim. Acta 2016, 210, 792–803.

26. Bazylak, A. Liquid water visualization in pem fuel cells: A review. Int. J. Hydrogen Energy 2009, 34, 3845–3857.

27. Krüger, P.; Markötter, H.; Haußmann, J.; Klages, M.; Arlt, T.; Banhart, J.; Hartnig, C.; Manke, I.; Scholta, J. Synchrotron X-ray tomography for investigations of water distribution in polymer electrolyte membrane fuel cells. J. Power Sources 2011, 196, 5250–5255.

28. Deevanhxay, P.; Sasabe, T.; Tsushima, S.; Hirai, S. Effect of liquid water distribution in gas diffusion media with and without microporous layer on pem fuel cell performance. Electrochem. Commun. 2013, 34, 239–241.

29. Banerjee, R.; Ge, N.; Lee, J.; George, M.G.; Chevalier, S.; Liu, H.; Shrestha, P.; Muirhead, D.; Bazylak, A. Transient liquid water distributions in polymer electrolyte

membrane fuel cell gas diffusion layers observed through in-operando synchrotron X-ray radiography. J. Electrochem. Soc. 2017, 164, F154–F162.

30. Owejan, J.P.; Trabold, T.A.; Jacobson, D.L.; Baker, D.R.; Hussey, D.S.; Arif, M. In situ investigation of water transport in an operating pem fuel cell using neutron radiography: Part 2—Transient water accumulation in an interdigitated cathode flow field. Int. J. Heat Mass Transf. 2006, 49, 4721–4731.

31. Hussaini, I.S.; Wang, C.Y. Visualization and quantification of cathode channel flooding in pem fuel cells. J. Power Sources 2009, 187, 444–451.

32. Owejan, J.P.; Owejan, J.E.; Gu, W.; Trabold, T.A.; Tighe, T.W.; Mathias, M.F. Water transport mechanisms in pemfc gas diffusion layers. J. Electrochem. Soc. 2010, 157, B1456–B1464.

33. Anderson, R.; Blanco, M.; Bi, X.; Wilkinson, D.P. Anode water removal and cathode gas diffusion layer flooding in a proton exchange membrane fuel cell. Int. J. Hydrogen Energy 2012, 37, 16093–16103.

34. Battrell, L.; Trunkle, A.; Eggleton, E.; Zhang, L.; Anderson, R. Investigation of water transport within a proton exchange membrane fuel cell by diffusion layer saturation analysis. In Proceedings of the 2016 14th International Conference on Fuel Cell Science, Engineering and Technology, Charlotte, NC, USA, 26–30 June 2016; p. V001T005A002.

35. Cindrella, L.; Kannan, A.M.; Lin, J.F.; Saminathan, K.; Ho, Y.; Lin, C.W.; Wertz, J. Gas diffusion layer for proton exchange membrane fuel cells—A review. J. Power Sources 2009, 194, 146–160.

36. Li, H.; Tang, Y.; Wang, Z.; Shi, Z.; Wu, S.; Song, D.; Zhang, J.; Fatih, K.; Zhang, J.; Wang, H.; et al. A review of water flooding issues in the proton exchange membrane fuel cell. J. Power Sources 2008, 178, 103–117.

37. Kim, M.; Jung, N.; Eom, K.; Yoo, S.J.; Kim, J.Y.; Jang, J.H.; Kim, H.-J.; Hong, B.K.; Cho, E. Effects of anode flooding on the performance degradation of polymer electrolyte membrane fuel cells. J. Power Sources 2014, 266, 332–340.

38. Voss, H.H.; Wilkinson, D.P.; Pickup, P.G.; Johnson, M.C.; Basura, V. Anode water removal: A water management and diagnostic technique for solid polymer fuel cells. Electrochim. Acta 1995, 40, 321–328.

39. Barbir, F. Pem Fuel Cells: Theory and Practice; Academic Press: Cambridge, MA, USA, 2012.

CHAPTER THREE

TRANSIENT, SPATIALLY RESOLVED DESATURATION OF GAS DIFFUSION LAYERS MEASURED VIA SYNCHROTRON VISUALIZATION

Contribution of Authors and Co-Authors

Manuscript in Chapter 3

Author: Logan Battrell

Contributions: Conceived and designed experiments, performed experiments, analyzed data, wrote the manuscript

Co-Author: Ning Zhu

Contributions: Assisted in synchrotron and data analysis, edited earlier manuscripts

Co-Author: Lifeng Zhang

Contributions: Conceived and designed experiments, edited earlier manuscripts

Co-Author: Ryan Anderson

Contributions: Conceived and designed experiments; analyzed data; provided materials and analysis tools; edited manuscripts

Manuscript Information

Logan Battrell, Ning Zhu, Lifeng Zhang and Ryan Anderson

International Journal of Hydrogen Energy

Status of Manuscript:
____ Prepared for submission to a peer-reviewed journal
____ Officially submitted to a peer-reviewed journal
____ Accepted by a peer-reviewed journal
_X_ Published in a peer-reviewed journal

Elsevier
Vol 43, Issue 24, Pages 11234-11243, June 2018
https://doi.org/10.1016/j.ijhydene.2018.05.017

TRANSIENT, SPATIALLY RESOLVED DESATURATION OF GAS DIFFUSION LAYERS MEASURED VIA SYNCHROTRON VISUALIZATION

Abstract

The transient 3-D visualization of the desaturation process of flooded gas diffusion layers (GDLs) is presented for the first time. Desaturation rates and pathways are reported for two commercial GDL samples, one with a PTFE treatment and the other without. On-the-fly synchrotron X-ray CT is performed while the GDL sample is subjected to a humidified or dry air flow stream to visualize the transient desaturation. The two humidification conditions assist in separating the convective and evaporative components of the desaturation process, showing a slight contribution from the convective effect, while the majority of the desaturation is due to evaporative removal. The convective removal is found to be insufficient to fully desaturate either GDL, with water remaining trapped underneath the channel rib with the more hydrophobic GDL and within the pore space in the more hydrophilic GDL. Stop-and-shoot synchrotron X-ray computed tomography (CT) is then used in conjunction with program-assisted segmentation to determine initial saturation water volumes. These are then combined with the desaturation times found from the on-the-fly experiments to determine desaturation rates for both GDLs. The desaturation rate using dry air flow for the more hydrophobic GDL is found to be nearly four times faster than that of the more

hydrophilic GDL. Results demonstrate that an evaporative contribution is necessary for either GDL sample to reach full desaturation.

3.1 Introduction

Polymer Electrolyte Membrane (PEM) fuel cells are a scalable energy conversion technology with the potential for zero local emissions, high power density, and rapid start-up, making them an attractive option for both mobile and stationary applications [1]. One of the main challenges to successful long-term, efficient fuel cell operation is water management, where water produced by the reaction and brought into the cell via a humidified air stream must be controlled [2]. Insufficient water management can lead to poor performance or total cell failure and reduce long term durability and efficiency [3, 4]. Proper water management includes maintaining enough water to hydrate the electrolyte membrane for proton conductivity while not allowing for excess water accumulation, which blocks effective gas transport to the catalyst layer [5, 6]. Thus, water management occurs over a range of length and time scales, from the catalyst layer and membrane to the flow field. Central to this challenge is the transient nature of fuel cell operation, previously reviewed by Banerjee and Kandlikar [7]. Any changes in power production result in changing water production rates, further complicating the balance of the overall system.

A key component to the overall water management of the fuel cell is maintaining appropriate water transport within the porous Gas Diffusion Layer (GDL), which is utilized to connect the flow field channels to the active reaction sites. At the cathode, it

must allow for efficient oxygen transport to the catalyst layer while also facilitating the removal of water produced by the reaction. Multiple studies have been performed to better understand the transport phenomena occurring within this thin porous layer. These studies have included investigations of various properties related to water transport, as well as investigating structural modifications of the entire membrane electrode assembly (MEA). Such research includes the exploration of introducing perforations to specific locations of a GDL [8], modifying microporous layer (MPL) composition based on the gas flow conditions [9], and changing the surface properties of the different layers on the cathode side [10]. Investigations of transport properties of GDLs have been performed in both an in-situ and ex-situ manner. Owejan et al. [11] measured vapor and liquid transport rates through different GDLs ex-situ, and then investigated how these properties affected active cell performance. From this work, they proposed that one of the main functions of the MPL was to help prevent the formation of a water film on the surface of the catalyst layer (CL). Morgan et al. [12] measured the vapor diffusivity and permeability of various GDLs using a specially-designed diffusivity cell and identified how different GDL design parameters can enhance performance in high or low current density operation. Yau et al. [13] measured overall MEA water crossover rates between the anode and cathode without a current load through infrared sensors and outlet gas processing. Signal analysis has also been investigated as a way to infer water movement or accumulation within a fuel cell, to enable a responsive control scheme to better avoid suboptimal performance. Hussaini et al. [14] proposed a dynamic external intermittent humidification scheme for multiple flow fields based on a feedback loop with the cell

voltage. Song et al. [15] proposed a hydrogen purge protocol based on the analysis of the hydrogen pressure drop to indicate cathode flooding. Damour et al. [16] designed a model to control air flow to regulate the overall water content of the membrane and optimize performance. Battrell et al. [17] analyzed the anode pressure drop of an initially dry anode stream to calculate the amount of water being removed from a flooded fuel cell. In each of these methods, a macroscopic parameter, such as the voltage or a pressure drop, is measured to infer a piece of the overall water behavior. These macro level studies have provided important information about the system, but understanding water management at the pore scale is necessary to inform the intelligent design of fuel cell systems.

Visualization has been a key tool to provide additional understanding of the various water management characteristics within the fuel cell at the micro level, and a review of the strengths and weaknesses of various visualization methods was provided by Bazylak [18]. One of the challenges related to visualization is that the natural architecture of a PEM fuel cell dictates that either specialized instrumentation or major modification to the overall fuel cell is required. Hussaini et al. [19] proposed a channel flow regime map of various two-phase flow patterns based on direct visualization experiments performed using an optically transparent fuel cell. Deevanhxay et al. [20] used soft X-ray tomography to visualize and confirm the increased flooding that occurs between the GDL and catalyst layer (CL) if an MPL is not applied to the GDL, which had previously been proposed by Owejan [11]. Iranzo et al. [21] utilized neutron beam imaging to visualize the transient water build-up during start-up and identified that water initially builds up at

the cathode exit, but that the location was dependent on the specific flow field design. Another transient investigation by Banerjee et al. [22] looked at water distributions in the GDL with increasing current density and found that the saturation increased to a certain threshold and would then stay steady as the current density was further raised. Lamibrac et al. [23] investigated water transport through the GDL by varying the capillary pressure to understand the pathways that the water takes through the GDL and found that consecutive injections followed similar pathways, but that small water volumes would accumulate in unconnected pores. Such visualization experiments have been key in confirming previously inferred conclusions.

Another visualization technique used to investigate PEM fuel cells is synchrotron radiography, due to the available phase contrast along with high temporal and spatial resolution. Synchrotron radiography was used by Kruger et al. [24] to demonstrate the increase in cathode GDL saturation that occurs when a fuel cell is operated at a high current density. Lee et al. [25] used synchrotron radiography to visualize and quantify water within the GDL to investigate the effects of MPL thickness on GDL water content. Chevalier et al. [26] used synchrotron radiography to characterize liquid water transport capabilities of various electrospun GDLs. All of the above studies demonstrate the important and conflicting roles that different layer properties and fuel cell design can have on fuel cell operation. For example, in the study of novel electrospun GDLs [26], it was found that the GDLs could reduce water accumulation underneath the channel ribs, but were also facilitating significant membrane dry-out. In many of the discussed studies, the focus was on the behavior of water ingress into the GDL or steady-state conditions. A

key area which has been overlooked is an exploration of the mechanisms by which water is removed. For instance, water management strategies that utilize a dry gas stream [14, 15, 17] rely on evaporation to provide GDL desaturation. However, this dynamic process has not been resolved in both a spatial and temporal manner in previous publications. In addition to expanding the understanding of how GDL desaturation occurs, results could be useful to inform models, which are often used to investigate the transient behaviors in PEMFC operation [27-29].

The focus of this work was to visualize the 3-D transient desaturation of different GDLs by convection and evaporation from air flowing in a serpentine gas channel. Emphasis was placed on two different GDLs and two different humidification conditions. The commercially produced Sigracet SGL 25 AA (0% PTFE) and 25 BA (5% PTFE) GDLs were utilized to contrast the initial saturation present; the 25 AA further allows for a higher initial saturation, providing more temporally resolved images of the desaturation process. The comparison of dry and fully humidified inlet gas conditions allow for the contributions of evaporation and convection to be analyzed individually. Desaturation images and rates for both GDL samples are presented and discussed.

3.2 Methods

Many decisions were made to optimize the design of the flow cell and the setup of the beam for two key parameters: to maximize the phase contrast between the water, GDL, and the flow cell; and to maximize the framerate at which the images could be acquired in order to minimize the total time required to perform a full X-ray computed

tomography (CT) scan. Sample preparation and setups used for the experiments are detailed, as well as the image processing protocol used to analyze the collected data.

3.2.1 Sample Design and Description

The chosen material used for the flow cell was acrylic due to its low absorption of X-rays compared to graphite, which is the standard material for PEMFC flow fields. Initial experiments showed that the phase contrast between the graphite, water, and GDL was insufficient due to the resulting low total X-ray flux. Since the focus of the experiments was on the desaturation of the GDL itself and not on interactions between the water and the flow field, the transition to acrylic was deemed acceptable in order to optimize the aforementioned parameters of interest. Figure 14 shows the flow cell pieces and schematics of the relevant geometries. The top and bottom pieces screw together, allowing a GDL sample to be placed between the two. The bottom portion featured a plenum that could be filled with water and used in part to create the initial max saturation condition for the quantification tests. The rib in the middle provided support for the GDL sample to ensure that the GDL would not sag down into the plenum. The top flow field features a typical serpentine pattern with 4 bends. The channel geometry was modelled after typical PEMFC geometry, with a cross section of 1mm x 1mm. The channel was designed to maximize the total channel length within the beam dimensions, allowing for a total channel length of 27.7 mm. The final design characteristic was a rubber gasket around the outside to ensure that water would not bypass the designed flow channels and leak from the sides of the cell. The diameter within the gasket was 12mm with an active area of 113 mm^2.

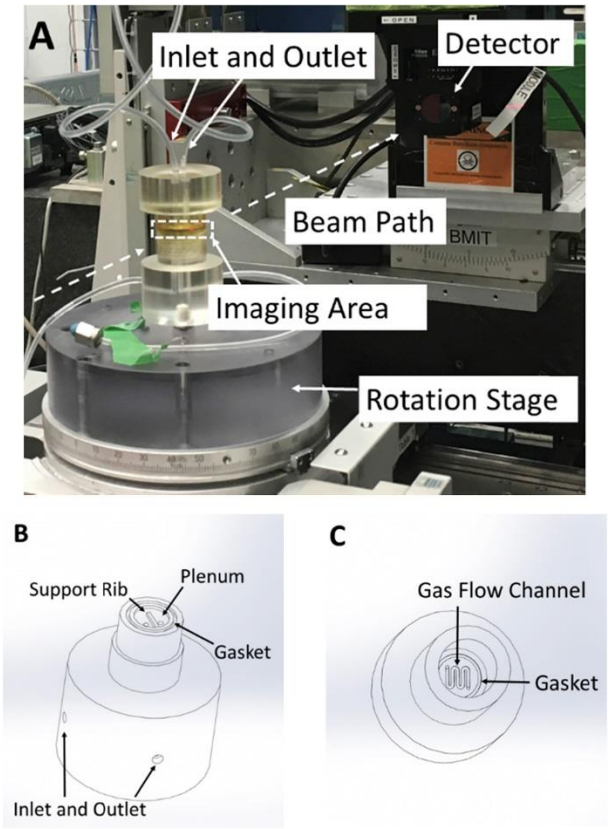

Figure 14. A) Assembled flow cell in beam setup with beam path and imaging area highlighted, B) Schematic of plenum and support rib located below the GDL sample, C) Schematic of flow channels located on top of the GDL sample

3.2.2 Desaturation Protocol and Experimental Conditions

In order to set the initial condition, the GDL samples were placed in a water bath and agitated for 1 minute, and then placed within the flow cell. To initiate the desaturation process, the air flow rate was set at 50 ml/min using an Omega FL-380-2ST rotameter (± 2 ml/min), which corresponds with a flowrate required to operate a similar sized active cell at 1000 mA/cm^2 at a stoichiometric point of 2. The GDLs and inlet gas conditions are highlighted in Table 4.

Table 4. GDLs with PTFE loadings, along with details of the T, P, and RH for all tests

GDLS / Conditions	Dry Air Inlet	Humidified Air Inlet
SGL 25 AA (no PTFE)	P = 1 bar, T = 22ºC, RH = 0%	P = 1 bar, T = 22°C, RH = 100%
SGL 25 BA (5% PTFE)	P = 1 bar, T = 22ºC, RH = 0%	P = 1 bar, T = 22°C, RH = 100%

Although the 25 AA GDL is not commonly used for fuel cell operation, it was selected to better investigate the desaturation because it allowed for a much higher initial saturation. This guaranteed that the transient nature of the full desaturation process could be captured by imaging at discrete times between the initially saturated and final dry condition. For the dry flow tests, the air flow was at room temperature and 0% relative humidity. For the humidified tests, the air was bubbled through heated water to 28°C and 85% relative humidity, for a wet bulb temperature of 26°C. The air was then measured at the inlet and outlet of the flow cell at room temperature 22°C. The relative humidity could not be measured at these points due to the size of the tubing, but was assumed to remain saturated at 100% relative humidity based on the temperature and pressure. This humidification setup ensured that any water removal during this case would be solely due to convection. These two air flow conditions allowed for the investigation and comparison of the contributions of evaporative and convective water removal.

Two imaging methods were utilized: a stop-and-shoot protocol used to quantify the maximum saturation for both GDLs, and an on-the-fly setup used to determine the rate of water removal and to visualize the transient desaturation process. For the experiments done with the on-the-fly setup, a small piece of polyethylene was placed between the GDL sample and the plenum. This was added for these rate-based

experiments to ensure that water being removed by the air stream was only coming from the GDL. Without the polyethylene, water from the plenum would artificially inflate the desaturation time. If the experiment was instead run with an empty plenum, water from the GDL would drain out into the empty plenum, artificially reducing the desaturation rate. This step was not needed in the stop-and-shoot protocol.

3.2.3 Synchrotron Setup/Parameters

All imaging experiments described in this work were performed at the 3rd generation synchrotron facility Canadian Light Source Inc. (CLS) (Saskatoon, Canada) at the BioMedical Imaging and Therapy (BMIT) 05B1-1 beamline [30]. All images were taken using the white beam, with the sample located 50 cm away from the detector in order to obtain additional phase contrast. The detector used was a Hamamatsu AA40 beam monitor coupled to a Hamamatsu ORCA Flash 4.0 camera with a pixel size of 6.4 μm. The higher photon flux obtainable using the white beam allowed for a fast CT scan, enabling the visualization of the desaturation process. Each CT scan was done in 9 seconds with 1500 projections in 180° rotation. Due to computer processing requirements, a CT scan could be taken every 1.5 minutes.

3.2.4 Image Processing

The first step in the image processing was to complete the background correction using ImageJ [31]. This involved using dark-field and flat-field images to correct for any monochromator, filter, or detector artifacts within the images. CT Reconstruction was then performed using NRecon 1.7.1.0 (Bruker). The reconstructed images were then

rendered for further analysis using Avizo 9.0 (FEI Visualization Sciences Group). Through this program, segmentation was performed by differentiating between the air, liquid water, and GDL fibers based on their absorbance values. For the quantification, the volume of the dry GDL was subtracted from the volume of the water and GDL, leaving the volume of the water. This value was then divided by the total volume sampled to calculate a percentage saturation value for each GDL.

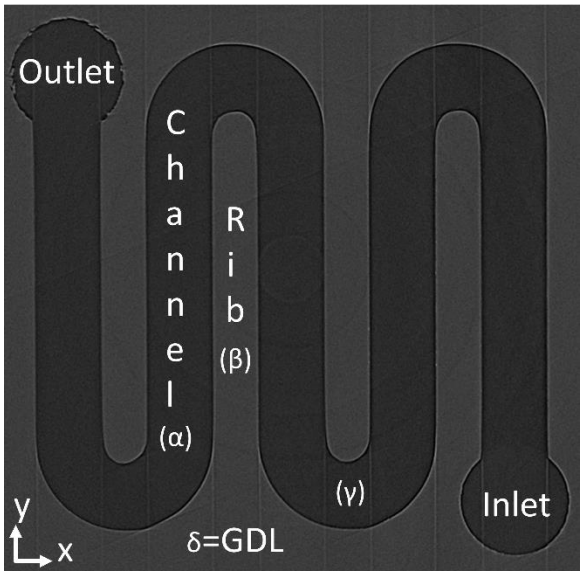

Figure 15. X-ray image of flow field with annotations establishing coordinate layout, inlet, outlet, and symbols to denote features in following images including channel, rib, bend, and GDL.

3.3 Results and Discussion

This section first examines the spatially resolved 2-D and 3-D images of the desaturation process for the two flow conditions described in Table 4 for both of the GDL samples. The quantified results for initial saturation and desaturation rate for both GDL samples are then presented and discussed.

3.3.1 Water Removal Visualization

The results for the dry flow condition for the two GDLs are discussed first and then contrasted with the results from the humidified flow condition. A basic schematic of the flow field with annotated symbols, which will be used to indicate features in following figures, is presented in Figure 15. All following images are arranged in the same manner with the same coordinate layout for consistency. Three images from the experiment using dry air for the desaturation of the 25 AA GDL are presented in Figure 16, showing the initial saturation, saturation after 8.5 minutes of flow, and the final saturation after 16 minutes of flow.

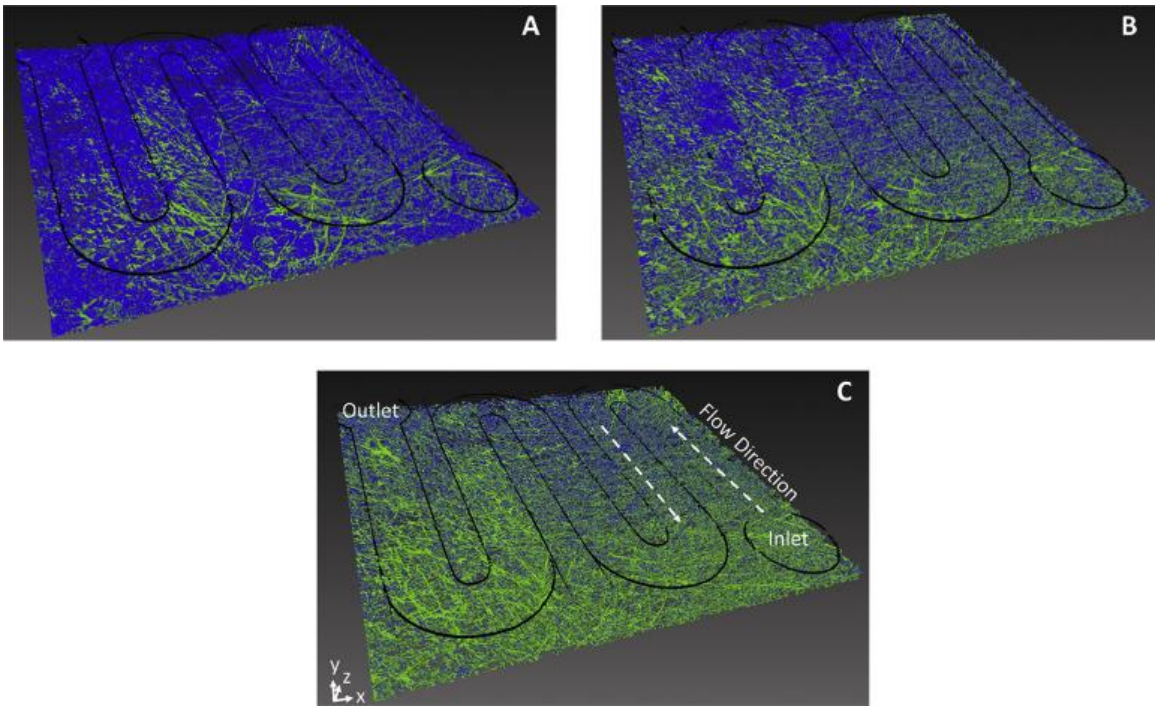

Figure 16. Visualization of desaturation process with dry air with the 25 AA GDL where blue represents water and green represents GDL fiber. A) Initial saturation 25 AA, B) saturation after 8.5 minutes, C) final saturation after 16 minutes.

These images demonstrate a significant initial saturation, as should be expected for a GDL without any sort of PTFE treatment. A more detailed quantitative analysis of the initial saturation can be found below, but for reference, the initial saturation was calculated as 20.4% dropping to 10.4% after 8.5 minutes of flow. Additionally, an overall saturation gradient is observed from the inlet to the outlet can be seen in Figure 16-B. Further confirmation of these observations is seen in the selection of projection images at different locations as presented in Figure 17. Looking at the projections in Figure 17-A, it is seen that the water both fully penetrates the GDL and forms a film underneath the ribs of the gas flow channel. In the YZ projection under the rib, a meniscus can be seen at the edge of the rib near the bend.

Figure 17-B demonstrates that the GDL first desaturates near the inlet, progressing towards the outlet. In the XZ image, a saturation gradient is seen in the same direction as the overall flow field (indicated by the arrow). In comparing the GDL saturation under the first and last channel, a clear difference in saturation is also seen. Finally, the projection taken under the rib shows a slight reduction in the water film, specifically near the channel bend, but a major water film is still noted. In the final collection of projections in Figure 17-C, a fully desaturated GDL is seen in the XZ slice, and the YZ slice under the rib shows that the water film has been fully removed.

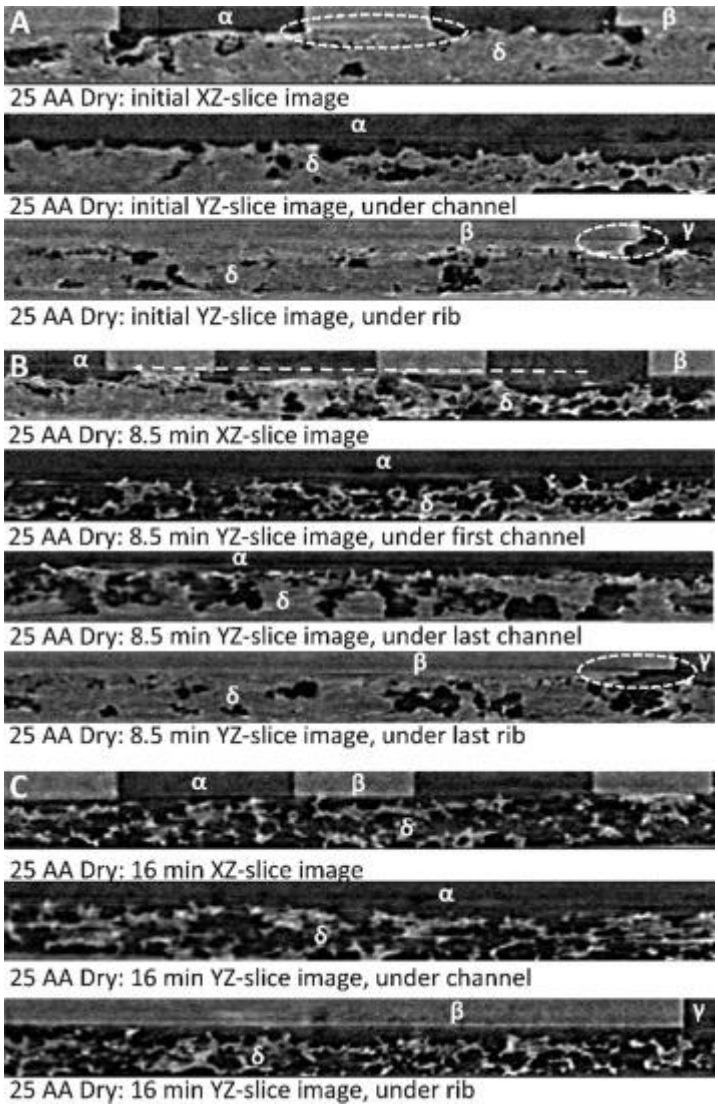

Figure 17. Projection images from the desaturation of the 25 AA GDL using dry air, symbols referenced above in Figure 15. A) Initial XZ projection and YZ projections under a channel and rib, B) XZ projection and YZ projections under the first channel, last channel

Figure 18 shows the 3-D reconstruction of the initial and final saturation for dry air experiment with the 25 BA GDL. The 25 BA GDL shows a much lower initial saturation, calculated to be 1.3%, as should be expected from a more hydrophobic GDL.

From the 3-D images, it appears that the water does not penetrate into the pore space and instead rests on the top of the GDL. This observation is confirmed in the 2-D projection images of the initial state, presented in Figure 19-A.

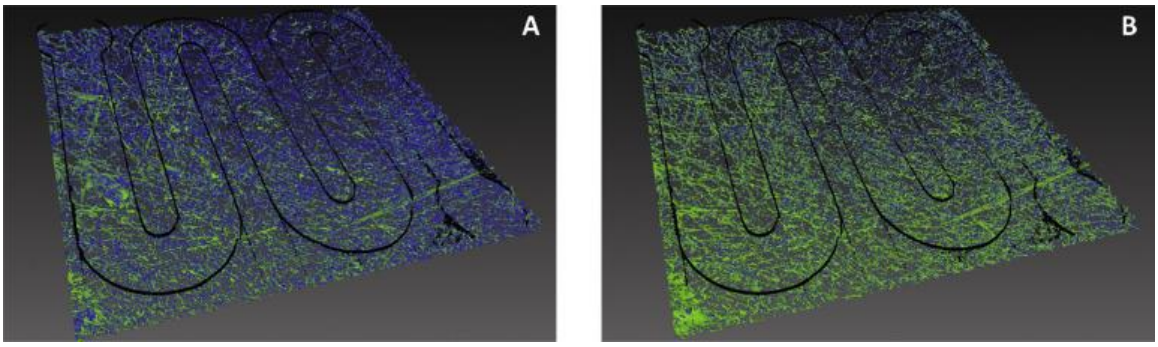

Figure 18. Visualization of desaturation process of the 25 BA GDL with dry air, where blue represents water and green represents GDL fiber. A) Initial saturation 25 BA, B) Final saturation after 2.5 minutes of dry airflow 25 BA.

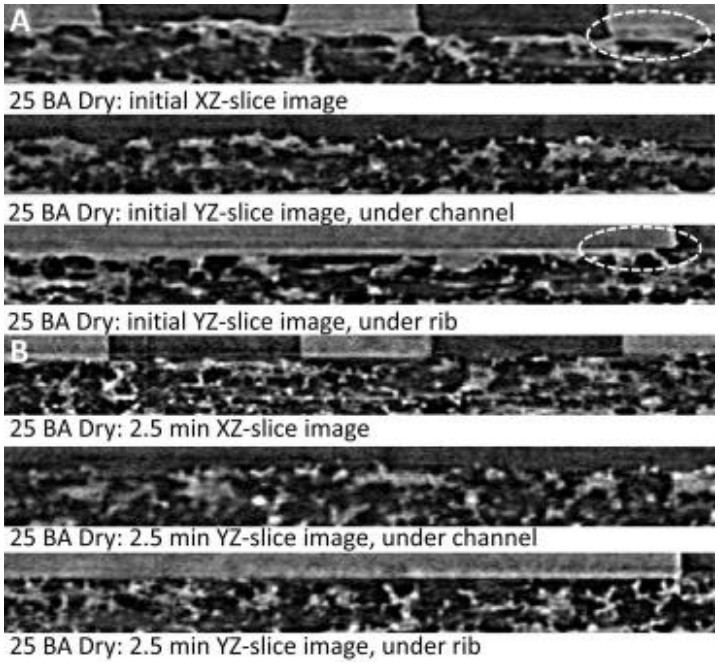

Figure 19. Projection images from the desaturation of the 25 BA GDL with dry airflow. A) Initial XZ projection and YZ projections under a channel and rib B) XZ projection and YZ projections under the first and last channel, and rib after 2.5 minutes of dry air flow

Similar to the 25 AA GDL, a film of water can be seen underneath the ribs; however, no significant penetration into the pore space is observed. In the final saturation projections in Figure 19-B, it can be seen that the water film underneath the ribs has been fully removed.

Figure 20 shows 3-D reconstructions of selected time points from the humid desaturation tests for both GDL samples. In setting up the initial condition for these tests, the water was allowed to pool on top of the GDL, effectively flooding the channel. This was done to fully capture any convective removal effects that would have otherwise been overlooked if any sort of initial gas purge had been performed in order to void the channels. Due to this channel flooding, the channel outline disappears on the images due to the loss of phase contrast, exhibited in Figure 20-A and D.

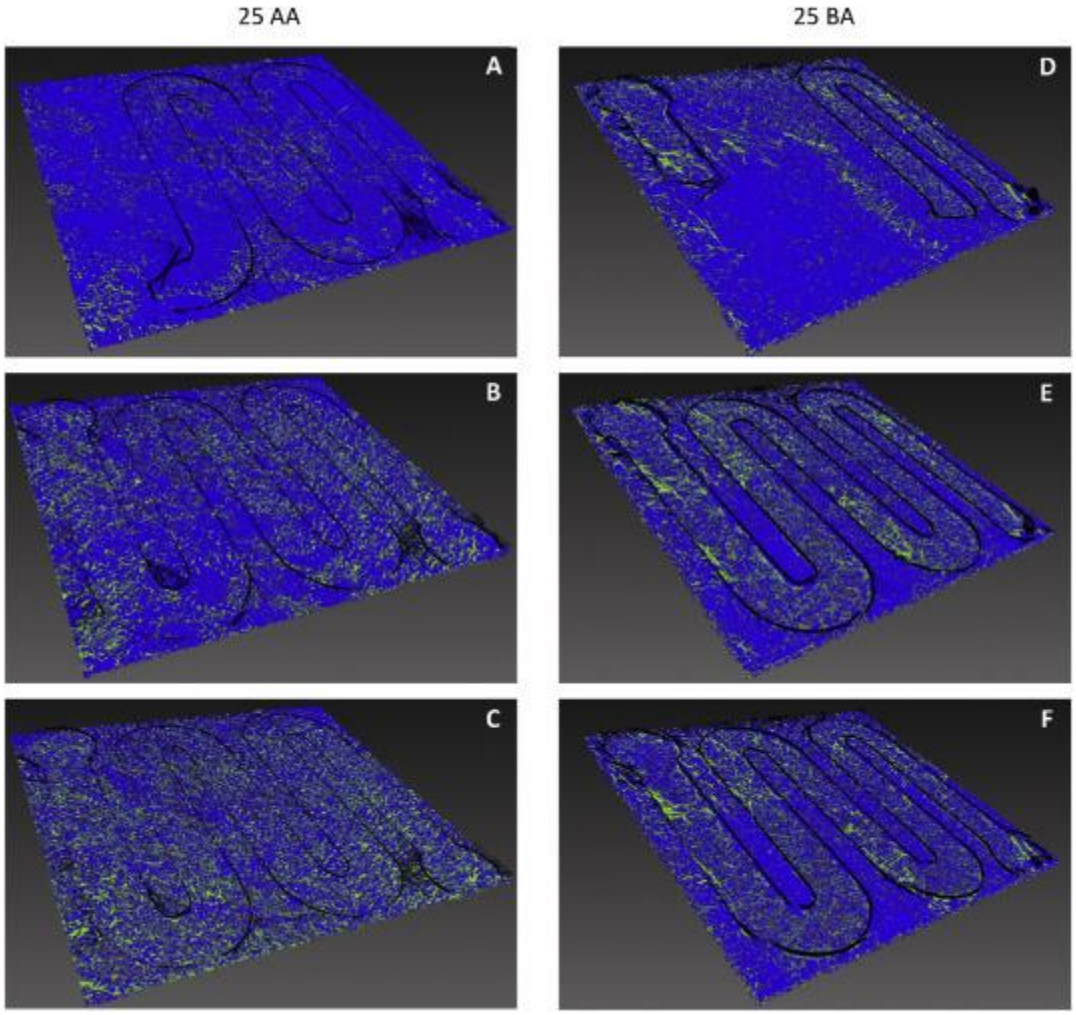

Figure 20. Visualization of desaturation process with humid air where blue represents water and green represents GDL fiber. The gas channel orientation is denoted in black with the inlet on the bottom left and outlet on the upper right. A) initial saturation 25 AA, B) saturation after 20 minutes of humid air flow 25 AA, C) final saturation after 46 minutes of humid air flow 25 AA, D) initial saturation 25 BA, E) saturation after 1 minute of humid air flow 25 BA, F) Final steady state saturation after 22 minutes of humid air flow.

Following the progression of images for both GDLs, the humid airflow alone is not able to fully desaturate either GDL. Interestingly, the residual water for the 25 AA GDL test is found within the pore space, whereas the residual water in the 25 BA GDL test remains directly underneath the ribs. For both cases, the majority of the water that is

removed comes from directly underneath the gas channels, where it can easily be convected out of the cell. These observations are confirmed by the 2-D projections presented in Figure 21 and Figure 22.

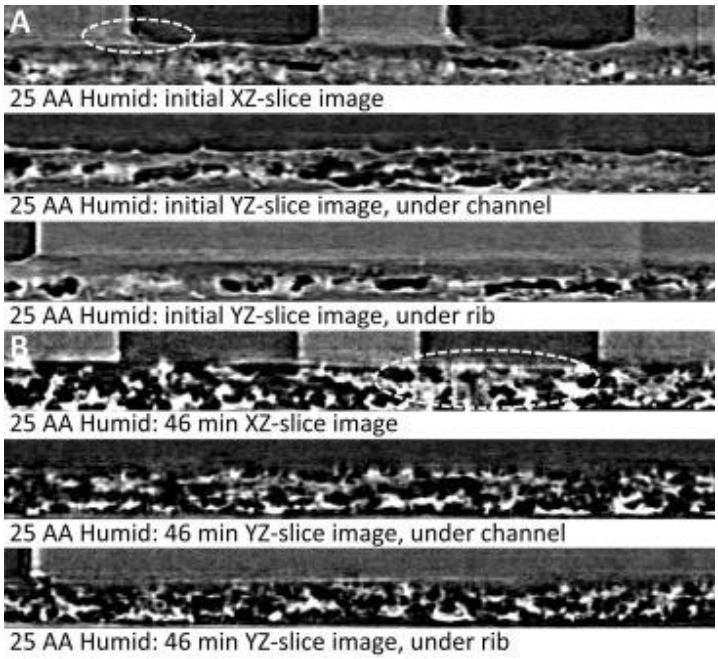

Figure 21. Projection images of initial and final saturation states for the humid flow condition for 25 AA GDLs. The final image was taken after 46 minutes of flow.

In Figure 21-A, the projections show that a film formed underneath the ribs and that there was a large general penetration of water into the pore space of the GDL, similar to the initial images for the dry air experiments. However, in Figure 21-B, it can be seen after 46 minutes of flow, which amounts to almost three times as long as the dry air experiment, that although the film underneath the ribs has been removed, the GDL is still not completely desaturated, as seen in Figure 17-C. In the initial 25 BA projections in Figure 22-A, a film underneath the ribs is seen, as well as a film of water on the top of the GDL. However, as seen in Figure 19-A, the overall water penetration into the pore space

is much lower even with a fully flooded channel above the GDL, outlined in white. The final projections in Figure 22-B show that the film underneath the ribs has not been removed, but that the film of water beneath the gas channels themselves is no longer present. The projection images show a difference in the desaturation preferences for the two GDLs. The 25 AA GDL seems more able to desaturate underneath the rib area while retaining saturation within the pore space, likely due to its lack of any PTFE coating. For the 25 BA GDL, the water underneath the ribs is entrained and unable to be removed by simple convection. One possibility to explain this discrepancy is that in the 25 AA case, as some of the water is removed from the pore space, the water underneath the ribs is then drawn into the GDL; however, further experimentation is required to confirm this hypothesis.

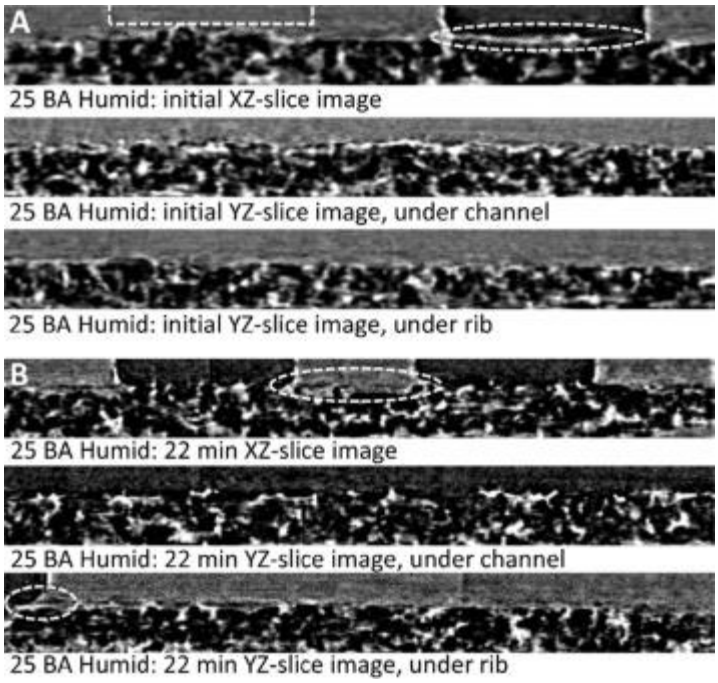

Figure 22. Projection images of initial and final saturation states for the humid flow condition for 25 BA GDLs. The final image was taken after 22 minutes of flow.

The results from the visualization provide some interesting insight and confirmation of previous findings. Multiple modeling studies and approaches investigating the coupled thermal and water management of fuel cells have concluded that condensation and accumulation occurs underneath the ribs of the channels due in part to the temperature gradient [32, 33]. Additionally, a range of visualization studies of active fuel cells have confirmed the accumulation of water beneath the channel ribs [24, 34, 35] and have even suggested that certain GDLs can deter this accumulation [26]. Serpentine flow channels have been widely used due in part to their increased pressure drop, which helps to increase in-plane convection [36]. Results from this study suggest that in order to effectively remove this accumulated water, an evaporative component must be introduced, since a convective effect alone appears unable to remove this excess water.

3.3.2 Saturation and Evaporation Rate Quantification

The stop-and-shoot experiment was run for the 25 BA and 25 AA GDLs to determine their maximum saturation. A summary of these quantified values can be seen in Table 5.

Table 5. Calculated percentage saturation for both GDLs based on the stop-and-shoot experiments

	25 BA	25 AA
Sampled Volume [mm^3]	7.097	7.035
GDL Fiber Volume [mm^3]	3.191	3.135
Water Volume [mm^3]	0.089	1.504
Initial Saturation	1.3%	21.4%

The saturation level for the 25 AA GDL is close to the critical saturation level above which cell failure occurs, identified as 20% by Wang and Nguyen [37] via neutron imaging. Of note, the 25 BA saturation level is lower than those reported from in-situ studies, due to the fact that the constant water generation from the electrochemical reaction was not captured in this study. Using these initial saturation values, the on-the-fly experiments were then used to determine an evaporation rate for both of the GDLs with dry airflow, reported in Table 6. Values for the humid removal rates could not be determined since full desaturation of the GDLs was never reached. In these experiments, a steady state of GDL water saturation developed, as discussed in detail in the visualization section.

Table 6. Desaturation rate results for the more hydrophobic (25 BA) and more hydrophilic (25 AA) GDLs

	25 BA	25 AA
Time to Dry [min]	2.5	16
Initial Water Volume [cm^3]	0.19	0.32
Water Removal Rate [g/min]	0.07	0.02

Since the CT scans were taken every 1.5 minutes, as detailed above, the reported evaporation times are the most conservative estimate, based on the identified CT scan when full desaturation had been achieved. Although the full CT scan time was 9 seconds, it was found that no transience within the system was lost in this sampling window, due in part to the experiments being operated at room temperature. Nonetheless, the evaporation rate of 0.07 g min^{-1} determined for the 25 BA sample is very close to the value of 0.05 g min^{-1} reported by Zenyuk et al [38] in their study of evaporation rates over a range of saturation values. The reported initial water volume was calculated based

on the initial saturation value as determined above and the full volume of the GDL sample. Interestingly, the desaturation rate for the 25 BA is nearly four times faster than the rate for the 25 AA sample. From the initial projection images for 25 BA, specifically Figure 19-A, it is seen that the majority of the initial water was only present on the surface of the GDL and did not penetrate into the pore space in any major way. Therefore, all of the desaturation for the 25 BA occurs within the "Surface Evaporation Regime," the fastest of the three evaporation regimes identified previously by Cho and Mench [39]. For the 25 AA sample, the lack of the PTFE coating allowed water to clearly penetrate into the pore space, seen in Figure 17-A, meaning its desaturation process would also include the slower evaporation regimes, referred to as the "Constant Rate Period" and "Falling Rate Period" [39], explaining the slower desaturation rate.

3.4 Conclusion

The transient 3-D visualization of the desaturation process of two different commercial GDLs was for the first time performed using synchrotron X-ray CT. For both GDLs, a comparison of convective and evaporative removal is shown. For the more hydrophobic 25 BA GDL, an initial saturation of 1.3% was seen with a majority of the initial water found to lay on the surface of the GDL, with minimal penetration into the pore space. When subjected to evaporation and convection, the full desaturation of the GDL occurred in 2.5 minutes. When only convective removal was used, the full desaturation was not achievable, with a portion of water remaining trapped underneath the channel ribs. For the more hydrophilic 25 AA GDL, an initial saturation of 21.4%

was achieved. This GDL was fully desaturated by convective and evaporative forces within 16 minutes, for a rate nearly four times slower than that of the 25 BA GDL. Similar to the 25 BA GDL, convective removal alone was not sufficient to fully desaturate the 25 AA GDL. However, the water was found to remain within the pore space rather than underneath the channel ribs, as seen with the 25 BA sample.

Acknowledgements

LFZ and RA acknowledge the support from their respective universities, the University of Saskatchewan and Montana State University. This collaboration was also supported under NSF Award number 1444198. Research described in this paper was performed at the BMIT facility at the Canadian Light Source, which is supported by the Canada Foundation for Innovation, Natural Sciences and Engineering Research Council of Canada, the University of Saskatchewan, the Government of Saskatchewan, Western Economic Diversification Canada, the National Research Council Canada, and the Canadian Institutes of Health Research.

References

1. Fuel Cell Technologies Office Multi-Year Research, Development, and Demonstration Plan. 2016, Department of Energy. p. 3.4 1-58.

2. Wang, Y., et al., A review of polymer electrolyte membrane fuel cells: Technology, applications, and needs on fundamental research. Applied Energy, 2011. 88(4): p. 981-1007.

3. Park, J., et al., A review of the gas diffusion layer in proton exchange membrane fuel cells: Durability and degradation. Applied Energy, 2015. 155: p. 866-880.

4. Lapicque, F., et al., A critical review on gas diffusion micro and macroporous layers degradations for improved membrane fuel cell durability. Journal of Power Sources, 2016. 336: p. 40-53.

5. Yousfi-Steiner, N., et al., A review on PEM voltage degradation associated with water management: Impacts, influent factors and characterization. Journal of Power Sources, 2008. 183(1): p. 260-274.

6. Ous, T. and C. Arcoumanis, Degradation aspects of water formation and transport in Proton Exchange Membrane Fuel Cell: A review. Journal of Power Sources, 2013. 240: p. 558-582.

7. Banerjee, R. and S.G. Kandlikar, Two-phase flow and thermal transients in proton exchange membrane fuel cells – A critical review. International Journal of Hydrogen Energy, 2015. 40(10): p. 3990-4010.

8. Alink, R., et al., The influence of porous transport layer modifications on the water management in polymer electrolyte membrane fuel cells. Journal of Power Sources, 2013. 233: p. 358-368.

9. Chen, H.-H. and M.-H. Chang, Effect of cathode microporous layer composition on proton exchange membrane fuel cell performance under different air inlet relative humidity. Journal of Power Sources, 2013. 232: p. 306-309.

10. Li, A. and S.H. Chan, Understanding the role of cathode structure and property on water management and electrochemical performance of a PEM fuel cell. International Journal of Hydrogen Energy, 2013. 38(27): p. 11988-11995.

11. Owejan, J.P., et al., Water Transport Mechanisms in PEMFC Gas Diffusion Layers. Journal of The Electrochemical Society, 2010. 157(10): p. B1456-B1464.

12. Morgan, J.M. and R. Datta, Understanding the gas diffusion layer in proton exchange membrane fuel cells. I. How its structural characteristics affect diffusion and performance. Journal of Power Sources, 2014. 251: p. 269-278.

13. Yau, T.C., et al., Water transport and Schröder's Paradox in fuel cell membrane electrode assemblies. Journal of Power Sources, 2013. 224: p. 285-289.

14. Hussaini, I.S. and C.Y. Wang, Dynamic water management of polymer electrolyte membrane fuel cells using intermittent RH control. Journal of Power Sources, 2010. 195(12): p. 3822-3829.

15. Song, M., et al., Water management of proton exchange membrane fuel cell based on control of hydrogen pressure drop. Journal of Power Sources, 2014. 267: p. 655-663.

16. Damour, C., et al., A novel non-linear model-based control strategy to improve PEMFC water management – The flatness-based approach. International Journal of Hydrogen Energy, 2015. 40(5): p. 2371-2376.

17. Battrell, L., et al., Quantifying Cathode Water Transport via Anode Relative Humidity Measurements in a Polymer Electrolyte Membrane Fuel Cell. Energies, 2017. 10(8): p. 16.

18. Bazylak, A., Liquid water visualization in PEM fuel cells: A review. International Journal of Hydrogen Energy, 2009. 34(9): p. 3845-3857.

19. Hussaini, I.S. and C.Y. Wang, Visualization and quantification of cathode channel flooding in PEM fuel cells. Journal of Power Sources, 2009. 187(2): p. 444-451.

20. Deevanhxay, P., et al., Effect of liquid water distribution in gas diffusion media with and without microporous layer on PEM fuel cell performance. Electrochemistry Communications, 2013. 34: p. 239-241.

21. Iranzo, A., et al., Water build-up and evolution during the start-up of a PEMFC: Visualization by means of Neutron Imaging. International Journal of Hydrogen Energy, 2017. 42(19): p. 13839-13849.

22. Banerjee, R., et al., Transient Liquid Water Distributions in Polymer Electrolyte Membrane Fuel Cell Gas Diffusion Layers Observed through In-Operando Synchrotron X-ray Radiography. Journal of The Electrochemical Society, 2017. 164(2): p. F154-F162.

23. Lamibrac, A., et al., Characterization of Liquid Water Saturation in Gas Diffusion Layers by X-Ray Tomographic Microscopy. Journal of The Electrochemical Society, 2016. 163(3): p. F202-F209.

24. Krüger, P., et al., Synchrotron X-ray tomography for investigations of water distribution in polymer electrolyte membrane fuel cells. Journal of Power Sources, 2011. 196(12): p. 5250-5255.

25. Lee, J., et al., Synchrotron Investigation of Microporous Layer Thickness on Liquid Water Distribution in a PEM Fuel Cell. Journal of the Electrochemical Society, 2015. 162(7): p. F669-F676.

26. Chevalier, S., et al., Novel electrospun gas diffusion layers for polymer electrolyte membrane fuel cells: Part II. In operando synchrotron imaging for microscale liquid water transport characterization. Journal of Power Sources, 2017. 352(Supplement C): p. 281-290.

27. García-Salaberri, P.A., et al., Effective diffusivity in partially-saturated carbon-fiber gas diffusion layers: Effect of local saturation and application to macroscopic continuum models. Journal of Power Sources, 2015. 296: p. 440-453.

28. Safi, M.A., et al., Experimental and pore-level numerical investigation of water evaporation in gas diffusion layers of polymer electrolyte fuel cells. International Journal of Heat and Mass Transfer, 2017. 115: p. 238-249.

29. Yan, W.-M., H.-Y. Li, and W.-C. Weng, Transient mass transport and cell performance of a PEM fuel cell. International Journal of Heat and Mass Transfer, 2017. 107: p. 646-656.

30. Wysokinski, T.W., et al., Beamlines of the biomedical imaging and therapy facility at the Canadian light source—Part 1. Nuclear Instruments and Methods in Physics Research Section A: Accelerators, Spectrometers, Detectors and Associated Equipment, 2007. 582(1): p. 73-76.

31. Rasband, W.S., ImageJ. 1997-2016, U.S. National Institutes of Health: Bethesda, Maryland, USA.

32. Cao, T.-F., et al., Numerical investigation of the coupled water and thermal management in PEM fuel cell. Applied Energy, 2013. 112: p. 1115-1125.

33. Aghighi, M. and J. Gostick, Pore network modeling of phase change in PEM fuel cell fibrous cathode. Journal of Applied Electrochemistry, 2017. 47(12): p. 1323-1338.

34. Hartnig, C., et al., High-resolution in-plane investigation of the water evolution and transport in PEM fuel cells. Journal of Power Sources, 2009. 188(2): p. 468-474.

35. Sasabe, T., S. Tsushima, and S. Hirai, In-situ visualization of liquid water in an operating PEMFC by soft X-ray radiography. International Journal of Hydrogen Energy, 2010. 35(20): p. 11119-11128.

36. Lim, B.H., et al., Effects of flow field design on water management and reactant distribution in PEMFC: a review. Ionics, 2016. 22(3): p. 301-316.

37. Wang, X. and T.V. Nguyen, An experimental study of the liquid water saturation level in the cathode gas diffusion layer of a PEM fuel cell. Journal of Power Sources, 2012. 197: p. 50-56.

38. Zenyuk, I.V., et al., Investigating evaporation in gas diffusion layers for fuel cells with X-ray computed tomography. The Journal of Physical Chemistry C, 2016. 120(50): p. 28701-28711.

39. Cho, K.T. and M.M. Mench, Fundamental characterization of evaporative water removal from fuel cell diffusion media. Journal of Power Sources, 2010. 195(12): p. 3858-3869.

CHAPTER FOUR

4-D IMAGING OF THE DESATURATION OF GAS DIFFUSION LAYERS BY SYNCHROTRON RADIOGRAPHY

Contribution of Authors and Co-Authors

Manuscript in Chapter 4

Author: Logan Battrell

Contributions: Conceived and designed experiments, performed experiments, collected and analyzed data, wrote the manuscript

Co-Author: Virat Patel

Contributions: Assisted in design of test cell, provided assistance with data collection

Co-Author: Ning Zhu

Contributions: Provided oversite on data collection and analysis, edited earlier manuscripts

Co-Author: Lifeng Zhang

Contributions: Conceived and designed experiments, edited earlier manuscripts

Co-Author: Ryan Anderson

Contributions: Conceived and designed experiments; analyzed data; provided reagents, materials, and analysis tools; edited manuscripts

Manuscript Information

Logan Battrell, Ning Zhu, Lifeng Zhang and Ryan Anderson

Journal of Power Sources

Status of Manuscript:
____ Prepared for submission to a peer-reviewed journal
_X__ Officially submitted to a peer-reviewed journal
____ Accepted by a peer-reviewed journal
____ Published in a peer-reviewed journal

Elsevier
October 5, 2018

4-D IMAGING OF THE DESATURATION OF GAS DIFFUSION LAYERS BY SYNCHROTRON RADIOGRAPHY

Abstract

The 4-D imaging and quantification of the desaturation of an initially flooded gas diffusion layer (GDL) with a serpentine gas flow channel by synchrotron radiography is presented. An imaging area with a diameter of 10 mm allows for the study of how the natural anisotropy of a GDL affects the desaturation profile. The GDL is progressively spatially segmented from the overall domain down to sections of the individual channels and ribs. Temporal saturation profiles and desaturation rates are presented for each step of this progressive segmentation. Although the desaturation of the overall domain initially appears to be a constant and steady process with a desaturation rate of 0.0030 μL cm^{-2} s^{-1}, segmented results display heterogeneous behavior with over two-fold differences between areas of the flow field. Segmented saturation surface plots are presented that spatially show how this heterogeneity occurs within the entire domain. Results indicate that initial conditions, anisotropic material properties, and flow field geometry all play a key role in determining local desaturation behavior. The larger domain considered here provides valuable data for future modeling studies that combine continuum studies of flow in the gas flow channels with GDL pore network models that consider two-phase flow behavior.

4.1 Introduction

The Gas Diffusion Layer (GDL) is a key component within the Membrane Electrode Assembly (MEA) of Polymer Electrolyte Membrane (PEM) fuel cells. These hydrogen fuel cells have been the focus of research due to their demonstrated potential as scalable energy conversion devices that feature zero local emissions, high power density, and rapid start-up [1]. The GDL is a thin porous layer that is located between the catalyst layer and the gas flow channels within both the anode and cathode. Here, thin refers to a porous media where the layer thickness is of a similar magnitude to a typical pore diameter (L_{GDL} = 100-400 μm, $D_{GDL\text{-}Pore}$ = 1-100 μm)[2]. This thin property introduces problems in studying this layer, since accurate continuum modeling dictates that the domain length should be 10-15 times larger than the average pore size, rather than the one order of magnitude or less difference commonly found in GDLs [3, 4]. Briefly, the GDL is responsible for promoting transport of the reactive species to the catalytic sites, facilitating the removal of product water from the cathode catalyst layer, and conducting electrons with low resistance. Key to its functionality is the proper management of the overall water saturation, specifically maintaining enough water to hydrate the polymer membrane while not accumulating water to the point where the GDL is considered flooded, where gas transport to the catalyst layer is restricted or completely blocked [5, 6]. Poor water management can lead to material degradation, lowered cell performance, and in extreme cases, total cell failure [7, 8].

This critical layer has been reviewed in detail, discussing the various materials, properties, characteristics, and varying structures [2, 7, 9]. As proficient water

management is clearly key to efficient fuel cell operation, numerous approaches have been developed and investigated to address this challenge. These include preventative measures to keep the GDL from ever reaching this flooded state and reactive strategies that desaturate the GDL once it has been identified as heading towards the flooded state. Several groups have studied a variety of material modifications to enhance or better understand water management. These investigations included introducing perforations to the cathode microporous layer (MPL) [10], varying the MPL composition based on the operating conditions of the cell [11], varying the hydrophobicity and structure of various cathode layers to optimize electrochemical performance of the cell [12], and utilizing a double layered GDL with a hydrophobicity gradient [13]. Additionally, new materials and architectures have been investigated to determine if they could potentially replace traditional layers. This includes replacing the cathode bipolar plate with a hydrophilic water transport plate [14], the investigation of novel electrospun GDLs and their effect on water management [15], as well as numerous studies into various flow fields designed to promote water removal, previously reviewed [16]. Many reactive strategies rely on some sort of signal analysis combined with an operational change to reduce or remove performance losses [17]. All of these net water management strategies are in effect governed by the pore scale water dynamics occurring within the GDL. For example, a proposed dynamic intermittent humidification scheme evaporates excess water based on voltage monitoring functions by removing excess water both convectively and through evaporation [18]. Additionally, an air flow control system was designed to regulate the overall water content within the cell, based on a model that controls the humidification of

the air stream [19]. Finally, a diagnostic technique was developed to quantify the desaturation of a flooded cathode based on an analysis of the anode pressure drop and the use of a dry anode stream [20]. As the pore-scale behavior is difficult to quantify, these control schemes are empirical and often specific to a cell's geometry or operating condition. In order to better understand the basic transport phenomena and governing properties, recent work has focused on numerical modeling and experimental visualization at the pore scale, which has the potential to allow for intelligent material design and better informed control schemes.

Various modeling strategies have been implemented to try to better understand water accumulation and transport within the GDL. Recent reviews of both performance and transport models was provided by Wu [21] and of cell-scale multiphase flow modeling by Andersson et al. [22]. As mentioned, one of the distinguishing factors of a GDL when compared to other porous materials is the fact that its pore size is on the same scale as the overall thickness of the layer. A recent investigation by García-Salaberri et al. [23] showed that a representative element volume for a GDL could not be identified in the through-plane due to its relative thinness in relation to the average pore size. To address this problem, one approach that has expanded is pore network models (PNM). Through PNM, researchers have been able to represent the GDL as a network of interconnected throats and pores and have simulated two-phase flow. Recently, Aghighi and Gostick [24] created a PNM to predict phase changes and capture local water distributions with a constant voltage boundary under different operating conditions. Similarly, Belgacem et al. [25] created a coupled continuum and condensation PNM to

investigate water accumulation in a PNM when coupled with the electrochemical phenomena occurring at the catalyst layer. Additionally, Medici et al. [26] utilized a coupled continuum-PNM model to understand how stacking anode GDLs increased performance. X-ray computed tomography (X-ray CT) was used to extract GDL properties, used as inputs for the model. Due to computational requirements, all of these models have limited their unit geometry to be roughly the width of one channel and rib. However, as computational capabilities expand, the need for larger domain data sets will be key in potentially validating results or seeding initial conditions. Since the GDL presents a unique case, experimental data is necessary to help validate the development of new models and inform new material designs.

To address these needs, the visualization of both the saturation and desaturation of this critical layer has been a research focus in recent years. Synchrotron radiography is a key technique to measure water in PEM fuel cells due to its sufficient phase contrast and high temporal and spatial resolution, allowing for the visualization and quantification of water content within the various layers of the MEA [27]. Synchrotron radiography has been used by Kruger et al. [28] to visualize the increasing cathode GDL saturation as the current density of the cell is increased, by Lee et al. [29] to investigate the effect of MPL thickness on GDL water saturation, and by Arlt et al. [30] to investigate the effect of aging on GDL water management capabilities. Muirhead et al. [31] quantified the relation between liquid water saturation and oxygen transport resistance and found that existing correlations relating porosity and saturation to diffusivity could be improved by GDL-specific tuning. The majority of these studies were 2-D investigations in the in-plane of

the fuel cell, likely due to the limiting nature of the components necessary for an operating fuel cell, specifically the metallic and graphite components, both of which have high absorptivity. X-ray CT is a specific visualization tool that has also been used to investigate different aspects of the desaturation of a GDL. Recently, Lal et al. [32] used a laboratory CT scanner to take images of a 1 mm x 1 mm region of a GDL with a single channel to determine the effect of temperature on the GDL evaporation rate. Zenyuk et al. [33] used synchrotron X-ray CT to take measurements of a 3.8 mm diameter GDL sample with a single gas channel and determined the effect that GDL saturation had on the evaporation rate.

In summary, the visualization of water accumulation and desaturation within the GDL is a topic that has received recent attention. Although many groups have examined this effect in 2-D with an active cell or in 3-D with a single channel, the research of desaturation of a full GDL domain in 3-D with a typical fuel cell flow field geometry is something that has not thoroughly been investigated. Recently, synchrotron X-ray CT was used by Battrell et al. [34] to investigate the transient desaturation process to separate the relative contributions of evaporation and convection to the overall GDL desaturation process of a 10 mm diameter sample by a 5 channel serpentine gas flow channel. The present work expands on this previous study by further investigating and quantifying the spatial gradients present within the GDL over time. This 4-D information is valuable to the modeling community, which could use this data to validate and confirm theoretical models. These results can also inform future GDL designs, which may be able to better intrinsically assist in the overall water management of the fuel cell. Saturation gradients

are broken down from overall desaturation profiles, to rib and channel, down to individual ribs and channels, and finally the segmentation of each rib and channel, allowing for a more detailed spatial and temporal investigation of the desaturation of this thin porous media.

4.2 Methods

The protocols used for this study were discussed in detail previously [34], and are presented briefly here for reference, as well as to highlight improvements made in order to facilitate further data analysis.

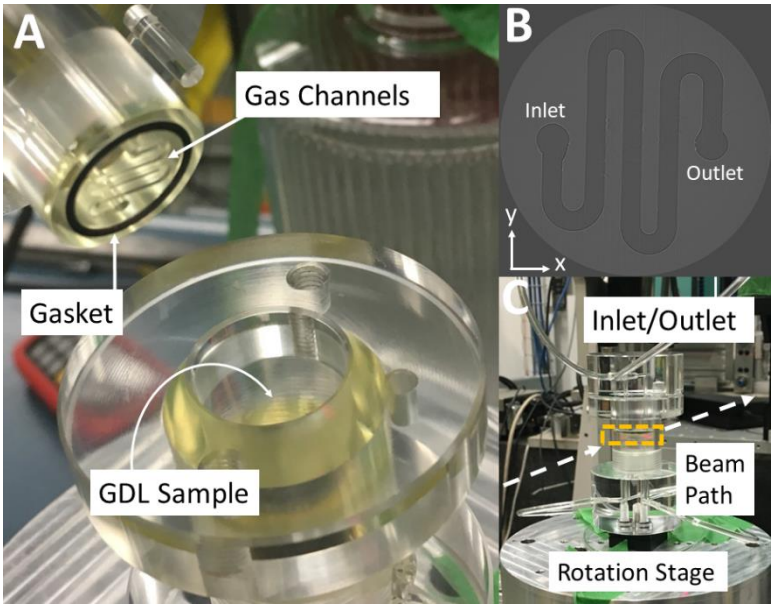

Figure 23. A) Disassembled cell displaying gas channels, gasket, and where the GDL is placed in the bottom piece, B) X-ray image of gas flow field with labeled inlet and outlet, and C) assembled flow cell in beam setup, with the imaging area highlighted in yellow.

4.2.1 Desaturation Protocol

The protocol for the desaturation of the GDL sample was the same used in the previous study [34] and is briefly reviewed here. The GDL sample was initially saturated by being submersed in a water bath and agitated for 1 minute. The GDL was then placed within the acrylic test cell, seen in Figure 23-A, which was then closed and tightened until water could be seen within the gas channels on top of the GDL. After taking an Stop-and-shoot (S+S) CT scan to establish initial saturation, dry air at room temperature (22°C) was introduced at a flowrate of 50 N ml min^{-1}, corresponding to the required flowrate to operate a fuel cell at 1000 mA cm^{-2} at a stoichiometric point of 2. On-the-fly (OTF) scans were then collected every minute, based on the computational limits of the image acquisition computer, for the first 30 minutes of the experiment, and then every 5 minutes. Data collection was reduced at this later period due to memory requirements and because the most dynamic transient behavior occurred early on in the test.

4.2.2 Sample Description and Flow Cell Design

The focus of the study was on the 35 AA GDL from Sigracet. Although a GDL without any hydrophobic treatment is not traditionally used in PEM fuel cell applications, this GDL is the substrate from which the 35 BA (5% PTFE) and 35 BC (5% PTFE and MPL) GDLs are made from. These GDLs were not investigated because previous results showed that the BA GDL fully desaturates in this setup in roughly 2.5 minutes [34], making the spatial gradients and transient desaturation much harder to visualize and quantify. Since the AA GDL is able to initially saturate to a much higher percentage, and the overall desaturation time is roughly four times slower, capturing the intermediate

saturation profiles at sufficient temporal resolution was made possible by selecting this material instead. The acrylic test cell used for this study had the same overall specifications as the one used previously, with a small change to the gas channel geometry that allowed for the increase of the overall channel length to 39.1 mm. Specifically, the gas channel, seen in Figure 23-B, was 1 mm (w) x 0.5 mm (d), the first and last ribs had a width of 1.2 mm, and the middle two ribs had a width of 0.8 mm.

4.2.3 Synchrotron Setup/Parameters

All of the imaging experiments for this study were performed at the 3rd generation synchrotron facility Canadian Light Source Inc. (CLS) (Saskatoon, Canada) at the BioMedical Imaging and Therapy (BMIT) 05B1-1 beamline [35]. All beam parameters, including the high intensity white beam (polychromatic beam), sample to detector distance (50 cm), detector (Hamamatsu AA40) and camera (Hamamatsu ORCA Flash 4.0) with a pixel size of 6.4 µm were the same as used in the previous study [34]. This setup allowed for two CT scan modes, a sub 10 second OTF scan mode, consisting of 1500 projections, and a high-quality S+S scan mode, consisting of 2250 projections. For the OTF protocol, CT scans could be consecutively conducted every minute and the data acquisition time was currently limited by the mechanical capacity of the rotation stage. Figure 23-C shows the acrylic test cell on the rotation stage, highlighting both the imaging area and beam path.

4.2.4 Image Processing and GDL Spatial Analysis

Background correction was performed with ImageJ [36] using dark-field and flat-field images to correct for any artifacts that might have been introduced by the monochromator, filter, or detector. The 3-D reconstruction was then performed with NRecon 1.7.1.0 (Bruker). These full CT images were then loaded into MetaMorph (Molecular Devices LLC) for post-reconstruction analysis, specifically segmentation and quantification. For this study, the GDL was progressively segmented into smaller and smaller regions in order to separate spatial saturation gradients from the overall desaturation profile. These different segmentation orientations and the naming conventions used throughout the rest of the paper can be seen in Figure 24. In all cases, the saturation represents the liquid volume in the various domains, e.g. the entire GDL or channel 1. The transient desaturation rates are calculated by considering the difference in saturation every five minutes, normalized by the cross sectional area in the through plane of the segment being analyzed. This approach reduces the noise associated with analysis every minute and is consistent with the time-steps at the end of the trial. Thus, eight rates are presented for the 40 minutes of collected data.

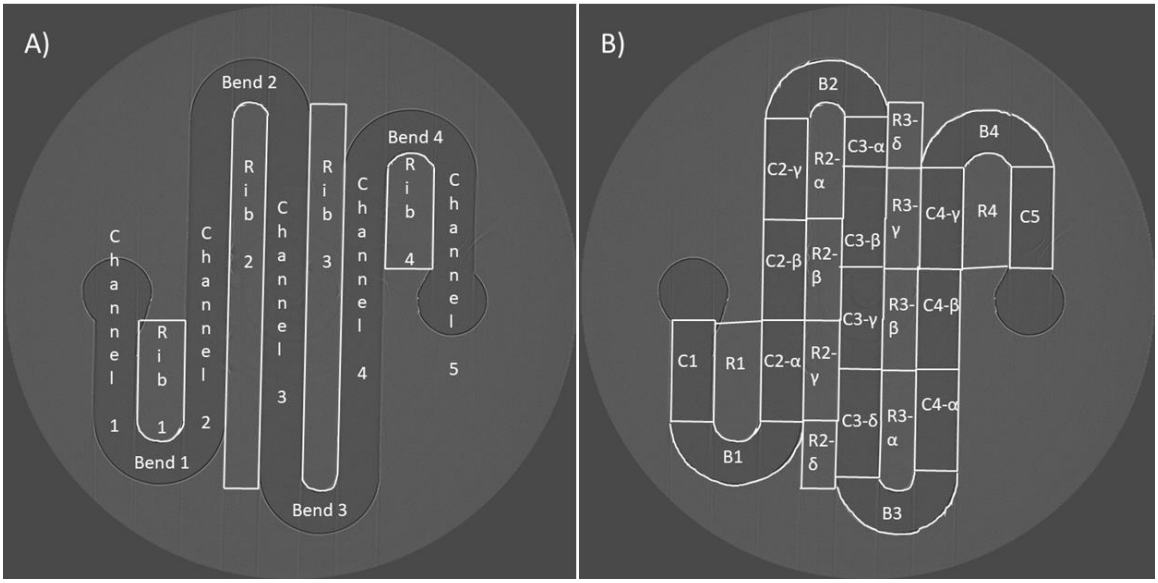

Figure 24. A) Schematic showing the naming convention for individual channels and ribs and B) the full segmentation geometry and further naming conventions (C=channel, R=rib, B=bend) used for subsequent data analysis.

4.3 Results

The temporal saturation profiles and transient desaturation rates are examined as the domain is segmented down from the overall domain, to channels and ribs, then to the individual channels and ribs, and finally to the spatially segmented saturation profile. This section focuses on the specific results of this study, while the discussion section focuses on comparisons to other published studies including published desaturation rates and pore network models.

4.3.1 Desaturation Quantification of the Entire GDL Sample

The first analysis was to consider the overall desaturation of the entire GDL domain, presented as the temporal saturation profile and transient desaturation rates in Figure 25. Based on the initial saturation, time to fully desaturate, and the volume of the

domain, the overall desaturation rate is calculated to be 0.0030 μL cm^{-2} s^{-1}. If all of the transient desaturation rates are averaged, the same overall desaturation rate is found, with a standard deviation of 0.0013 μL cm^{-2} s^{-1}. From this figure, it is seen that the overall GDL desaturation has two approximately linear regions, with the transition between them happening between the 15 and 20 minute mark that corresponds with a step-change in the desaturation rate from 0.0018 ± 0.0002 μL cm^{-2} s^{-1} to 0.0042 ± 0.0004 μL cm^{-2} s^{-1}.

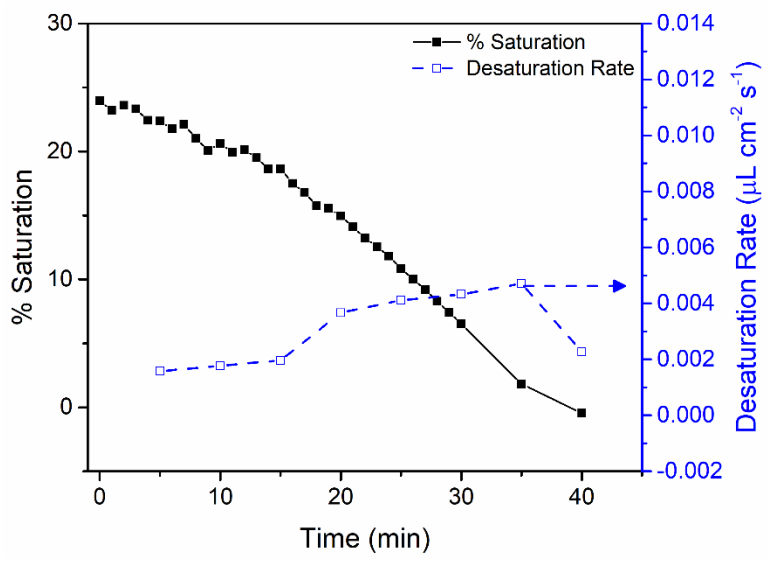

Figure 25. Temporal saturation profile and transient desaturation rate for the overall GDL domain. For reference, the desaturation rate is calculated as a 5 minute average

4.3.2 Desaturation Quantification: Channels vs. Ribs

The next step in the analysis of the desaturation profile was to isolate the channel and rib saturation from overall profile. The channel domain is comprised of the four bends and channels 1-5, while the rib domain is the average of ribs 1-4, as specified in Figure 24-A. It is key to point out that in this segmentation some of the outer area that

was previously included in the overall analysis was cropped out to only include rib directly located next to two channels. In Figure 26, the temporal saturation profiles and transient desaturation rates are presented for both the channel and rib domains. At this stage of segmentation, the overall desaturation rates for both the channel and rib domains are calculated to be similar to that of the overall GDL, 0.0034 ± 0.0012 μL cm^{-2} s^{-1} and 0.0031 ± 0.0025 μL cm^{-2} s^{-1} respectively. Interestingly, the temporal saturation profile underneath the channels is very similar to the overall GDL temporal saturation profile, seen in Figure 25. Comparing these two saturation profiles to the profile underneath the ribs, an interesting difference is found. The saturation underneath the ribs is seen to remain mostly constant or increase, as denoted by the negative desaturation rate, until the 15-16 minute mark, when the ribs begin to have a similar desaturation rate to that seen in the channels. This overlap of desaturation rates ends starting at the 30 minute mark, when the ribs undergo rapid desaturation.

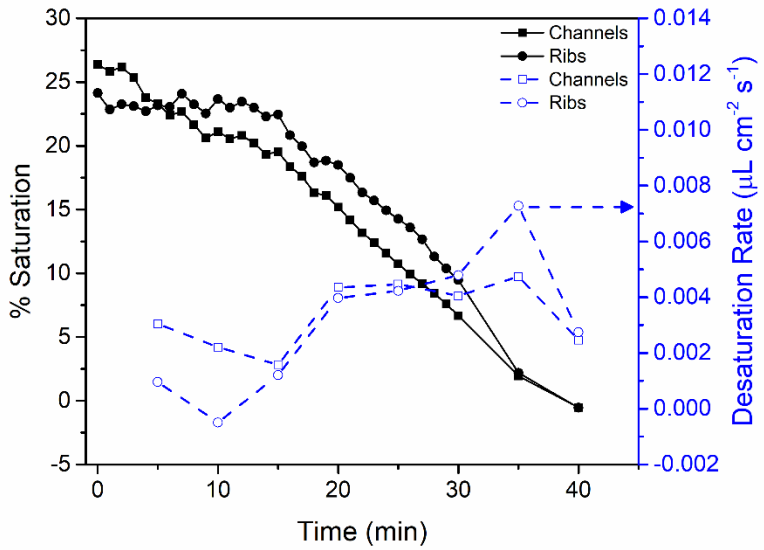

Figure 26. Temporal saturation profile and transient desaturation rate for both the channel and rib domains.

Next, the individual channels and ribs were separated to investigate if there was a spatial saturation difference from inlet to outlet across the GDL. The reader is referred back to Figure 24-A to reference the naming convention for the individual ribs and channels in the cell. Figure 27 displays the temporal saturation profiles and desaturation rates for each rib and gas flow channel. From Figure 27-A, it is seen that there is a high level of heterogeneity between each of the channels. Looking at the transient desaturation rates in Figure 27-C, it is seen that all of the channels have unique desaturation profiles, with peak desaturation rates occurring at different time points throughout the experiment. While it makes sense that channel one is the first to peak at the beginning of the experiment, as it is located directly next to the inlet, the next peak occurs under channel 5 from 15-20 minutes, which is located next to the outlet. The final peak occurs in the middle of the overall GDL domain under channel 3 from 30-35 minutes. Also interesting is that for the first 15 minutes, the desaturation rate underneath channel 2 and 3 is close to zero. Looking to the results underneath the ribs, the same extent of heterogeneity is not observed. First, all four ribs display a lag time before significant desaturation occurs, generally between the 12 and 16 minute mark. However, it is seen that in rib 3 the saturation actually slightly increases from the 4 to 12 minute mark. It is also underneath rib 3 that the highest overall desaturation rate is observed from the 30 minute mark until the end of the test.

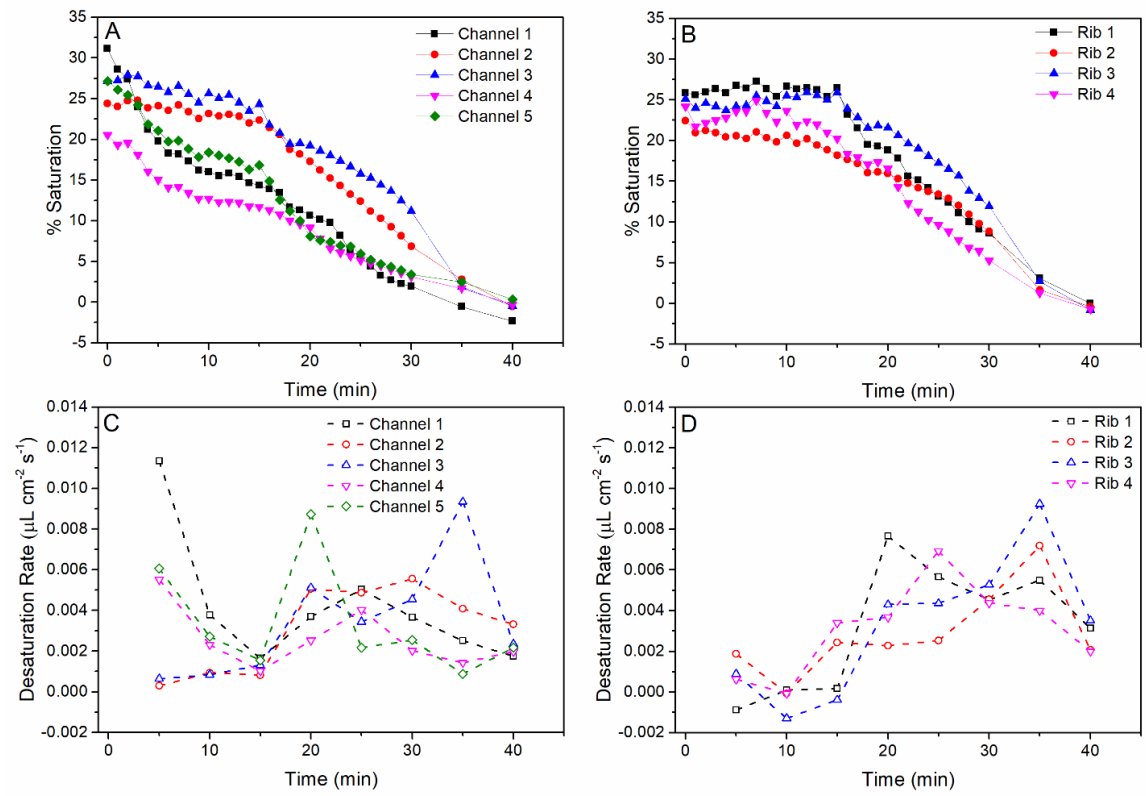

Figure 27. Temporal saturation profiles A) underneath each individual gas flow channel, where channel 1 is the inlet and channel 5 is the outlet, and B) underneath each individual rib. Transient desaturation rates presented as 5-minute averages C) for each channel.

These segmented temporal saturation profiles and transient desaturation rates demonstrate the large scale of heterogeneity present throughout the entire GDL during the overall desaturation process. This is in stark contrast to the investigation of the overall domain, where the process is seen to be mostly steady and consistent.

4.3.3 Desaturation Quantification: Channel and Rib Segmentation

Next, the individual channels and ribs were segmented, with geometries and naming conventions displayed in Figure 24-B. The saturation measurements for each segment were translated onto a matrix based on the spatial coordinates of each segment

and are presented as surface plots. This plot allows each segment to be visualized at the same spatial scale (e.g. channel width or rib width) as occurs in the actual experimental setup. Figure 28 presents the spatial saturation plots at selected time points throughout the desaturation process. From these selected saturation plots, it can be seen that the highest concentration of water was consistently found underneath the third bend throughout the test. Between the first and tenth minute of airflow, the saturation only slightly decreases in this location by 0.9%. Figure 27-C shows that channels 1, 4, and 5 had the highest desaturation rates at the start of the test. Comparing Figure 28-A and B, it is seen that the majority of the desaturation in channel 4 occurred at the end of the channel, closest to bend 4. Similarly, in channels 2 and 3 it is seen that the middle and top portions of the channel (relative to the figure) desaturate faster than the lower areas. Taken together, this shows a preference of desaturation to the upper region of the overall GDL domain. This, along with the behavior observed in bend 3, suggests that the gas flow was potentially bypassing underneath the ribs and following a more direct path from the inlet to outlet via the in-plane flow paths available in the porous GDL.

The heterogeneous nature of the desaturation is best observed by comparing Figure 28-A and C. Specifically, it is seen that although the regions centered around bend 1 and bend 4 started at a relatively high saturation, they both underwent faster desaturation then areas with lower initial saturation such as channel 3 and 4 and their neighboring ribs. Figure 28-D shows that after 30 minutes of airflow the majority of the domain has completely desaturated, except for the region around the third bend and the

neighboring sections of ribs 2 and 3. By 40 minutes, the entire domain is at 0% saturation.

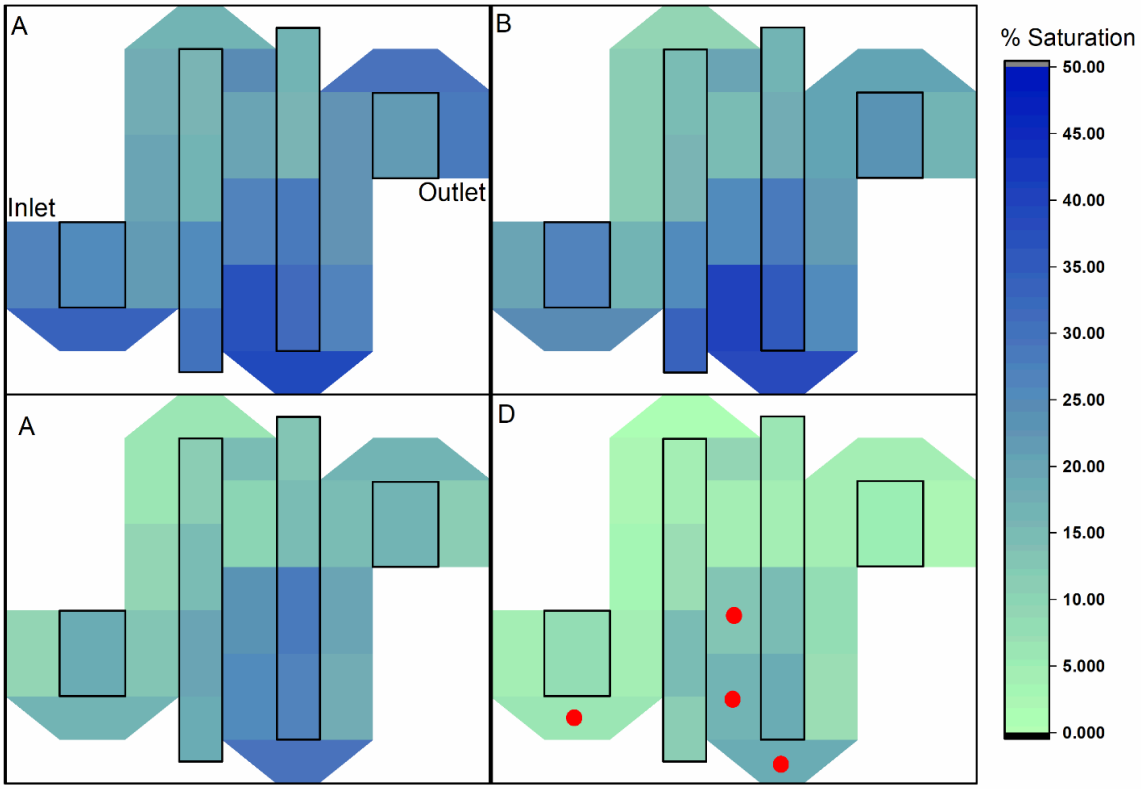

Figure 28. Spatial saturation plots showing the segmented saturation profiles after A) 1 min of dry air flow, B) 10 minutes of dry airflow, C) 20 minutes of dry airflow, and D) 30 minutes of dry airflow. (Color figure online)

In this approach, it is seen that both neighboring segments, as well as regions with similar geometries, display high levels of variance in their desaturation profiles. This factor is further illustrated by Figure 29, where the temporal saturation profiles of four selected segments are presented. For reference, these four segments are marked in Figure 28-D by red dots. Figure 29-A displays saturation profiles of two neighboring segments in channel 3. There is initially a 7 % magnitude difference between the saturation values between the two regions. From here, the saturation for both segments stays mostly

constant for the first 20 minutes of the experiment. At this point channel 3-γ (C3-γ) undergoes rapid desaturation down to approximately the same value as seen in channel 3-δ (C3-δ). From here the desaturation of the two segments follows a similar path until 35 minutes where a difference of 5.5% saturation appears. A divergence is also found between the saturation profiles of bend 1 (B1) and bend 3 (B3). While bend 1 almost immediately begins to desaturate, bend 3 briefly increases in saturation for the first 5-10 minutes, until its constant desaturation begins, rapidly accelerating around 25 minutes.

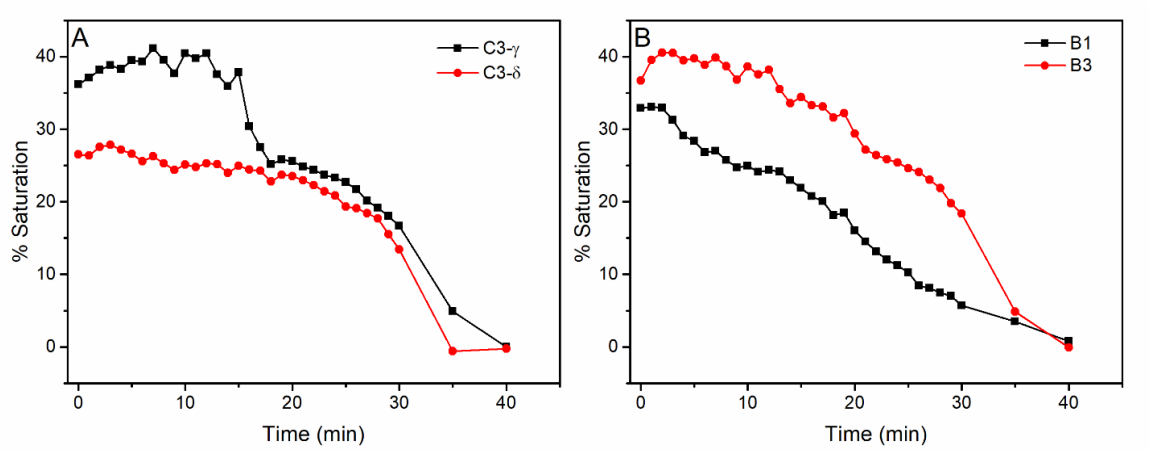

Figure 29. Temporal saturation profiles for select segments in Figure 28. A) Channel 3-γ and channel 3-δ and B) bend 1 and bend 3. These results indicate different rates of desaturation that are not dependent on flow field geometry or initial conditions.

These selected saturation profiles demonstrate that there is no representative or average desaturation path that can be applied between the different segments. Even between segments that have similar geometries, heterogeneous behavior is consistently observed, pointing to the impact that local material structures, such as permeability, pore size, and initial saturation have on desaturation.

4.4 Discussion

This section focuses on comparisons to other studies including published desaturation rates and pore network models. The potential applications where this data set could be used for future validation and key findings from this study are also summarized.

4.4.1 Analysis of Overall Desaturation Rate

As discussed in section 3.1, the overall desaturation rate for the entire GDL domain was found to be 0.0030 μL cm^{-2} s^{-1}. While this value is lower than that reported by other recent studies, this difference can be explained by the experimental conditions used in each study. Zenyuk et al. [33] reported a value of 0.09 μL cm^{-2} s^{-1}. However, their experiment was at a flowrate of 600 N ml min^{-1}, which is an order of magnitude higher than that used in this study, 50 N ml min^{-1}, and it has been shown by previous work that there is a convective component to GDL desaturation [34]. Multiple studies [37, 38] have also shown that increasing the flowrate results in an increase of the evaporation rate. Additionally, the GDL investigated in that study had PTFE treatment, which has been shown to alter both the location of saturating water as well as the rate of desaturation [34]. Similarly, Lal et al. [32] determined an evaporation rate of 0.9 μL cm^{-2} s^{-1}; however, their experiment was run at 60°C with a gas velocity of 6 m s^{-1}, while this study was performed at 22°C and 0.8 m s^{-1}. In addition to the effects due to a larger flowrate and PTFE treatment, an increased temperature has an exponential impact on an evaporation rate [37]. Finally, both of those studies investigated a single channel over a much smaller domain, 3.2 mm diameter in the investigation by Zenyuk et al. [33], and 1 mm x 1 mm

for Lal et al. [32], compared to the 5 serpentine channels within a region of interest of 10 mm in diameter in this study. Taking all of these factors into consideration, the difference between the calculated overall desaturation rates makes qualitative sense.

4.4.2 Analysis of Segmented Results

As reviewed in section 4.1, the typical pore network modeling domain size is currently restricted by computational power, and most models are limited to a unit cell approximately the width of one channel and rib (1-2mm) [24-26]. Results from this study show that as computational capabilities expand, both initial conditions and flow field geometry will need to be taken into consideration in order to fully capture and model the transient saturation behavior. Although the bulk desaturation of a GDL may appear to be a largely linear process, as seen in Figure 25-A, when the flow field is spatially segmented into ribs and channels, heterogeneous desaturation rates emerge, as seen in Figure 27, where both the saturation values as well as the desaturation rates are seen to vary. These variations occur between the channel and rib zones, and also on a channel-to-channel and rib-to-rib basis. For example, between channel 3 and channel 4 there is a nearly two-fold difference in the desaturation rate from 15 to 20 minutes, 0.005 $\mu L\ cm^{-2}\ s^{-1}$ versus 0.003 $\mu L\ cm^{-2}\ s^{-1}$. Additionally, from the spatial saturation maps in Figure 28, it is seen that large saturation gradients can exist across the domain. As seen in Figure 29-A, there is a 7% difference in magnitude of the initial saturation between two neighboring segments of the same channel, and their resulting desaturation profiles are different. Although the initial saturation in this study was not generated by an active PEMFC, previous active fuel cell results show that the current distribution is not homogenous

throughout the catalyst layer [39], which would lead to heterogeneous water production across the domain. Depending on the material, this could lead to varying initial conditions and removal characteristics within the porous media. In a recent study by García-Salaberri et al. [23], it was found that a representative element volume could not be found for a GDL due to the relative thinness of the GDL in relation to the average pore size. Similarly, this study has shown that both desaturation rates and overall saturation can vary across the whole domain. As seen in Figure 25 and discussed in section 4.3.1, there was a two-fold difference between transient desaturation rates, thus an overall desaturation rate may not be appropriate when describing this media. As such, as computational power expands PNMs will need to accordingly expand to capture more of the domain in order to further investigate the cause for these observed heterogeneities.

These results also highlight the potential for intelligently engineered materials, which have the potential to replace the anisotropic carbon fiber paper commonly used as the substrate for GDLs. Examples of such designed materials include electrospun GDLs and metallic GDLs. As these more isotropic GDLs are further developed, it should be investigated whether or not GDL homogeneity affects the spatial distribution of percent saturation or transient desaturation rates.

4.5 Conclusion

The 4-D imaging of the desaturation of an initially flooded GDL by a serpentine flow channel was performed for the first time using synchrotron X-ray CT. Analysis of the overall domain presented a desaturation profile that was comprised of two largely

linear regions, with rates ranging between 0.0018 ± 0.0002 μL cm^{-2} s^{-1} to 0.0042 ± 0.0004 μL cm^{-2} s^{-1} and an overall rate of 0.0030 ± 0.0013 μL cm^{-2} s^{-1}. As the domain was segmented down to the scale of individual ribs and channels, a heterogeneous distribution of both local saturations and desaturation rates emerged with overall desaturation rates of 0.0034 ± 0.0012 μL cm^{-2} s^{-1} and 0.0031 ± 0.0025 μL cm^{-2} s^{-1} for the channel and rib domain, respectively. Fully segmented results showed that this heterogeneous behavior was still observed between both neighboring regions and similar geometries. These temporal and spatial gradients show that the initial conditions, intrinsic anisotropy of the material, as well as the local and global geometry of the gas flow field all play a key role in determining the local desaturation behavior of a GDL. Taken together, these results indicate that as computational capabilities expand, larger computational domains will be necessary to accurately represent the multiphase transport within this thin porous media.

Acknowledgements

LFZ and RA acknowledge the support from their respective universities, the University of Saskatchewan and Montana State University. LFZ also acknowledge the financial support from Natural Sciences and Engineering Research Council of Canada (NSERC). This collaboration was also supported under NSF Award number 1444198. Any opinions, findings, and conclusions or recommendations expressed in this material are those of the authors and do not necessarily reflect the views of the National Science Foundation. RA and LB also acknowledge the support from the Center for Biofilm Engineering from Montana State University for access to imaging software. Research described in this

paper was performed at the BMIT facility at the Canadian Light Source, which is supported by the Canada Foundation for Innovation, Natural Sciences and Engineering Research Council of Canada, the University of Saskatchewan, the Government of Saskatchewan, Western Economic Diversification Canada, the National Research Council Canada, and the Canadian Institutes of Health Research.

References

1. Fuel Cell Technologies Office Multi-Year Research, Development, and Demonstration Plan. 2016, Department of Energy. p. 3.4 1-58.

2. Cindrella, L., et al., Gas diffusion layer for proton exchange membrane fuel cells—A review. Journal of Power Sources, 2009. 194(1): p. 146-160.

3. Bear, J., Dynamics of fluids in porous media. 2013: Courier Corporation.

4. Qin, C.Z. and S.M. Hassanizadeh, A new approach to modelling water flooding in a polymer electrolyte fuel cell. International Journal of Hydrogen Energy, 2015. 40(8): p. 3348-3358.

5. Yousfi-Steiner, N., et al., A review on PEM voltage degradation associated with water management: Impacts, influent factors and characterization. Journal of Power Sources, 2008. 183(1): p. 260-274.

6. Ous, T. and C. Arcoumanis, Degradation aspects of water formation and transport in Proton Exchange Membrane Fuel Cell: A review. Journal of Power Sources, 2013. 240: p. 558-582.

7. Park, J., et al., A review of the gas diffusion layer in proton exchange membrane fuel cells: Durability and degradation. Applied Energy, 2015. 155: p. 866-880.

8. Lapicque, F., et al., A critical review on gas diffusion micro and macroporous layers degradations for improved membrane fuel cell durability. Journal of Power Sources, 2016. 336: p. 40-53.

9. Park, S., J.-W. Lee, and B.N. Popov, A review of gas diffusion layer in PEM fuel cells: Materials and designs. International Journal of Hydrogen Energy, 2012. 37(7): p. 5850-5865.

10. Alink, R., et al., The influence of porous transport layer modifications on the water management in polymer electrolyte membrane fuel cells. Journal of Power Sources, 2013. 233: p. 358-368.

11. Chen, H.-H. and M.-H. Chang, Effect of cathode microporous layer composition on proton exchange membrane fuel cell performance under different air inlet relative humidity. Journal of Power Sources, 2013. 232: p. 306-309.

12. Li, A. and S.H. Chan, Understanding the role of cathode structure and property on water management and electrochemical performance of a PEM fuel cell. International Journal of Hydrogen Energy, 2013. 38(27): p. 11988-11995.

13. Wang, Y., et al., Double-layer gas diffusion media for improved water management in polymer electrolyte membrane fuel cells. Journal of Power Sources, 2015. 292: p. 39-48.

14. Wang, Z., et al., Improvement of PEMFC water management by employing water transport plate as bipolar plate. International Journal of Hydrogen Energy, 2017. 42(34): p. 21922-21929.

15. Chevalier, S., et al., Novel electrospun gas diffusion layers for polymer electrolyte membrane fuel cells: Part II. In operando synchrotron imaging for microscale liquid water transport characterization. Journal of Power Sources, 2017. 352(Supplement C): p. 281-290.

16. Lim, B.H., et al., Effects of flow field design on water management and reactant distribution in PEMFC: a review. Ionics, 2016. 22(3): p. 301-316.

17. Trabold, T.A., Minichannels in Polymer Electrolyte Membrane Fuel Cells. Heat Transfer Engineering, 2005. 26(3): p. 3-12.

18. Hussaini, I.S. and C.Y. Wang, Dynamic water management of polymer electrolyte membrane fuel cells using intermittent RH control. Journal of Power Sources, 2010. 195(12): p. 3822-3829.

19. Damour, C., et al., A novel non-linear model-based control strategy to improve PEMFC water management – The flatness-based approach. International Journal of Hydrogen Energy, 2015. 40(5): p. 2371-2376.

20. Battrell, L., et al., Quantifying Cathode Water Transport via Anode Relative Humidity Measurements in a Polymer Electrolyte Membrane Fuel Cell. Energies, 2017. 10(8): p. 16.

21. Wu, H.-W., A review of recent development: Transport and performance modeling of PEM fuel cells. Applied Energy, 2016. 165: p. 81-106.

22. Andersson, M., et al., A review of cell-scale multiphase flow modeling, including water management, in polymer electrolyte fuel cells. Applied Energy, 2016. 180: p. 757-778.

23. García-Salaberri, P.A., et al., Analysis of representative elementary volume and through-plane regional characteristics of carbon-fiber papers: diffusivity, permeability and electrical/thermal conductivity. International Journal of Heat and Mass Transfer, 2018. 127: p. 687-703.

24. Aghighi, M. and J. Gostick, Pore network modeling of phase change in PEM fuel cell fibrous cathode. Journal of Applied Electrochemistry, 2017. 47(12): p. 1323-1338.

25. Belgacem, N., M. Prat, and J. Pauchet, Coupled continuum and condensation–evaporation pore network model of the cathode in polymer-electrolyte fuel cell. International Journal of Hydrogen Energy, 2017. 42(12): p. 8150-8165.

26. Medici, E.F., et al., Understanding Water Transport in Polymer Electrolyte Fuel Cells Using Coupled Continuum and Pore-Network Models. Fuel Cells, 2016. 16(6): p. 725-733.

27. Bazylak, A., Liquid water visualization in PEM fuel cells: A review. International Journal of Hydrogen Energy, 2009. 34(9): p. 3845-3857.

28. Krüger, P., et al., Synchrotron X-ray tomography for investigations of water distribution in polymer electrolyte membrane fuel cells. Journal of Power Sources, 2011. 196(12): p. 5250-5255.

29. Lee, J., et al., Synchrotron Investigation of Microporous Layer Thickness on Liquid Water Distribution in a PEM Fuel Cell. Journal of the Electrochemical Society, 2015. 162(7): p. F669-F676.

30. Arlt, T., et al., Influence of artificially aged gas diffusion layers on the water management of polymer electrolyte membrane fuel cells analyzed with in-operando synchrotron imaging. Energy, 2017. 118: p. 502-511.

31. Muirhead, D., et al., Liquid water saturation and oxygen transport resistance in polymer electrolyte membrane fuel cell gas diffusion layers. Electrochimica Acta, 2018. 274: p. 250-265.

32. Lal, S., et al., Determination of Water Evaporation Rates in Gas Diffusion Layers of Fuel Cells. Journal of The Electrochemical Society, 2018. 165(9): p. F652-F661.

33. Zenyuk, I.V., et al., Investigating evaporation in gas diffusion layers for fuel cells with X-ray computed tomography. The Journal of Physical Chemistry C, 2016. 120(50): p. 28701-28711.

34. Battrell, L., et al., Transient, spatially resolved desaturation of gas diffusion layers measured via synchrotron visualization. International Journal of Hydrogen Energy, 2018. 43(24): p. 11234-11243.

35. Wysokinski, T.W., et al., Beamlines of the biomedical imaging and therapy facility at the Canadian light source—Part 1. Nuclear Instruments and Methods in Physics Research Section A: Accelerators, Spectrometers, Detectors and Associated Equipment, 2007. 582(1): p. 73-76.

36. Rasband, W.S., ImageJ. 1997-2016, U.S. National Institutes of Health: Bethesda, Maryland, USA.

37. Hisatake, K., et al., Experimental and theoretical study of evaporation of water in a vessel. Journal of Applied Physics, 1995. 77(12): p. 6664-6674.

38. Lyulin, Y.V. and O.A. Kabov, Measurement of the evaporation mass flow rate in a horizontal liquid layer partly opened into flowing gas. Technical Physics Letters, 2013. 39(9): p. 795-797.

39. Herrera, O.E., D.P. Wilkinson, and W. Mérida, Anode and cathode overpotentials and temperature profiles in a PEMFC. Journal of Power Sources, 2012. 198: p. 132-142.

CHAPTER FIVE

CONCLUSIONS AND RECOMMENDATIONS

5.1 Conclusions

The work comprising this thesis has investigated water transport and removal from the GDL of a fuel cell at both the macroscale and microscale. Experimental techniques used included the analysis of pressure drop signals from active fuel cell testing (Chapter 2) and Synchrotron X-ray CT to investigate GDL desaturation rates and behaviors (Chapters 3 and 4). Findings and conclusions from these studies are summarized below.

The developed diagnostic test effectively extends the traditional Anode Water Removal (AWR) technique beyond a purely qualitative test. The traditional AWR test is able to identify if a PEM fuel cell is operating below its optimal voltage due to cathode flooding by introducing a dry anode stream with a step-wise increase in the flowrate. By first collecting anode pressure drop data at set relative humidities and flowrates in a non-active fuel cell, an algorithm was developed to solve for the unknown anode relative humidity during active cell testing. The algorithm works by guessing a humidity value and then calculating the resulting gas properties such as density and total flowrate, and then calculating what the overall pressure drop is. The difference between the calculated pressure drop and the experimental pressure drop is minimized, resulting in a predicted relative humidity value. This relative humidity data is then used to close the water balance of the cell, which allows for the calculation of the overall net cell water flux.

When the net cell water flux is negative, there is more water being removed from the cell than is being produced by the reaction, so there must be an additional source of water within the cell. When this is observed along with an increase in voltage, it indicates that the sub-optimal performance is due to flooding on the cathode side, which accounts for the additional source term, either within the GDL or between the GDL and catalyst layer. This test was used to analyze three different GDLs with varying intrinsic water management capabilities, and results showed that the amount of water removed corresponded to the initial performance and expected water management capabilities. The strength of this approach is that it is fast, non-intrusive, and should be applicable to a variety of fuel cell testing setups. Additionally, it is able to provide information about water transport from an active fuel cell, as opposed to the more common *ex-situ* techniques.

Next, the desaturation of the GDL was investigated and visualized at the microscale using synchrotron X-ray computed tomography (X-ray CT). An *ex-situ* acrylic test cell, with a single serpentine channel with four bends, was designed to minimize scan time while maximizing phase contrast and the region of interest in order to image the largest domain possible as quickly as possible. Two different GDL samples, one with a hydrophobic PTFE (5% by weight) treatment and one without, were initially saturated with liquid water and then desaturated at constant air flow rates. The flow conditions were varied with both dry and 100% humidified air to separate the contributions of evaporation and convection in the desaturation of the GDLs. Slow, high-fidelity scans taken at the beginning and end of the experiment were used to quantify

initial saturation. Rapid on-the-fly scans were taken every 1.5 minutes to identify the desaturation time to then calculate overall desaturation rates. Visualization results qualitatively showed that both evaporation and convection play a role in GDL desaturation, but that evaporation is both the dominant component and required for full desaturation; a singularly convective component is unable to fully desaturate a GDL. This study also showed that the hydrophobic treatment applied to GDLs changes the location of where saturating water accumulates to be on the surface of the GDL, with minimal penetration into the pore space. Additionally, the hydrophobic treatment changed where the irremovable water to be underneath the channel ribs, whereas for the GDL without PTFE the water was dispersed throughout the entire porous layer. Finally, these results showed that the GDL with the PTFE treatment desaturated almost four times faster than the GDL without PTFE.

Next, the synchrotron X-ray CT technique was extended to quantify transient desaturation rates and saturation profiles of the GDL, again using an *ex-situ* acrylic test cell with a single serpentine channel with four bends. The overall domain was successfully segmented down to investigate the spatial distribution of both local percent saturation and transient desaturation rates. Looking at the transient desaturation of the overall domain, two largely linear regions were identified, with an initial desaturation rate of 0.0018 ± 0.0002 μL cm^{-2} s^{-1}, which then increased to 0.0042 ± 0.0004 μL cm^{-2} s^{-1}, for an overall rate of 0.0030 ± 0.0013 μL cm^{-2} s^{-1}. When the domain was segmented to separate the areas underneath the ribs and channels, rates of 0.0031 ± 0.0025 μL cm^{-2} s^{-1} and 0.0034 ± 0.0012 μL cm^{-2} s^{-1} where found. As the channels and ribs were further

segmented, the heterogeneity continued to expand including between neighboring regions and similar geometries. These results showed that the desaturation of the domain was a largely heterogeneous process that depends on initial saturation, flow field geometry, and the anisotropic nature of the material. Currently, the general domain size investigated by modeling studies is on average 1-2 mm x 1-2 mm, which encompasses one rib-channel unit. These results show that as computational capabilities increase, future models will have to expand their investigated domain in order to fully capture the observed heterogeneous behavior. Additionally, these results underline the potential for intelligently engineered materials, which are more isotropic than the commonly used carbon fiber paper substrates, to allow for more homogenous behavior throughout the entire domain.

5.2 Recommendations

The information provided by the diagnostic test tells how much water is being removed by the anode. By combining this data with the known water production rate and the amounts of water being brought in by the two gas streams based on their set humidities, a full water balance could be formulated. The diagnostic test could then be extended to also calculate the bulk diffusivity of the MEA for water transport from the cathode to the anode of an active fuel cell, information that previously has only been measured in *ex-situ* non-active setups. This *in-situ* information would be valuable for the potential modification of macro-level fuel cell models, such as the ones used in control schemes, which to date generally use *ex-situ* measurements to describe the system.

Future visualization experiments should focus on including two of the operating conditions used in the active fuel cell that were previously neglected, specifically cell temperature, gas pressure, and compression pressure. New designs of the test cell should incorporate external heating and some sort of external compression so that the environment within the test cell is more similar to actual fuel cell operating conditions of 75°C with 80-100 kPa external compression. Previously, external heating was attempted using heat tape, but due to the poor thermal conductivity of acrylic, the region of interest could not be heated to realistic fuel cell conditions before the area with the heat tape began to melt and deform. To address this, a channel should be added underneath the test area through which heated water could be flowed. By flowing heated water close to the region-of-interest, it should be possible to heat that area to fuel cell temperature without damaging or altering the acrylic. Previously, external compression was not achieved due to the brittle nature of the acrylic and using screws that could only be hand tightened. To address these issues, the acrylic cell should be fabricated with fine metal threading, which will make it possible to be better control the compression pressure and alleviate the issue of the threading wearing down or cracking. Additionally, screws that can be tightened by a torque wrench should be used so that an appropriate amount of compression can be achieved.

Next, a computational fluid dynamics (CFD) approach should be used to start corroborating results from both the macroscale and microscale investigations. First, a model of the setup used for the visualization results could be used to identify if the heterogeneous initial saturation is causing unexpected flow patterns, channel bypass, or

velocity gradients throughout the GDL, which could help to explain the heterogeneous desaturation rates observed in the experiment. Additionally, a model of the full active fuel cell setup could be used to verify the net cell water flux calculated from the experimental results. Then, if computationally feasible, heterogeneous saturation gradients based on results from the visualization experiments could be seeded as initial conditions to see if the proposed transport mechanisms describing the water removal are physically possible. Current image segmentation and analysis is being completed by lumping the GDL and water together, and seeing how this bulk value changes over time, with the assumption that any reduction in threshold area is due to water removal. In order to generate 3-D reconstructions of the water within the GDL, which is necessary to seed as an initial condition, a more rigorous segmentation method is necessary. Lambric et al [1] have published a segmentation and reconstruction algorithm that was able to separate GDL fibers, void space, and water. This algorithm could be applied to the data sets that have been collected in order to reconstruct the actual water volume in each scan, which could better elucidate the transport occurring and to identify the locations where water is being removed and accumulating.

Once these three initial task are completed, there are several avenues for how this work could continue on a more long-term scale. It was seen from the synchrotron work in Chapter 4 that saturation distributions and desaturation rates were heterogeneous across the domain. Recently, a method to fabricate metal GDLs has been developed that would result in a more controlled and isotropic material. It would be interesting to see if a more uniform material also displayed the heterogeneous behavior observed with the carbon

fiber paper substrate. In order to investigate this, modifications would have to be made to the acrylic cell to shrink the domain size, since the attenuation of the metal GDL would be much higher than that of the carbon fiber paper. The initial substance being considered is silver; however the attenuation of 1 mm of silver at 70 keV is ~98.7%, which is much too high for any suitable imaging. However, if a different metal could be used, such as titanium that has an attenuation of 23.3%, similar experiments to those in Chapters 3 and 4 could be ran to investigate the desaturation properties of a more isotropic material. Similarly, these materials could also be tested using the diagnostic protocol described in Chapter 2 to determine their intrinsic water management capabilities to be compared to more traditional materials. All of these steps could also be applied to electrospun GDLs, which similarly can be fabricated in a manner to produce a more homogenous domain.

The next improvement for the visualization studies would be to redesign the setup to incorporate an active fuel cell. To do so would require the intelligent engineering and design of the fuel cell architecture to maintain the capability for 4-D imaging, as multiple groups have already imaged various processes related to water management in the 2-D setting. Key to such a design would be moving all flow architecture outside of the viewing window with a specialized setup designed to allow for the rotation of the sample without introducing any supporting architecture into the viewing window. The necessary addition of graphite to the sample cell would require a higher X-ray flux in order to maintain the phase contrast required for quantification, so all of the beam and sample distance calibration would have to be repeated on the higher energy 05ID-2 beamline.

Finally, recent work has showed that coupled continuum-pore network models are appropriate in describing the overall water transport through GDLs [2]. If the reconstruction of the water volume, described above, was then imported into such a model, an investigation of the desaturation of the GDL with relevant flow geometries above could be completed. It should be noted that modeling the entire domain investigated in Chapters 3 and 4 would require extensive computational capabilities, and thus would require access to high-end supercomputing to even be feasible. As such, a reduction of the domain size may be necessary to make the problem more computationally reasonable.

References

1. Lamibrac, A., et al., Characterization of Liquid Water Saturation in Gas Diffusion Layers by X-Ray Tomographic Microscopy. Journal of The Electrochemical Society, 2016. 163(3): p. F202-F209.

2. Medici, E.F., et al., Understanding Water Transport in Polymer Electrolyte Fuel Cells Using Coupled Continuum and Pore-Network Models. Fuel Cells, 2016. 16(6): p. 725-733.

CUMULATIVE REFERENCES CITED

1. Fuel Cell Technologies Office Multi-Year Research, Development, and Demonstration Plan. 2016, Department of Energy. p. 3.4 1-58.

2. Light Sources of the World. 2018, Lightsource.org: https://lightsources.org/lightsources-of-the-world/.

3. Aghighi, M. and J. Gostick, Pore network modeling of phase change in PEM fuel cell fibrous cathode. Journal of Applied Electrochemistry, 2017. 47(12): p. 1323-1338.

4. Aiyejina, A. and M.K.S. Sastry, PEMFC Flow Channel Geometry Optimization: A Review. Journal of Fuel Cell Science and Technology, 2011. 9(1): p. 011011-011011-24.

5. Alink, R., et al., The influence of porous transport layer modifications on the water management in polymer electrolyte membrane fuel cells. Journal of Power Sources, 2013. 233: p. 358-368.

6. Anderson, R., et al., Anode water removal and cathode gas diffusion layer flooding in a proton exchange membrane fuel cell. International Journal of Hydrogen Energy, 2012. 37(21): p. 16093-16103.

7. Andersson, M., et al., A review of cell-scale multiphase flow modeling, including water management, in polymer electrolyte fuel cells. Applied Energy, 2016. 180: p. 757-778.

8. Arlt, T., et al., Influence of artificially aged gas diffusion layers on the water management of polymer electrolyte membrane fuel cells analyzed with in-operando synchrotron imaging. Energy, 2017. 118: p. 502-511.

9. Banerjee, R., et al., Transient Liquid Water Distributions in Polymer Electrolyte Membrane Fuel Cell Gas Diffusion Layers Observed through In-Operando Synchrotron X-ray Radiography. Journal of The Electrochemical Society, 2017. 164(2): p. F154-F162.

10. Banerjee, R., et al., Heterogeneous porosity distributions of polymer electrolyte membrane fuel cell gas diffusion layer materials with rib-channel compression. International Journal of Hydrogen Energy, 2016. 41(33): p. 14885-14896.

11. Banerjee, R. and S.G. Kandlikar, Two-phase flow and thermal transients in proton exchange membrane fuel cells – A critical review. International Journal of Hydrogen Energy, 2015. 40(10): p. 3990-4010.

12. Barbir, F., PEM fuel cells: theory and practice. 2012: Academic Press.

13. Battrell, L., et al., Investigation of Water Transport Within a Proton Exchange Membrane Fuel Cell by Diffusion Layer Saturation Analysis. 2016(50244): p. V001T05A002.

14. Battrell, L., et al., Quantifying Cathode Water Transport via Anode Relative Humidity Measurements in a Polymer Electrolyte Membrane Fuel Cell. Energies, 2017. 10(8): p. 16.

15. Battrell, L., et al., Transient, spatially resolved desaturation of gas diffusion layers measured via synchrotron visualization. International Journal of Hydrogen Energy, 2018. 43(24): p. 11234-11243.

16. Bazylak, A., Liquid water visualization in PEM fuel cells: A review. International Journal of Hydrogen Energy, 2009. 34(9): p. 3845-3857.

17. Bear, J., Dynamics of fluids in porous media. 2013: Courier Corporation.

18. Belgacem, N., M. Prat, and J. Pauchet, Coupled continuum and condensation–evaporation pore network model of the cathode in polymer-electrolyte fuel cell. International Journal of Hydrogen Energy, 2017. 42(12): p. 8150-8165.

19. Berning, T., M. Odgaard, and S.K. Kær, A study of multi-phase flow through the cathode side of an interdigitated flow field using a multi-fluid model. Journal of Power Sources, 2010. 195(15): p. 4842-4852.

20. Cao, T.-F., et al., Numerical investigation of the coupled water and thermal management in PEM fuel cell. Applied Energy, 2013. 112: p. 1115-1125.

21. Chen, H.-H. and M.-H. Chang, Effect of cathode microporous layer composition on proton exchange membrane fuel cell performance under different air inlet relative humidity. Journal of Power Sources, 2013. 232: p. 306-309.

22. Chevalier, S., et al., Novel electrospun gas diffusion layers for polymer electrolyte membrane fuel cells: Part II. In operando synchrotron imaging for microscale liquid water transport characterization. Journal of Power Sources, 2017. 352(Supplement C): p. 281-290.

23. Chevalier, S., et al., Novel electrospun gas diffusion layers for polymer electrolyte membrane fuel cells: Part I. Fabrication, morphological characterization, and in situ performance. Journal of Power Sources, 2017. 352: p. 272-280.

24. Chevalier, S., et al., In operando measurements of liquid water saturation distributions and effective diffusivities of polymer electrolyte membrane fuel cell gas diffusion layers. Electrochimica Acta, 2016. 210: p. 792-803.

25. Cho, K.T. and M.M. Mench, Fundamental characterization of evaporative water removal from fuel cell diffusion media. Journal of Power Sources, 2010. 195(12): p. 3858-3869.

26. Cindrella, L., et al., Gas diffusion layer for proton exchange membrane fuel cells—A review. Journal of Power Sources, 2009. 194(1): p. 146-160.

27. Damour, C., et al., A novel non-linear model-based control strategy to improve PEMFC water management – The flatness-based approach. International Journal of Hydrogen Energy, 2015. 40(5): p. 2371-2376.

28. Deevanhxay, P., et al., Effect of liquid water distribution in gas diffusion media with and without microporous layer on PEM fuel cell performance. Electrochemistry Communications, 2013. 34: p. 239-241.

29. Ding, Y., X. Bi, and D.P. Wilkinson, 3D simulations of the impact of two-phase flow on PEM fuel cell performance. Chemical Engineering Science, 2013. 100: p. 445-455.

30. Fazeli, M., et al., Pore network modeling to explore the effects of compression on multiphase transport in polymer electrolyte membrane fuel cell gas diffusion layers. Journal of Power Sources, 2016. 335: p. 162-171.

31. García-Salaberri, P.A., et al., Effective diffusivity in partially-saturated carbon-fiber gas diffusion layers: Effect of local saturation and application to macroscopic continuum models. Journal of Power Sources, 2015. 296: p. 440-453.

32. García-Salaberri, P.A., et al., On the limitations of volume-averaged descriptions of gas diffusion layers in the modeling of polymer electrolyte fuel cells. ECS Transactions, 2017. 80(8): p. 133-143.

33. García-Salaberri, P.A., et al., Analysis of representative elementary volume and through-plane regional characteristics of carbon-fiber papers: diffusivity, permeability and electrical/thermal conductivity. International Journal of Heat and Mass Transfer, 2018. 127: p. 687-703.

34. Gostick, J.T., et al., In-plane and through-plane gas permeability of carbon fiber electrode backing layers. Journal of Power Sources, 2006. 162(1): p. 228-238.

35. Grötsch, M. and M. Mangold, A two-phase PEMFC model for process control purposes. Chemical Engineering Science, 2008. 63(2): p. 434-447.

36. Gurau, V., et al., Characterization of transport properties in gas diffusion layers for proton exchange membrane fuel cells: 2. Absolute permeability. Journal of Power Sources, 2007. 165(2): p. 793-802.

37. Hartnig, C., et al., High-resolution in-plane investigation of the water evolution and transport in PEM fuel cells. Journal of Power Sources, 2009. 188(2): p. 468-474.

38. Herrera, O.E., D.P. Wilkinson, and W. Mérida, Anode and cathode overpotentials and temperature profiles in a PEMFC. Journal of Power Sources, 2012. 198: p. 132-142.

39. Hisatake, K., et al., Experimental and theoretical study of evaporation of water in a vessel. Journal of Applied Physics, 1995. 77(12): p. 6664-6674.

40. Hussaini, I.S. and C.Y. Wang, Visualization and quantification of cathode channel flooding in PEM fuel cells. Journal of Power Sources, 2009. 187(2): p. 444-451.

41. Hussaini, I.S. and C.Y. Wang, Dynamic water management of polymer electrolyte membrane fuel cells using intermittent RH control. Journal of Power Sources, 2010. 195(12): p. 3822-3829.

42. Iranzo, A., et al., Water build-up and evolution during the start-up of a PEMFC: Visualization by means of Neutron Imaging. International Journal of Hydrogen Energy, 2017. 42(19): p. 13839-13849.

43. Jiang, H., et al., Experimental study on dual recirculation of polymer electrolyte membrane fuel cell. International Journal of Hydrogen Energy, 2017. 42(29): p. 18551-18559.

44. Kalidindi, A.R., et al., A two-phase model for studying the role of microporous layer and catalyst layer interface on polymer electrolyte fuel cell performance. International Journal of Hydrogen Energy, 2013. 38(22): p. 9297-9309.

45. Kim, K.N., et al., Lattice Boltzmann simulation of liquid water transport in microporous and gas diffusion layers of polymer electrolyte membrane fuel cells. Journal of Power Sources, 2015. 278: p. 703-717.

46. Kim, M., et al., Effects of anode flooding on the performance degradation of polymer electrolyte membrane fuel cells. Journal of Power Sources, 2014. 266: p. 332-340.

47. Kirubakaran, A., S. Jain, and R.K. Nema, A review on fuel cell technologies and power electronic interface. Renewable and Sustainable Energy Reviews, 2009. 13(9): p. 2430-2440.

48. Krüger, P., et al., Synchrotron X-ray tomography for investigations of water distribution in polymer electrolyte membrane fuel cells. Journal of Power Sources, 2011. 196(12): p. 5250-5255.

49. Lal, S., et al., Determination of Water Evaporation Rates in Gas Diffusion Layers of Fuel Cells. Journal of The Electrochemical Society, 2018. 165(9): p. F652-F661.

50. Lamibrac, A., et al., Characterization of Liquid Water Saturation in Gas Diffusion Layers by X-Ray Tomographic Microscopy. Journal of The Electrochemical Society, 2016. 163(3): p. F202-F209.

51. Lapicque, F., et al., A critical review on gas diffusion micro and macroporous layers degradations for improved membrane fuel cell durability. Journal of Power Sources, 2016. 336: p. 40-53.

52. Lee, J., et al., Synchrotron Investigation of Microporous Layer Thickness on Liquid Water Distribution in a PEM Fuel Cell. Journal of the Electrochemical Society, 2015. 162(7): p. F669-F676.

53. Lemoine-Nava, R., et al., The gas diffusion layer in polymer electrolyte membrane fuel cells: A process model of the two-phase flow. International Journal of Hydrogen Energy, 2011. 36(2): p. 1637-1653.

54. Li, A. and S.H. Chan, Understanding the role of cathode structure and property on water management and electrochemical performance of a PEM fuel cell. International Journal of Hydrogen Energy, 2013. 38(27): p. 11988-11995.

55. Li, H., et al., A review of water flooding issues in the proton exchange membrane fuel cell. Journal of Power Sources, 2008. 178(1): p. 103-117.

56. Lim, B.H., et al., Effects of flow field design on water management and reactant distribution in PEMFC: a review. Ionics, 2016. 22(3): p. 301-316.

57. Lyulin, Y.V. and O.A. Kabov, Measurement of the evaporation mass flow rate in a horizontal liquid layer partly opened into flowing gas. Technical Physics Letters, 2013. 39(9): p. 795-797.

58. Manso, A.P., et al., Influence of geometric parameters of the flow fields on the performance of a PEM fuel cell. A review. International Journal of Hydrogen Energy, 2012. 37(20): p. 15256-15287.

59. Medici, E.F., et al., Understanding Water Transport in Polymer Electrolyte Fuel Cells Using Coupled Continuum and Pore-Network Models. Fuel Cells, 2016. 16(6): p. 725-733.

60. Meng, H., B. Han, and B. Ruan, Numerical modeling of liquid water transport inside and across membrane in PEM fuel cells. Asia-Pacific Journal of Chemical Engineering, 2013. 8(1): p. 104-114.

61. Molaeimanesh, G.R. and M.H. Akbari, A three-dimensional pore-scale model of the cathode electrode in polymer-electrolyte membrane fuel cell by lattice Boltzmann method. Journal of Power Sources, 2014. 258: p. 89-97.

62. Molaeimanesh, G.R., H. Saeidi Googarchin, and A. Qasemian Moqaddam, Lattice Boltzmann simulation of proton exchange membrane fuel cells – A review on opportunities and challenges. International Journal of Hydrogen Energy, 2016. 41(47): p. 22221-22245.

63. Morgan, J.M. and R. Datta, Understanding the gas diffusion layer in proton exchange membrane fuel cells. I. How its structural characteristics affect diffusion and performance. Journal of Power Sources, 2014. 251: p. 269-278.

64. Muirhead, D., et al., Liquid water saturation and oxygen transport resistance in polymer electrolyte membrane fuel cell gas diffusion layers. Electrochimica Acta, 2018. 274: p. 250-265.

65. O'hayre, R., et al., Fuel Cell Fundamentals. 2006, Hoboken, New Jersey: John Wiley & Sons.

66. Ous, T. and C. Arcoumanis, Degradation aspects of water formation and transport in Proton Exchange Membrane Fuel Cell: A review. Journal of Power Sources, 2013. 240: p. 558-582.

67. Owejan, J.P., et al., Water Transport Mechanisms in PEMFC Gas Diffusion Layers. Journal of The Electrochemical Society, 2010. 157(10): p. B1456-B1464.

68. Owejan, J.P., et al., In situ investigation of water transport in an operating PEM fuel cell using neutron radiography: Part 2 – Transient water accumulation in an interdigitated cathode flow field. International Journal of Heat and Mass Transfer, 2006. 49(25–26): p. 4721-4731.

69. Pahon, E., et al., A signal-based method for fast PEMFC diagnosis. Applied Energy, 2016. 165: p. 748-758.

70. Park, C.H., et al., Nanocrack-regulated self-humidifying membranes. Nature, 2016. 532: p. 480.

71. Park, J., et al., A review of the gas diffusion layer in proton exchange membrane fuel cells: Durability and degradation. Applied Energy, 2015. 155: p. 866-880.

72. Park, S., J.-W. Lee, and B.N. Popov, A review of gas diffusion layer in PEM fuel cells: Materials and designs. International Journal of Hydrogen Energy, 2012. 37(7): p. 5850-5865.

73. Pei, P., et al., A review on water fault diagnosis of PEMFC associated with the pressure drop. Applied Energy, 2016. 173: p. 366-385.

74. Prat, M. and T. Agaësse, Thin porous media. Handbook of porous media, 2015: p. 89-112.

75. Qin, C., et al., Two-phase flow modeling for the cathode side of a polymer electrolyte fuel cell. Journal of Power Sources, 2012. 197: p. 136-144.

76. Qin, C.Z. and S.M. Hassanizadeh, A new approach to modelling water flooding in a polymer electrolyte fuel cell. International Journal of Hydrogen Energy, 2015. 40(8): p. 3348-3358.

77. Qin, Y., et al., Numerical investigation of water dynamics in a novel proton exchange membrane fuel cell flow channel. Journal of Power Sources, 2013. 222: p. 150-160.

78. Rasband, W.S., ImageJ. 1997-2016, U.S. National Institutes of Health: Bethesda, Maryland, USA.

79. Safi, M.A., et al., Experimental and pore-level numerical investigation of water evaporation in gas diffusion layers of polymer electrolyte fuel cells. International Journal of Heat and Mass Transfer, 2017. 115: p. 238-249.

80. Sasabe, T., S. Tsushima, and S. Hirai, In-situ visualization of liquid water in an operating PEMFC by soft X-ray radiography. International Journal of Hydrogen Energy, 2010. 35(20): p. 11119-11128.

81. Sinha, P.K. and C.-Y. Wang, Pore-network modeling of liquid water transport in gas diffusion layer of a polymer electrolyte fuel cell. Electrochimica Acta, 2007. 52(28): p. 7936-7945.

82. Solsona, M., C. Kunusch, and C. Ocampo-Martinez, Control-oriented model of a membrane humidifier for fuel cell applications. Energy Conversion and Management, 2017. 137: p. 121-129.

83. Song, M., et al., Water management of proton exchange membrane fuel cell based on control of hydrogen pressure drop. Journal of Power Sources, 2014. 267: p. 655-663.

84. Tavangarrad, A.H., et al., Continuum-Scale Modeling of Liquid Redistribution in a Stack of Thin Hydrophilic Fibrous Layers. Transport in Porous Media, 2018. 122(1): p. 203-219.

85. Trabold, T.A., Minichannels in Polymer Electrolyte Membrane Fuel Cells. Heat Transfer Engineering, 2005. 26(3): p. 3-12.

86. Voss, H.H., et al., Anode water removal: A water management and diagnostic technique for solid polymer fuel cells. Electrochimica Acta, 1995. 40(3): p. 321-328.

87. Wang, X. and T.V. Nguyen, An experimental study of the liquid water saturation level in the cathode gas diffusion layer of a PEM fuel cell. Journal of Power Sources, 2012. 197: p. 50-56.

88. Wang, Y. and K.S. Chen, Advanced control of liquid water region in diffusion media of polymer electrolyte fuel cells through a dimensionless number. Journal of Power Sources, 2016. 315: p. 224-235.

89. Wang, Y., et al., A review of polymer electrolyte membrane fuel cells: Technology, applications, and needs on fundamental research. Applied Energy, 2011. 88(4): p. 981-1007.

90. Wang, Y., et al., Stochastic modeling and direct simulation of the diffusion media for polymer electrolyte fuel cells. International Journal of Heat and Mass Transfer, 2010. 53(5): p. 1128-1138.

91. Wang, Y., et al., Double-layer gas diffusion media for improved water management in polymer electrolyte membrane fuel cells. Journal of Power Sources, 2015. 292: p. 39-48.

92. Wang, Z., et al., Improvement of PEMFC water management by employing water transport plate as bipolar plate. International Journal of Hydrogen Energy, 2017. 42(34): p. 21922-21929.

93. Wang, Z.H., C.Y. Wang, and K.S. Chen, Two-phase flow and transport in the air cathode of proton exchange membrane fuel cells. Journal of Power Sources, 2001. 94(1): p. 40-50.

94. Wu, H.-W., A review of recent development: Transport and performance modeling of PEM fuel cells. Applied Energy, 2016. 165: p. 81-106.

95. Wysokinski, T.W., et al., Beamlines of the biomedical imaging and therapy facility at the Canadian light source—Part 1. Nuclear Instruments and Methods in

Physics Research Section A: Accelerators, Spectrometers, Detectors and Associated Equipment, 2007. 582(1): p. 73-76.

96. Yan, W.-M., H.-Y. Li, and W.-C. Weng, Transient mass transport and cell performance of a PEM fuel cell. International Journal of Heat and Mass Transfer, 2017. 107: p. 646-656.

97. Yau, T.C., et al., Water transport and Schröder's Paradox in fuel cell membrane electrode assemblies. Journal of Power Sources, 2013. 224: p. 285-289.

98. Yousfi-Steiner, N., et al., A review on PEM voltage degradation associated with water management: Impacts, influent factors and characterization. Journal of Power Sources, 2008. 183(1): p. 260-274.

99. Zenyuk, I.V., et al., Investigating evaporation in gas diffusion layers for fuel cells with X-ray computed tomography. The Journal of Physical Chemistry C, 2016. 120(50): p. 28701-28711.

100. Zhang, D., Q. Cai, and S. Gu, Three-dimensional lattice-Boltzmann model for liquid water transport and oxygen diffusion in cathode of polymer electrolyte membrane fuel cell with electrochemical reaction. Electrochimica Acta, 2018. 262: p. 282-296.

APPENDICES

APPENDIX A

EXPERIMENTAL PROTOCOLS

A.1 Membrane Electrode Assembly Fabrication Protocol

This protocol describes the steps necessary to fabricate an MEA for use in the TP50E fuel cell.

1) Attach the edge of the Kapton (polyimide) tape to the edge of the table and roll out an amount equivalent to the length of the steel frames.
2) Align plate with the top alignment hole being on the right.
3) Stick the tape to the frame such that the left edge of the tape is touching the inner left side of the frame (approx. 1cm of coverage) and also covers the top and bottom edges of the frame.
4) Repeat the process for the second frame
5) Lay the GDL cutter face up and put the red alignment tubes into the corner holes, then place one of the frames on top such that the sticky side of the tape is facing the cutter
6) Using the exacto knife, trace the inside edge of the GDL cutter

    NOTE: In order to keep the tape taught, start ~1cm from the corner to cut each of the 4 sides, and then go back and finish the cut off

7) Repeat steps 4 and 5 for the other frame
8) Put on gloves
9) Place a liner on the cutting mat (either kimwipes or the paper that is included inside the Catalyst Coated Membrane (CCM) packaging)
10) Remove a CCM sheet from its packaging and place it on the liner
11) Align the CCM cutter over the CCM sheet in a way that reduces the amount of waste produced

    NOTE: CCM cutter should be sharp side down

12) Press down evenly on the cutter twice to create an initial outline
13) Holding the cutter steady, hammer each side and corner with the rubber mallet and then finish by hammering the center of the cutter. Try to avoid any wiggling of the cutter while hammer

    NOTE: If the cutter doesn't completely cut through in some spaces, finish the cut using an exacto-knife instead of trying to replace the cutter perfectly where it was before.

14) Trim any uneven sides with the exacto-knife
15) Set one of the steel frames on top of a kimwipe such that the sticky side is facing up and the kimwipe is covering the square hole cut out previously
16) Gently set the cut out square of CCM on top of the square hole in the tape such that there is approximately 1cm of tape overlapping with each edge of the CCM.

    NOTE: The most important part of this step is that there is contact on each edge of the CCM and the tape, the sides do not have to be equal but there must be coverage on each side.

17) Align the other frame with the red alignment tubes and set it down on top of the frame with the CCM in the middle
18) First run your finger along the edges of the tape covering the CCM to ensure a good adhesion
19) Then use the plastic spatula to apply firm but gentle pressure to the tape to smooth out air bubbles in between the two pieces of tape, working from the center towards the edges

    NOTE: When necessary it's possible to use an exacto knife to poke a small hole in a particularly stubborn air bubble. However, try to use this as a last resort.

20) Place a kimwipe in the middle of the MEA cutter so that the CCM doesn't touch it in the next steps
21) Using the red alignment tubes, place the connected frames on top of the MEA cutter
22) Using a black sharpie, mark where each of the steel springs align with the tape
23) Remove the connected frames, then cut out a hole on top of each of the marks using the hole punch by using the rubber mallet. Hammer the top of the hole-punch, twist the hole punch and then remove the cut out circle.
24) Once all of the holes have been cut, place the connected frames back on the MEA cutter and cut out the full MEA by tracing the <u>outside</u> of the square using an exacto knife
25) Place the MEA on top of a kimwipe sandwich and select the correct GDL's as required by the experiment
26) Cut the appropriate anode and cathode GDL by using the GDL cutter in the same fashion as cutting the CCM above (step 8)
27) Label the MEA on the bottom corner of the Kapton with:

    MEA #. Month. Year Anode GDL Cathode GDL

    IE: the second MEA created in January, 2018: **2.1.18 29BC35AA**

28) Put the MEA and two GDLs inside a kimwipe sandwich and place them under the mini table that hold the fuel cell.

<u>A.2 Start Up Protocol</u>

1) Turn on air tank (yellow) located toward the front of the lab
2) Turn on the hydrogen (red) and nitrogen (black) tanks located toward the back of the lab.
3) Turn on faucet for water flow
4) Plug in water pump (right of hydrogen tank)
5) Ensure all valves going to the machine are switched open
6) Open valve that compresses the fuel cell, located by the fuel cell
7) Turn on machine

8) Open Emerald –FCATS

A.3 Warm-Up Protocol

This protocol describes the steps necessary to heat up and pressurize the cell to the standard operating conditions of 75C and 206.9 kPa. The protocol should be modified to the appropriate final set points if a different operating condition is desired.

1) Switch the system from "Set-Up" to "LB Control" using the drop down menu in the upper left corner
2) Switch to the "Gas Flow Control" submenu
    - Set anode flow rate to 0.15 NLPM
    - Set cathode flow rate to 0.25 NLPM
3) Switch to the "Pressure and Temperature" submenu
    - Set anode/cathode pressure to 50 kPa
    - Set all temperatures to 35°C
4) When both anode and pressure reach 50 kPa, increase pressure set points to 100 kPa. Repeat until both are set to 206.9 kPa.
5) Once all temperatures have reached at least 30°C, increase set points to 45°C. Repeat until all temperatures are set to 75°C.
6) Switch to "Gas Flow Control" submenu
    - Set anode flow rate to 0.52 SLPM
    - Set cathode flow rate to 1.66 SLPM
7) Switch to "LB Control" submenu
8) Set current to 50 A
9) Let cell run for at least an hour

A.4 Shutdown Protocol

1) Set current to 0 A
2) Start a 2 minute gas purge
3) Press "STOP" button, located on the upper left of Emerald
4) When the gas purge is done, close all valves going to the machine and the valve for the external fuel cell compression
5) Unplug water pump
6) Close all gas tanks and shut off water

A.5 Manual Polarization Protocol

This protocol describes how to manually perform a polarization curve. This protocol should be aborted early if the voltage of the cell falls below 0.25 V.

1) Set current to 0 A
2) Set gas flow rates to:
    - Anode: 0.03 NLPM
    - Cathode: 0.08 NLPM
3) Start saving data and wait for 5 minutes
4) Set current to 2.5 A and wait ten minutes
5) Set gas flow rates to:
    - Anode: 0.04 NLPM
    - Cathode: 0.12 NLPM
6) Set current to 3.75 A and wait ten minutes
7) Set gas flow rates to:
    - Anode: 0.05 NLPM
    - Cathode: 0.17 NLPM
8) Set current to 5.00 A and wait ten minutes
9) Set gas flow rates to:
    - Anode: 0.10 NLPM
    - Cathode: 0.33 NLPM
10) Set current to 10.0 A and wait ten minutes
11) Set gas flow rates to:
    - Anode: 0.21 NLPM
    - Cathode: 0.66 NLPM
12) Set current to 20.0 A and wait ten minutes
13) Set gas flow rates to:
    - Anode: 0.31 NLPM
    - Cathode: 0.99 NLPM
14) Set current to 30.0 A and wait ten minutes
15) Set gas flow rates to:
    - Anode: 0.42 NLPM
    - Cathode: 1.33 NLPM
16) Set current to 40.0 A and wait ten minutes
17) Set gas flow rates to:
    - Anode: 0.52 NLPM
    - Cathode: 1.66 NLPM
18) Set current to 50.0 A and wait ten minutes
19) Set gas flow rates to:
    - Anode: 0.62 NLPM

- Cathode: 1.99 NLPM

20) Set current to 60.0 A and wait ten minutes
21) Set gas flow rates to:
    - Anode: 0.73 NLPM
    - Cathode: 2.32 NLPM
22) Set current to 70.0 A and wait ten minutes
23) Set gas flow rates to:
    - Anode: 0.83 NLPM
    - Cathode: 2.65 NLPM
24) Set current to 80.0 A and wait ten minutes
25) Set gas flow rates to:
    - Anode: 0.93 NLPM
    - Cathode: 2.98 NLPM
26) Set current to 90.0 A and wait ten minutes
27) Stop data collection

A.6 Standard Anode Water Removal Protocol

1) Set anode flowrate to 0.52 NLPM and cathode flow rate to 1.66 NLPM
2) Flip “Anode Dry Gas Bypass” switch to “Dry”
3) Start saving data
4) Start timer for 2 minutes
5) Set Anode flow rate to 0.69 NLPM (stoich of 2)
6) Wait 2 minutes
7) Set Anode flow rate to 1.04 NLPM (stoich of 3)
8) Wait 2 minutes
9) Set Anode flow rate to 1.38 NLPM (stoich of 4)
10) Wait 2 minutes
11) Set Anode flow rate to 1.73 NLPM (stoich of 5)
12) Wait 2 minutes
13) Set Anode flow rate to 2.08 NLPM (stoich of 6)
14) Wait 2 minutes
15) Set Anode flow rate to 2.42 NLPM (stoich of 7)
16) Wait 2 minutes
17) Set Anode flow rate to 2.77 NLPM (stoich of 8)
18) Wait 2 minutes
19) Set Anode flow rate to 3.11 NLPM (stoich of 9)
20) Wait 2 minutes
21) Set Anode flow rate to 3.46 NLPM (stoich of 10)
22) Wait 2 minutes
23) Stop collecting data

24) Flip “Anode Dry Gas Bypass” switch to humidified
25) Set Anode flow rate to 3.0 NLPM and wait 5 seconds,
26) Repeatedly lower the flow rate by 0.5 NLPM and then waiting 5 seconds until the starting flow rate of 0.52 NLPM is reached

APPENDIX B

DATA ANALYSIS MATLAB SCRIPTS

B.1 Polarization Curve Data Processing Script

This script is used to process the raw data output from the polarization curve test. Before running the script the raw time, voltage, and current SET POINT data needs to be posted into the "Polarization_test.xls" spreadsheet. The script will output the average voltage for each current set point, along with its associated standard deviation.

```
clear
close all
home

%Load your file name here by changing the .xls file
%The file has to have three columns...time, voltage, and current
    %set point
fileName = 'Polarization_test.xls';
testdata = xlsread(fileName);

%t = time, v = voltage, d = current  SET POINT
t = testdata(:,1);
v = testdata(:,2);
sd = testdata(:,3);
%mA/cm2 to normalize the current set point to current density
aa = 50;
d = sd.*(1000/aa);

%Set the tolerance for the different between current densities
    %ie diff(d)>=your input
%The startIdx and stopIdx look at the current density set point to see
when
    %it makes a jump
startIdx = find([1 ; abs(diff(d))>=1]);
stopIdx = [startIdx(2:end)-1 ; length(d)];

%This for loop with the startIdx/stopIdx is the heart and soul of the
code.
%It takes the voltage data at each current density based on the
startIDx
    %and the stopIdx
%This also stores the time, voltage, and current density in a cell area
that has to be
    %accessed like vv{1,j} where j is a current density

for j = 1:length(startIdx)

  idx = startIdx(j):stopIdx(j);
  tt{j}=t(idx); %all times at a given current density
  vv{j}=v(idx); %all voltages at a given current density
  dd{j}=d(idx); %all current densities (set pt repeats in all rows)
  V(j) = mean(v(idx)); %average voltage
  D(j) = mean(d(idx)); %average current density (same as set pt in this
case)
```

```
  vstd(j)=std(v(idx)); %standard deviation of voltage at a given
current density

end


%Plot the polarization curve and output the results...this has no
    %additional manipulation of the voltage data and contains all of
the data
    %so if you cycle the curve or go up and down etc then it all shows
up here
figure(1);
Dr=D';
Vr=V';
Vstd=vstd';
intr=1:1:length(Dr);
count=intr';%how many pts did you end up with...should match your
experiment!!
format bank;
results = [count Dr Vr Vstd] %results for the entire data set
errorbar(Dr,Vr, Vstd,'*r');
maxDr= max(Dr);
axis([0 maxDr 0 1]);
    xlabel('Curent Density')
    ylabel('Voltage');
%The problem with the plot above is that you can't do multiple curves
in a row
    %so you have to update the index here to pick out the data points
you want
    %In this case you know it starts at one and ends at point P.
    %This then takes the mean only for those first 1-->P data points
and
    %plots them in figure 2 to give the polarization surve

CDpoints = input('See the results above. How many points in your
polarization curve?     ');
CDstart = input('What point would you like to start with?   ');
CDend= CDstart+CDpoints-1;

for k = CDstart:CDend
   vvv(k)=mean(vv{1,k});
   ddd(k)=mean(dd{1,k});
   vvstd(k)=std(vv{1,k});
   k=k+1;
end
   figure(2)
    plot(ddd,vvv,'^')
   errorbar(ddd,vvv,vvstd,'.r');
   maxddd= max(ddd)+100;
   axis([0 maxddd 0 1]);
   xlabel('Current Density (mA/cm2)')
   ylabel('Voltage');
```

```
% These subplots show all of the voltage signals vs time, allowing you
to
%     see how steady the voltages are. From these you would know if you
needed
%     to 'clean up' the data further. The length of i needs to be
changed to
%     match the length of k above and the subplots have to be adjusted
to give
%     an MxN matrix that will accomodate all of the P plots....ie if
you had
%     14 points you could do a subplot(7,2,i)

Q=CDpoints/2;
H=round(Q);
m=1;
for i = CDstart:CDend;
   figure(3);
   subplot(H,2,m); %update to match dimensions of P
   m=m+1;
   plot(tt{1,i},vv{1,i})
   xlabel('Time (s)')
   ylabel('Voltage');
end
```

B.2 AWR Data Processing Script

This script is used to process the raw data output from the AWR test. Before running the script the raw time, voltage, anode flow rate SET POINT, anode pressure drop and cathode pressure drop data needs to be posted into the "AWR.xls" spreadsheet. The script will output an average voltage, anode pressure drop, and cathode drop for each anode stoichiometric point, along with their associated standard deviation.

```
clear
close all
home

%Load your file name here by changing the .xls file
%The file has to have three columns...time, voltage, and current
    %set point
fileName = 'AWR.xls';
testdata = xlsread(fileName);

%Need to change the file name here too
%t = time, v = voltage, d = anode flowrate SET POINT (replace this with
ANY setpoint you use)
% AnP = anode pressure drop % CatP = cathode pressure drop
t = testdata(:,1);
v = testdata(:,2);
d = testdata(:,3);
sd=d;
AnP = testdata (:,4);
CatP= testdata (:,5);
```

```
%Set the tolerance for the different between flow rates
    %ie diff(d)>=your input
%The startIdx and stopIdx look at the anode flow rate set point to see
when
    %it makes a jump
startIdx = find([1 ; abs(diff(d))>=0.05]);
stopIdx = [startIdx(2:end)-1 ; length(d)];

%This for loop with the startIdx/stopIdx is the heart and soul of the
code.
%It takes the voltage data at each current density based on the
startIDx
    %and the stopIdx
%This also stores the time, voltage, and current density in a cell area
that has to be
    %accessed like vv{1,j} where j is a current density

for j = 1:length(startIdx)

  idx = startIdx(j):stopIdx(j);
  tt{j}=t(idx); %all times at a given current density
  vv{j}=v(idx); %all voltages at a given current density
  dd{j}=sd(idx); %all current densities (set pt repeats in all rows)
  AnPp{j}=AnP(idx); %all anode pressure drops at a given current
density
  CatPp{j}=CatP(idx); %all cathode pressure drops at a given current
density
  V(j) = mean(v(idx)); %average voltage
  D(j) = mean(sd(idx)); %average current density (same as set pt in
this case)
  vstd(j)=std(v(idx)); %standard deviation of voltage at a given
current density
  anodP(j)=mean(AnP(idx)); % avg anode dP
  cathoP(j)=mean(CatP(idx));% average cathode dP
  anodPstd(j)=std(AnP(idx)); % st dev anode dP
  cathoPstd(j)=std(CatP(idx));% st dev cathode dP

end

figure(1);
plot(D,V,'o-')
Dr=D';
Vr=V';
Vstd=vstd';
anodpr = anodP';
cathoPr=cathoP';
AnodPstd = anodPstd';
CathoPstd = cathoPstd';
intr=1:1:length(Dr);
count=intr';%how many pts did you end up with...should match your
experiment!!
format('short');
```

```
results = [count Dr Vr Vstd anodpr AnodPstd cathoPr CathoPstd] %results
for the entire data set
errorbar(Dr,Vr, Vstd,'*r');
maxDr= max(Dr);
axis([0 maxDr 0.4 0.7]);
    xlabel('Anode Flow Rate (NLPM)')
    ylabel('Voltage');
```

APPENDIX C

VISUALIZATION PROTOCOLS

C.1 Background Correction

1) Open ImageJ-win64 in the Fiji.app folder
2) Open the BMIT Toolbox in the Plugins

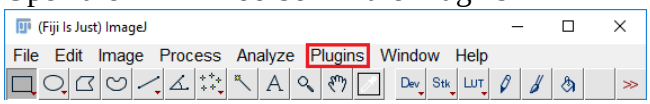

3) Select "Image Sequence (TIFF) Background Correction" and hit OK

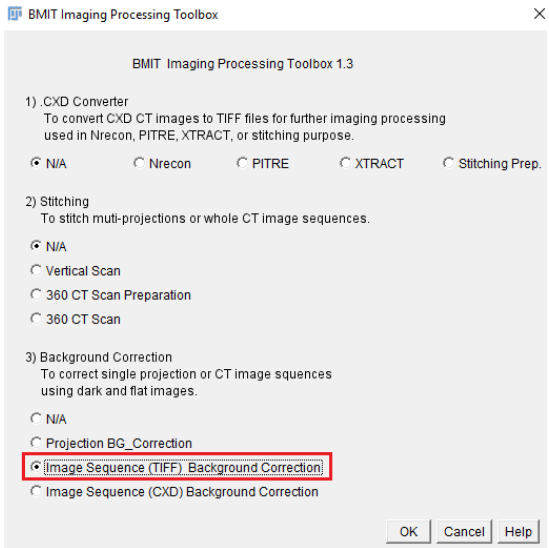

4) Select the folder with the dark images and hit ok
5) Select the folder with the flat images and hit ok
6) Select the folder with the flat images and hit ok
7) Hit OK on both of the popup windows that show up

C.2 3-D Reconstruction

1) Open "NReconServer" program
2) Open the "NRecon"
3) Open the first image in the "Corrected" folder that was created by the background correction script
4) Go to the "Settings" tab in the "Reconstruction" window (far right) and check the boxes for "Object larger than field of view" and "Ring artifacts reduction"
5) Go back to the "Start" tab and click the "Preview" button
6) The program will automatically switch to the "Output" tab, check the preview image to verify reconstruction
7) Uncheck the "Scales ON" box, click the browse button and create a new folder to save the reconstructed images to
8) Change the file format to TIF (16) using the drop-down menu
9) Go to the "Settings" tab and increase the Ring artifacts reduction from 1 to 20
10) Go back to the "Start" tab and hit Start

NOTE: if multiple fully reconstructed images are going to be compared or normalized to each other, the dynamic image range needs to be the same for all of them. These values can be set by clicking the button under the histogram in the “Output” tab after creating the initial “preview” image

C.3 Segmentation Protocol

1) Open “MetaMorph0068” program
2) Load sequence of images by File>Open Special>Build Stack>Numbered Names
3) Define region of interest by Region>Create Region
4) Set threshold of images by Measure>Threshold Image
5) After setting appropriate threshold, all measurements can be accessed through Measure>Region measurements

APPENDIX D

CURRENT RESULTS AND STATUS

D.1 Calculating Diffusion Coefficients
(Work performed by Megan English, undergraduate researcher at MSU)

First, Fick's Law was used to calculate overall diffusivities for the MEA:

$$J = D_{eff} \, {}^{\Delta c}/_{\Delta x}$$

where J is the anode removal water flux from the results presented in Chapter 2, Δc is the concentration difference across the MEA, again based on results from Chapter 2, and Δx is the cumulative MEA thickness, taken from published values. This equation was used to calculate the overall effective diffusivity for each time averaged stoichiometric point for the 25 BC GDL at T = 75°C, seen in Figure 30.

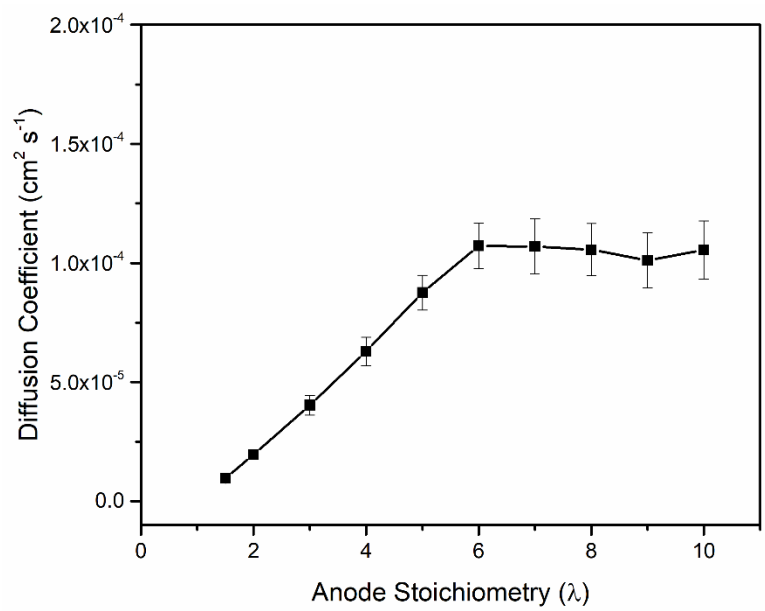

Figure 30. Calculated effective diffusivity based on anode stoichiometry for the three MEA configurations

The effective diffusivities calculated for the first five stoichiometric set point are found to be within the range of order of magnitudes as published literature values (1-10 x 10^{-6}) [1]. It was thought that the increasing pressure gradient might be introducing a

significant amount of pressure driven flow across the membrane at the higher stoichiometric flow rates. To investigate this potential contribution, the max potential hydraulic permeation was investigated based on the greatest pressure drop observed in the experiments. This rate was found to be 3 orders of magnitude less than the overall flux, so it was identified as a negligible term. Next, the potential contribution of the convective removal term from the anode stream will be investigated to see if it can help to resolve the difference. Previously, a modified AWR test was performed where the anode flow rate was held constant at a stoichiometry of 5 for 100 minutes, instead of step raises in the anode flow rate every 2 minutes for a total of 20 minutes, an example of these results are shown in Figure 31.

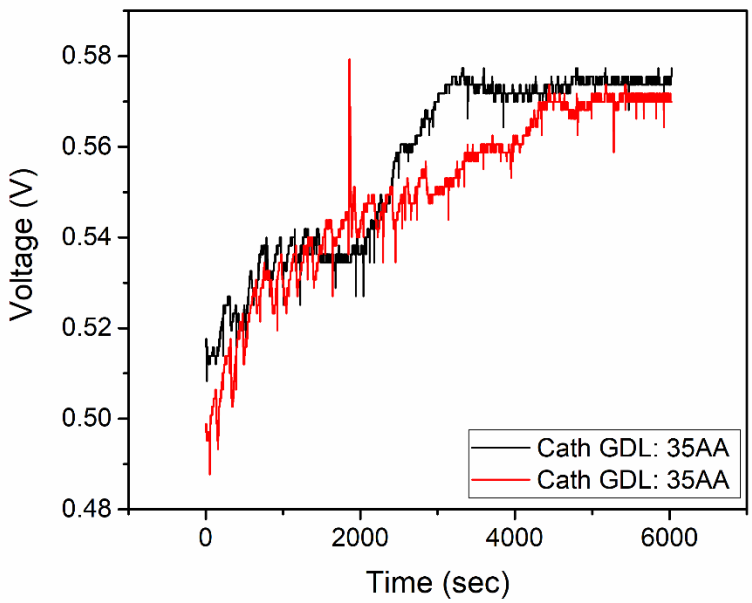

Figure 31. Example of constant flow rate AWR results, where the anode stoichiometry was held steady at $\lambda = 5$.

Results from this test showed that although the voltage did increase over time, it eventually reached a steady-state below the max voltage obtained using the standard test.

These two results taken together indicate that a convective component is likely driving the majority of the transport observed at the higher stoichiometries during the standard AWR protocol. To investigate this contribution, the base diffusion flux calculated from the initial stoichiometric set point should be removed from the proceeding points such that the remaining flux would be the convective term. The convective mass transfer coefficient h_m between the cathode GDL and air channel has been previously shown by Wang et al. [2] to be calculated by

$$h_m = {}^{Sh}/_{D_{gas}H_{gc}} \quad \text{(AD.1)}$$

where Sh is the Sherwood number, D_{gas} is the effective diffusivity of the gas, and H_{gc} is the height of the channel. If this equation was then extended to the anode side, the convective mass flux component could then be calculated to see if this accounts for the discrepancy between the calculated effective diffusivity and literature values, and also to help explain the general trend of the graph.

D.2 Modeling Desaturation and Vapor Transport

Currently, two CFD models have been generated in an attempt to describe the *ex-situ* setup used in the synchrotron investigation and to describe the *in-situ* flow field geometry used in the active fuel cell testing.

D.2.1 *Ex-Situ* CFD Model

(Work performed by Duncan Jacobsen, undergraduate researcher at MSU)

The flow field geometry used in the synchrotron testing was recreated in COMSOL Multiphysics version 5.3, seen in Figure 32.

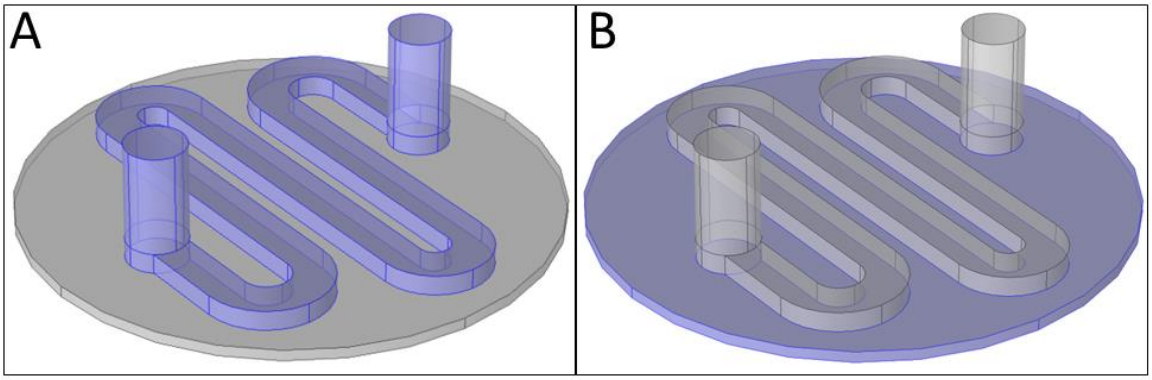

Figure 32. Recreated *Ex-situ* test cell geometry with A) channels highlighted and B) porous layer highlighted.

Currently, physics in the porous are set to laminar, steady-state flow using a modified version of Navier-Stokes, which takes into account the porosity and permeability of the GDL. Initial results have looked at the separate x, y, and z velocities within a dry porous layer to identify any high flowrate regions or potentials for channel bypass.

Next, the GDL was segmented into four quadrants, and the permeability of the lower right quadrant was reduced by four orders of magnitude to simulate the pocket of water found in that general location in the experimental work (detailed in Chapter 4). The x, y, and z velocities for this setup were then compared to the dry GDL 50 μm below the channel and halfway in the GDL, presented below in Figure 33 and 32. It is seen that the change in permeability has a noticeable effect on the various velocity profiles. Future work should focus on refining the mesh and seeing if we can do further segmentation of the porous layer.

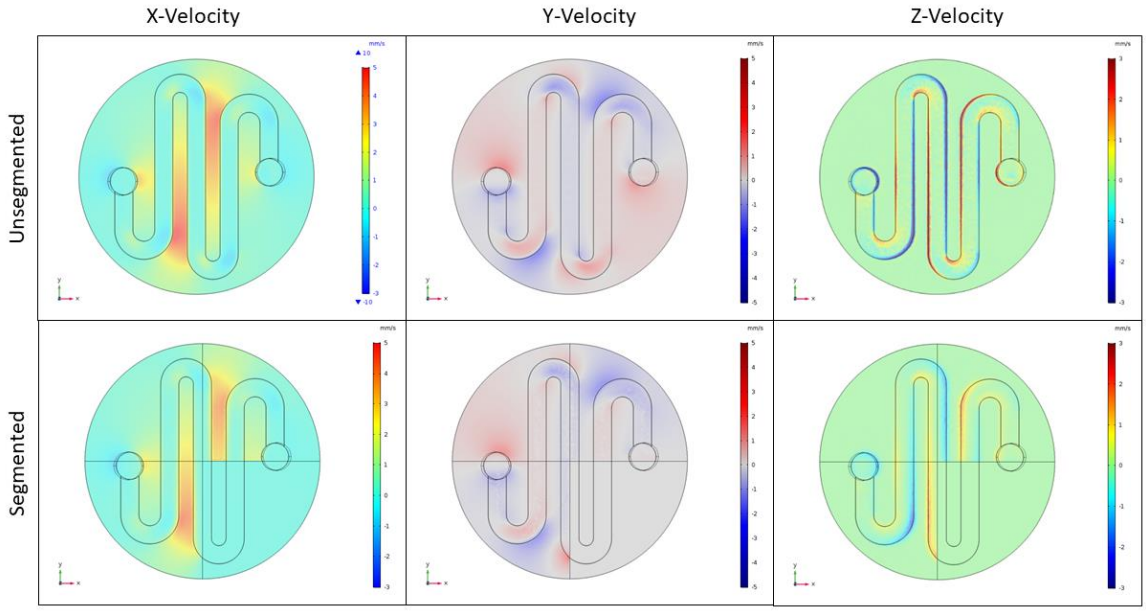

Figure 33. X,Y, and Z velocities for segmented and unsegmented porous layer 50 μm beneath channel.

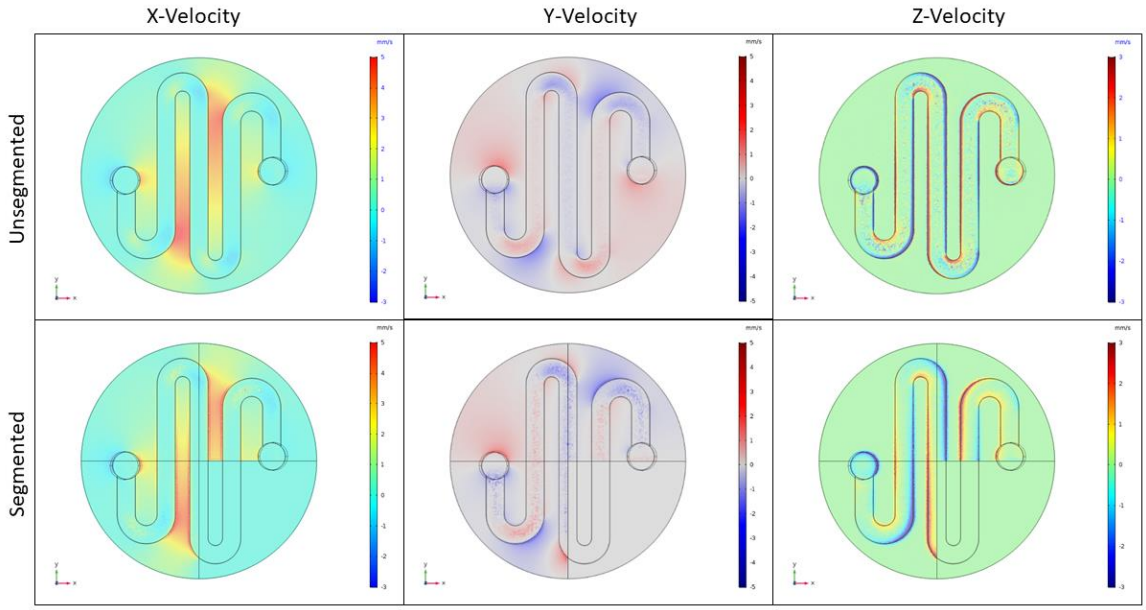

Figure 34. Y-velocities for segmented and unsegmented porous layer halfway through GDL

D.2.2 *In-situ* CFD model
(Work performed by Prasaad Milner, undergraduate researcher at MSU)

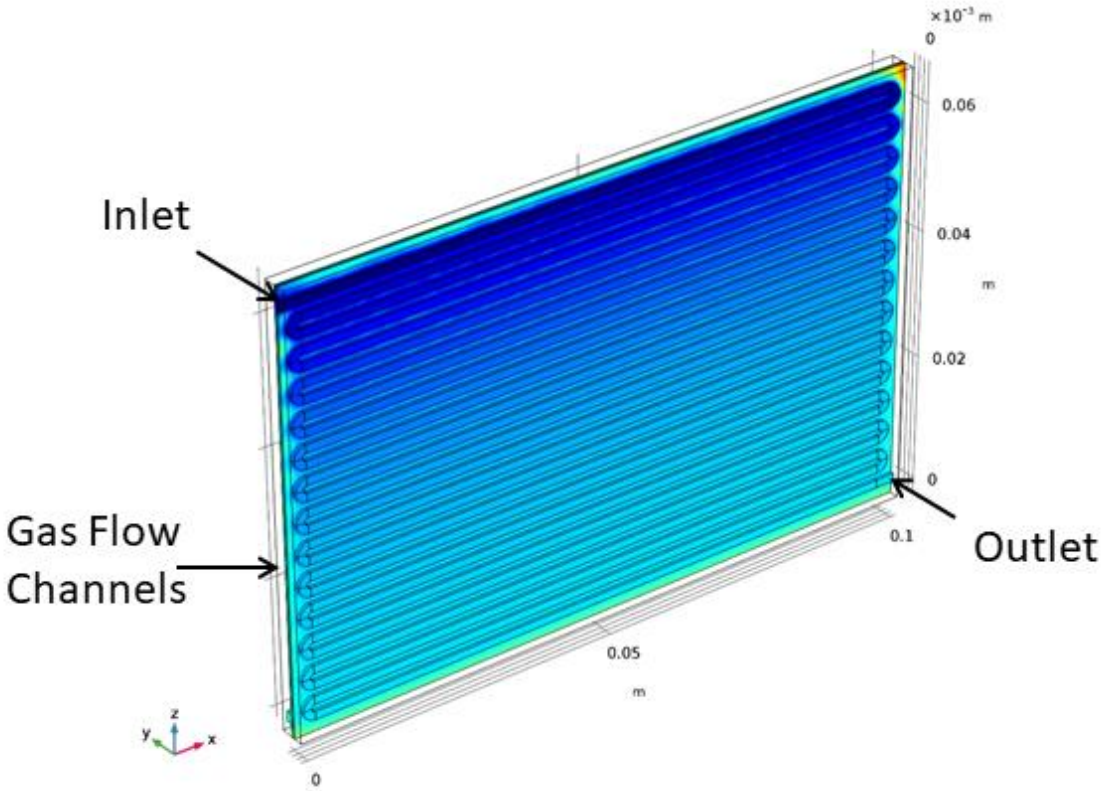

Figure 35. Reconstructed geometry of the active fuel cell in COMSOL

The active fuel cell flow field was also reconstructed in COMSOL Multiphysics version 5.3, including the 26 bends and the semi-co-flow, counter flow geometry wherein each individual anode/cathode channel is counter flow but the overall flow field is co-flow such that the inlet and outlets are aligned at the same ends of the flow field. This model was able to simulate the outlet RH, water vapor flux, and pressure drop observed in active fuel cell experiments, detailed in Chapter 2, but for a non-active setup. Future work should focus on refining the meshing and introducing the water production from the reaction at the appropriate layer.

References

1. Barbir, F., PEM fuel cells: theory and practice. 2012: Academic Press.

2. Wang, Z.H., C.Y. Wang, and K.S. Chen, Two-phase flow and transport in the air cathode of proton exchange membrane fuel cells. Journal of Power Sources, 2001. 94(1): p. 40-50.